THE DEVELOPMENT OF AN AXIAL ACTIVE MAGNETIC BEARING

R. GOUWS B.Eng

Dissertation submitted in partial fulfillment of the requirements for the degree Magister Ingeneriae in Electrical and Electronic Engineering at the North-West University

Supervisor: Prof. G. van Schoor

2004
Potchefstroom

SUMMARY

In this dissertation, the author presents the operation and development of active magnetic bearings (AMBs), with specific focus on axial AMBs. The project objective is the development of an axial AMB system. The electromagnetic design, inductive sensor design, dSpace® controller model design and actuating amplifier design are aspects discussed in this dissertation.

The physical model constitutes two electromagnets positioned above and beneath a 2 kg steel disc with an air gap of 3 mm on either side of the disc. The electromagnetic design is done analytically and verified using Quickfield® finite element analysis software.

Inductive sensors are designed to obtain position feedback from the model. These sensors measure the distance of the air gap between the suspended steel disc and the electromagnets. The dSpace® 1104 controller board and software is used for controlling purposes. This dissertation describes the system development from the Simulink® model to the real-time model, where the dSpace® controller board controls the physical hardware.

The dSpace® controller sends out control signals via D/A ports to actuating amplifiers. The actuating amplifiers then provide a controlling current to the electromagnets. The steel disc is attracted or released according to the signal provided. The inductive position sensors provide feedback from the model via the A/D port of the dSpace® controller to close the control loop.

The control performance of the model is evaluated through steady state analysis (static load test), dynamic disturbance analysis (downward disturbance test) and step response analyses (amplitude step response test). The step response analysis provide information about the time-to-peak, settling time, percentage overshoot, natural frequency, damping ratio, damping constant and stiffness of the model. The experimental results obtained agree with the expected theoretical norms.

Future possible projects can be done on the improvement of the sensor (designing a sensorless sensor), designing advanced control techniques for the axial AMB model by using the dSpace® DS1104 controller and designing an axial AMB model for high speed applications.

OPSOMMING

In hierdie verhandeling verskaf die outeur die werking en vervaardiging van aktiewe magnetiese laers (AMLs), met spesifieke fokus op aksiale AMLs. Die doel van die projek is om `n aksiale AML te ontwerp. Aspekte aangaande die elektromagnetiese ontwerp, induktiewe sensor ontwerp, dSpace® beheerder ontwerp en kragversterker ontwerp word in hierdie verhandeling bespreek.

Die fisiese model bestaan uit `n elektromagneet wat bo en onder `n 2 kg staal skyf gemonteer is met `n 3 mm luggaping aan beide kante van die skyf. Die elektromagnetiese ontwerp word analities gedoen en geverifieer met eindige element sagteware genaamd Quickfield®.

Die induktiewe sensor word ontwerp vir posisieterugvoer vanaf die model. Hierdie sensor meet die grootte van die luggaping tussen die gesuspendeerde staal skyf en die elektromagnete. Die dSpace® 1104 beheerderkaart en sagteware word gebruik vir beheerdoeleindes. Hierdie verhandeling bespreek die stelselontwikkeling vanaf die Simulink®-model tot by die in-tyd model, waar die dSpace® beheerderkaart die fisiese hardeware beheer.

Die dSpace® beheerder stuur beheerseine uit na die kragversterkters deur middel van sy D/A poorte. Die kragversterkers verskaf dan `n beheerstroom vir die elektromagnete. Die staal skyf word dan aangetrek of laat val volgens die sein verskaf. Die induktiewe posisiesensor verskaf terugvoer vanaf die model deur middel van die A/D poort van die dSpace®-beheerder om die beheerlus te sluit.

Die doeltreffendheid van die beheerder word ge-evalueer deur middel van bestendige toestand foutanalise (statiese las toets), dinamiese steuringsanalise (afwaardse steurkrag toets) en trap-responsanalise (amplitude traprespons toets) op die model toe te pas. Die amplitude traprespons toets verskaf inligting aangaande die piektyd, vestigingstyd, persentasie verbyskiet, natuurlike frekwensie, dempingsverhouding, dempingskonstante en styfheid. Die eksperimentele resultate wat verkry is stem ooreen met verwagte teoretiese norme.

Toekomstige moontlike projekte kan gedoen word op die verbetering van die sensor (ontwerp van `n sensorlose sensor), ontwikkeling van gevorderde beheeralgoritmes vir die aksiale AML model deur gebuik te maak van die dSpace® DS1104 beheerder en om `n aksiale AML model te ontwerp spesifiek vir hoë spoed rotasie.

Elkeen wat lewe, moet ter harte neem wat die uiteinde van die mens is.

Prediker 7:2

Verder se hy vir my: "Moenie die woorde van hierdie profetiese boek geheim hou nie, want die eindtyd is naby..."

Openbaring 22:10

... for that is the end of all men; and the living will lay it to heart.

Ecclesiastes 7:2

And he told me, Do not seal up the words of the prophecy of this book and make no secret of them, for the time when things are brought to a crisis and period of their fulfillment is near.

Revelation 22:10

DANKBETUIGINGS

Prof G. van Schoor vir al sy tyd, ondersteuning en leiding gedurende die studie. Daar is slegs `n handjie vol mense wat so baie moeite soos hy sal doen.

Markus vir bystand, hulp en christelike ondersteuning.

Daleen vir ondersteuning en begrip.

M Tech Industrial vir finansiële ondersteuning met die studie.

TABLE OF CONTENTS

APPENDIX SECTION

LIST OF FIGURES

LIST OF TABLES

NOMENCLATURE

Abbreviations	**Definition**
AMB	Active Magnetic Bearing
LPV	Linear Parameter Varying
AVBC	Adaptive Variable Bias Control
THVD	Total Harmonic Voltage Distortion
THID	Total Harmonic Current Distortion
CSR	Current Slew Rate
FSR	Force Slew Rate
MMF	Magneto-motive Force

Symbols	**Definition**
A_g	Area of the air gap facing a single pole
A_w	Cross-sectional area of the wire used for the current-carrying coil
A_1, A_2	Face area of outer and inner pole of magnetic axial bearing respectively
B	Magnetic flux density
C_{eq}	Equivalent (or effective) damping of the bearing
cf	Correction factor
D_1, D_4	Outer and Inner diameter of the bearing respectively
D_2, D_3	Outer and Inner diameter of the coil gap respectively
D_{mean}	Mean diameter of the coil gap
F	Actual force developed by the bearing
ff	Fringing factor
h	Effective air gap for the magnetic circuit
i	Current in the coil
K_{eq}	Equivalent stiffness of the bearing
K_i	Current stiffness of the bearing
L	Length (axial) of the bearing
L_{coil}	Inductance of the coil
lf	Leakage factor
L_w	Length of the wire in the coil
N	Number of turns making up the coil
R	Total reluctance of the magnetic circuit
R_{coil}	Resistance of the total length of the coil wire at the temperature T
R_0	Resistance of the total length of the coil wire at the temperature T_0
R_g, R_i	Reluctance of each air gap and of the ith. flux path respectively
Z	Maximum possible displacement of the shaft in the axial direction with magnetic thrust bearings
α_0	Temperature coefficient of the resistance of the coil wire at the temperature T_0
Δ	Permeance of a magnetic flux path
μ, μ_0	Permeability of a medium, Permeability of free space
$\mu_r Fe$	Relative permeability of iron
ρ	Resistivity of the wire material
ϕ, ω	Magnetic flux and Frequency respectively

CHAPTER 1
INTRODUCTION

The Pebble Bed Modular Reactor (PBMR) is a small, safe, clean, cost-efficient, inexpensive and adaptable nuclear power plant, using coated uranium particles encased in graphite to form a fuel sphere (60 mm in diameter). In addition, the PBMR design makes use of helium as the coolant and energy transfer medium to a closed cycle gas turbine and generator. Helium is used, because it is radiologically inert.

According to the PBMR engineers, the use of normal bearings for rotational devices, would have the result that contaminated oil particles would run through the system. Thus although the helium is radiologically inert, the oil particles can make the process radioactive. If the oil particles would somehow leak from the system it would cause serious illness or even death.

A solution to this problem is to use a magnetic bearing system where the rotor is magnetically suspended. A magnetic bearing system has the advantage that it does not need any oil. This advantage will prevent radioactive contamination of the system. This in turn makes the surrounding environment safer in case of leakage.

A magnetic bearing system is a much cleaner and safer system compared to a conventional lubricated bearing system and it requires much less maintenance. The project objective is to develop a working axial AMB system, on which measurements and tests can be conducted in a research environment.

Improvements on this project will lead to future research projects. This project together with others will provide a knowledge base in the field of active magnetic bearings (AMBs).

This dissertation starts with a system design explaining al the different stages of the project, followed by a thorough study on AMBs. The design of the model and induction sensor design can be found in chapter 3 and 4 respectively, followed by the development and implementation of the controllers in chapter 5.

The dissertation ends with a system evaluation and verification, followed by conclusions and results. The appendices provide technical information about the project.

1.1. PURPOSE OF RESEARCH

The main project objective is the development of a working axial AMB system. Secondary objectives are the establishment of research capacity at the university and establishment of a research laboratory.

1.1.1. ESTABLISH RESEARCH CAPACITY

There is a lack of knowledge in the field of AMB systems driven by dSpace® controllers. The purpose is to establish research capacity which would lead to the offering of post-graduate courses on AMBs. The research program will also facilitate Masters and Doctorate studies on AMBs.

1.1.2. ESTABLISH RESEARCH LABORATORY

A secondary objective is to establish a research laboratory where future studies on AMB can be done. The research laboratory will be used to solve problems that may be encountered at industrial plants. Solutions and results can be obtained in the laboratory and a demonstration of a working model can be given, before implemented at the plant.

1.2. ISSUES TO BE ADDRESSED

The issues that need to be addressed before fulfilling the main project objective can be divided in 4 stages. Figure 1.1 provides a block diagram of the basic layout of the project. This figure shows the different stages of the project that will help with the explanation.

The controller (stage 1) receives the error signal as input and provides a control signal as output. The power amplifier (stage 2) receives the control signal and sends out a signal to the axial AMB model (stage 3). The axial AMB model consists of two electromagnets, one above and one beneath a steel disc. Position sensors (stage 4) measure the position of the suspended disc and provides position feedback to the controller.

More detail on the system design of the project can be found in section 1.4.

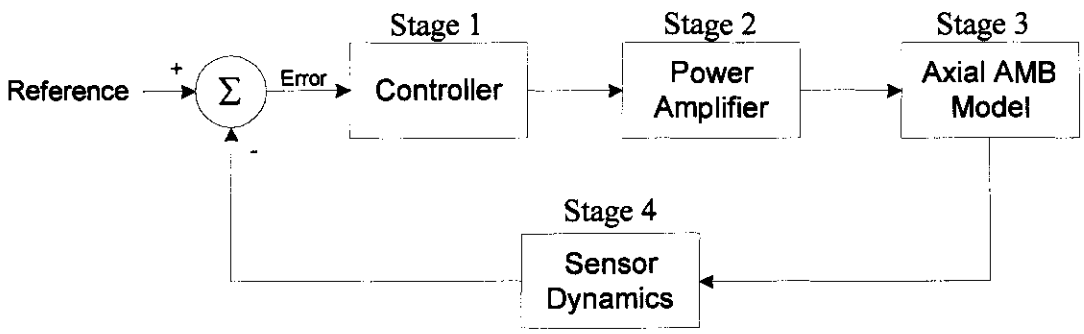

Figure 1.1: Block diagram of the basic layout of the project

1.3. RESEARCH METHODOLOGY

This project will be conducted in six phases: 1) Background study on the AMB, 2) Axial AMB model design, 3) Position sensor design, 4) Controller development and implementation, 5) Results obtained and system evaluation, 6) Conclusions and improvements.

1.3.1. BACKGROUND STUDY ON THE AMB

A thorough study on AMBs needs to be done, with special attention given to axial AMBs. A study on the first practical magnetic bearing, operation of an AMB, background on bearings and sensors for AMB systems, benefit of magnetic bearings, limitations of magnetic bearings and future AMB control technologies will therefore be done.

1.3.2. AXIAL AMB DESIGN

During this part the complete axial AMB model will be designed. A theoretical design of the model will first be done, followed by a verification of the data using a finite element software package. In the theoretical design of the model the specification of the model and core dimensions needs to be calculated. The magnetomotive force and magnetic flux will be verified using the finite element software.

1.3.3. POSITION SENSOR DESIGN

In this section the position sensor will be designed. A complete circuit diagram must therefore be designed and explained. The characteristics of the sensor need to be determined and tests must be performed to verify its functionality.

1.3.4. CONTROLLER DEVELOPMENT AND IMPLEMENTATION

The electromagnetic suspension model dynamics needs to be determined before controller development and implementation. The simulation design, analogue controller design and discrete controller design can then be done.

1.3.5. RESULTS OBTAINED AND SYSTEM EVALUATION

During this stage a system analysis will be done. The model will be tested under load and disturbance conditions. Finally the stiffness of the model will be measured as a function of control parameters.

1.3.6. CONCLUSIONS AND IMPROVEMENTS

In this part some conclusions on the model will be formulated. The necessary improvements that can be done on the model will also be discussed.

1.4. SYSTEM DESIGN

The system design can be divided into 4 stages. Figure 1.2 provides a block diagram of the basic layout of the project.

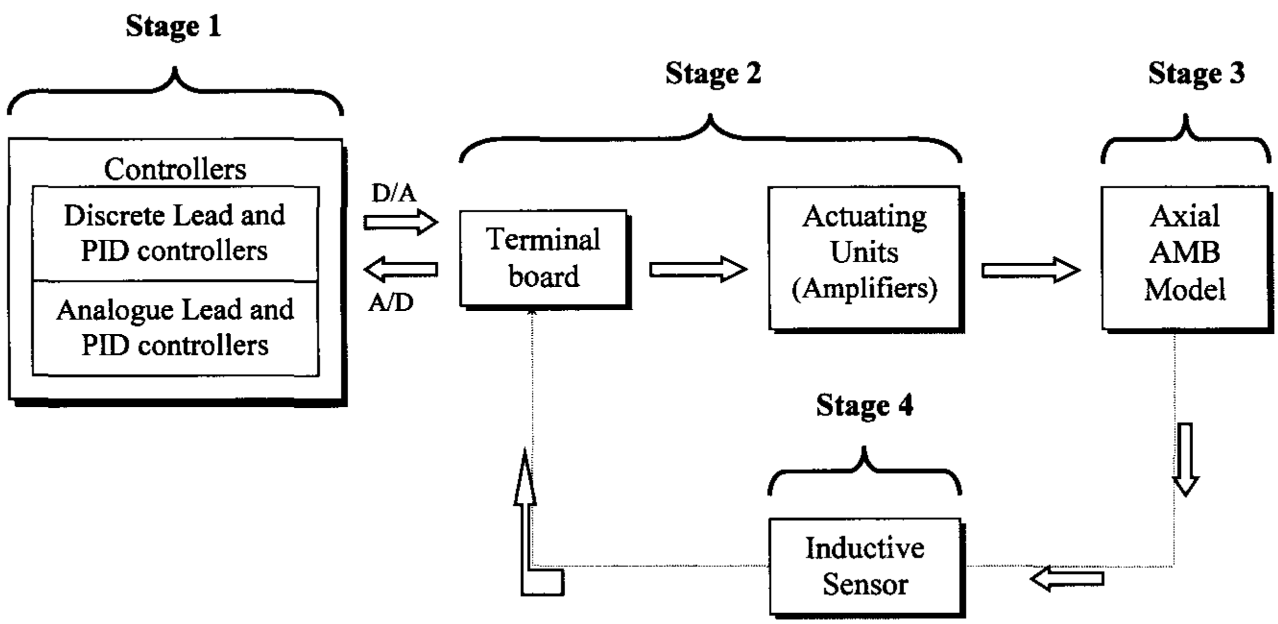

Figure 1.2: Block diagram of the AMB system

1.4.1. STAGE 1: ANALOGUE AND DISCRETE LEAD AND PID CONTROLLERS

This stage focuses on the design of the different controllers. The analogue and discrete lead and analogue and discrete PID controllers will be designed and tested.

It was decided to use the dSpace® 1104 R&D Controller Board for the discrete controllers, since it is the leading standard in the world for controlling hardware. dSpace® is widely used in the motor industry by manufactures like Audi, BMW and Mercedes. It has also proven to work for controlling AMB systems with moving parts, which makes it ideal for future projects.

dSpace® controlling software (Controldesk®) will be used, since it is integrateable with Matlab/Simulink®. The dSpace® controlling hardware consists of a DSP controller card with A/D and D/A slots. These slots will be used for controlling the axial AMB model.

Software code can be written in Simulink® and after verification downloaded onto the DSP programmable card. The system is then ready for real time interfacing and simulations. Data can then be sent and received via the controller and adjustments on the system stability can be made in real time mode.

1.4.2. STAGE 2: TERMINAL BOARD AND ACTUATING UNITS

The terminal board receives signals from the computer and sends them to the actuating units. It also receives signals from the sensors and sends them back to the computer. The purpose of the terminal board is to protect the computer and the dSpace® card from any high voltage spikes coming from the actuating units. This board will also scale the input and output signals to the correct amplitude for the dSpace® controller card.

The project was started by using PWM power amplifiers. The computer and dSpace® card was protected against high voltage spikes by using an opto-isolator. Unfortunately the power amplifiers did not perform to standard and it was decided to use power transistors as an actuating unit.

These power transistors isolate the secondary high voltage/high current side from the primary low voltage/low current side and makes it safe to connect the dSpace® controller to the rest of the circuitry.

For the axial AMB model two actuating units will be used. These actuating units consist of NPN power transistors, attracting and releasing the suspended object. The one will be used to provide the top electromagnet with the correct potential and the other one to provide the bottom electromagnet with the correct potential to suspend the object.

1.4.3. STAGE 3: AXIAL AMB MODEL

The model will consist of a suspended object (in this project a 2kg steel base will be used) and two electromagnets. The one electromagnet will be placed on top of the steel base and the other one beneath the steel base. The steel base will be connected to a steel rod and will be able to freely move in die axial direction. The steel base will not be able to move in die radial direction.

1.4.4. STAGE 4: INDUCTIVE SENSOR

Inductive sensors will be designed to provide position feedback to the controlling hardware. These sensors will measure the distance of the air gap between the steel base and the electromagnets. The focus is to suspend the steel base, thus the position must be controlled precisely.

1.5. SUMMARY

The focus of this project is to develop a working axial AMB system. For this purpose the project is divided into 4 main stages. The different stages can be seen in the system design (section 1.4).

After these stages are finished the system integration will be done. Various disturbance and load tests will then be performed on the system. These tests will provide us with useful information about the operation of the axial AMB system.

CHAPTER 2
ACTIVE MAGNETIC BEARINGS

2.1. INTRODUCTION

Magnetic bearings have structured themselves in bearing technology over the past few years. They take radial loads or thrust loads by utilising a magnetic field to support the shaft rather than a mechanical force as in fluid film or rolling element bearings. [4]

A magnetic bearing system constitutes four basic components: (1) magnetic actuator, (2) electronic control, (3) power amplifier and (4) shaft position sensor. In many ways, magnetic bearing components resemble electric motors with the basic magnetic actuator being constructed of soft ferromagnetic material electromagnetically activated by a coil of wire.

Magnetic bearings are non-containing, which means they have negligible friction loss, no wear, and higher reliability. Magnetic bearings enable previously unachievable surface speeds to be attained. Lubrication is eliminated, meaning that these bearings can be incorporated into processes that are sensitive to contamination, such as the vacuum chambers in which many semiconductor manufacturing processes take place.

2.2. FIRST PRACTICAL MAGNETIC BEARING

Professor Jesse W. Beams (1898 – 1977) developed the first practical magnetic suspension for high speed rotating devices. These devices include high speed rotating mirrors, ultracentrifuges and high speed centrifugal field rotors. [24]

Prof. Beams employed magnetic suspension as a means to carry out extensive experiments on physical properties in areas of isotope separation, biophysics, materials science and gravitational physics. He typically thought of ways to modify and improve experimental equipment. The improved equipment then gave much better experimental results. [3]

2.3. OPERATION OF AN AMB

Figure 2.1 provides a layout of the operation of an AMB. From this figure the stator, rotor and flux path can be seen. AMBs work on the principle that ferromagnetic particles are attracted by an electromagnet. The rotor of an AMB is made out of a material called ferromag.

This property of the rotor makes it ideal for a rotor to be supported by an electromagnet in the stator of a motor. The purpose of the electromagnet is to apply a force on the rotor to maintain a constant air gap, between the rotor and the stator. [9], [12]

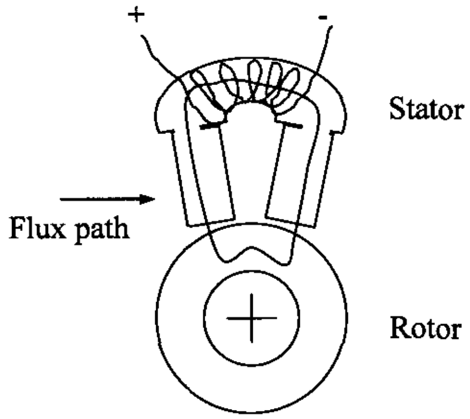

Figure 2.1: Operation of an AMB [16]

As the air gap between these two parts decreases, the attractive force increases, therefore, electromagnets are inherently unstable. A control system is needed to regulate the current and provide stability of the forces and position of the rotor.

The control process begins by measurement of the rotor position by means of a position sensor. The signal from this device is received by control electronics, which compares it to the desired position during machine start-up. Any difference between these two signals result in calculation of the force necessary to pull the rotor back to the desired position.

The position error is translated into two commands to the power amplifiers connected to the magnetic bearing stator. The current is increased in the one power amplifier, causing an increase in magnetic flux, an increase in the forces between the rotating and stationary components, and finally, movement of the rotor toward the stator along the axis of control. While the current in the one power amplifier increases, the current in the other power amplifier decreases with the inverse effect. [7]

Since the natural tendency of the stator is to attract the rotor until it makes contact, some control action is required to modulate the magnetic field and maintain the rotor in the desired position. The most common type of control involves the feedback of shaft position. This information is then used by the control system to modulate the magnetic field through power amplifiers, so that the desired rotor position is maintained even under changing shaft load conditions.

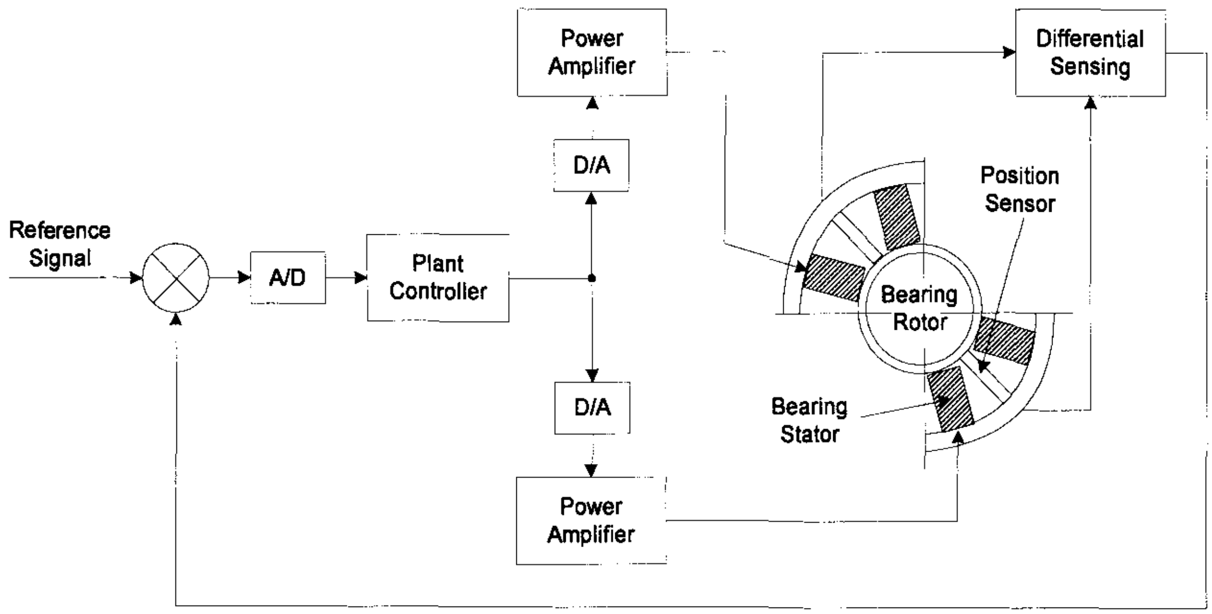

Figure 2.2: An active magnetic bearing system [16]

An AMB system constitutes electromagnets, position sensors, a control system and power amplifiers, as shown in the figure 2.2. The bearing actuators and sensors are located in the machine, while the control system and amplifiers are generally located remotely.

2.4. BACKGROUND ON BEARINGS AND SENSORS FOR AMB SYSTEMS

To provide support in more than one direction, magnetic poles are oriented about the periphery of a radial bearing. This is shown in figure 2.3.

Radial bearing construction is very similar to that of an electric motor, involving the use of stacked steel laminations, around which power coils are wound. Stacked laminations are also used in the rotor to minimize eddy current losses, which are a very small source of drag in a magnetic bearing and cause localized heating on the rotor.

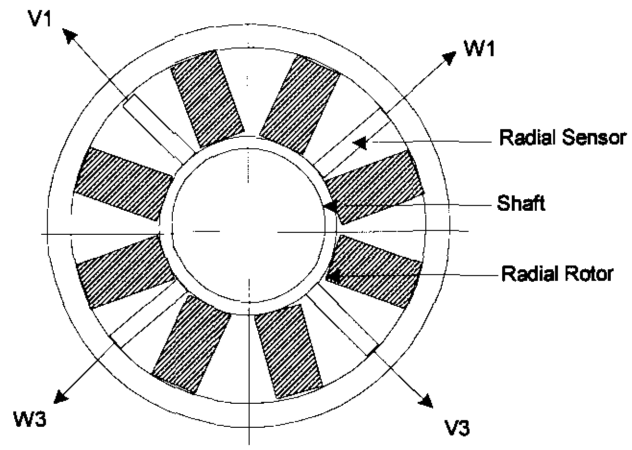

Figure 2.3: Magnetic poles for support [5]

The sensors are also oriented about the periphery of the stator, usually inside a ring or individual tubes mounted adjacent to the actuator poles. Position sensors are used, that measure the distance of the air gap between the sensor and the rotor laminations. Two measurements are taken for each radial axis and the rotor center position is calculated by means of a bridge circuit. [2]

A typical rotating machine will experience forces in both the radial and axial directions. Typically, a 5-axis orientation of bearings is used, incorporating 2 radial bearings of 2 axes each, and 1 thrust bearing. The orientation of these axes is shown in figure 2.4.

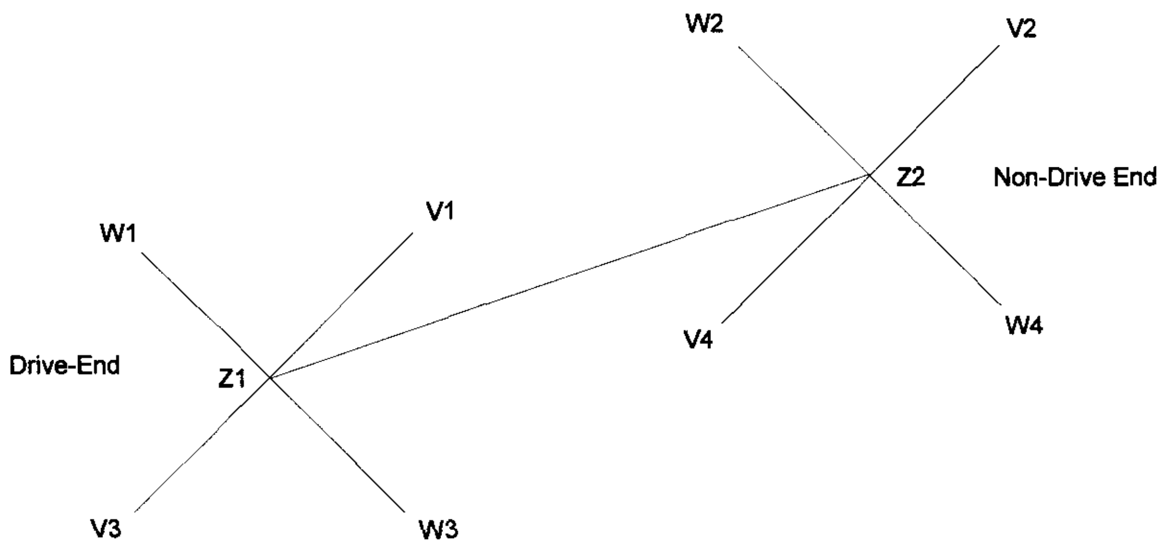

Figure 2.4: 5-axis orientation of a magnetic bearing [22]

Thrust bearings provide a magnetic flux path in the axial direction, between 2 stators oriented on either side of a thrust rotor (or disc). This is then mounted on the rotating shaft as shown in figure 2.5. An axial sensor measures the position of the shaft.

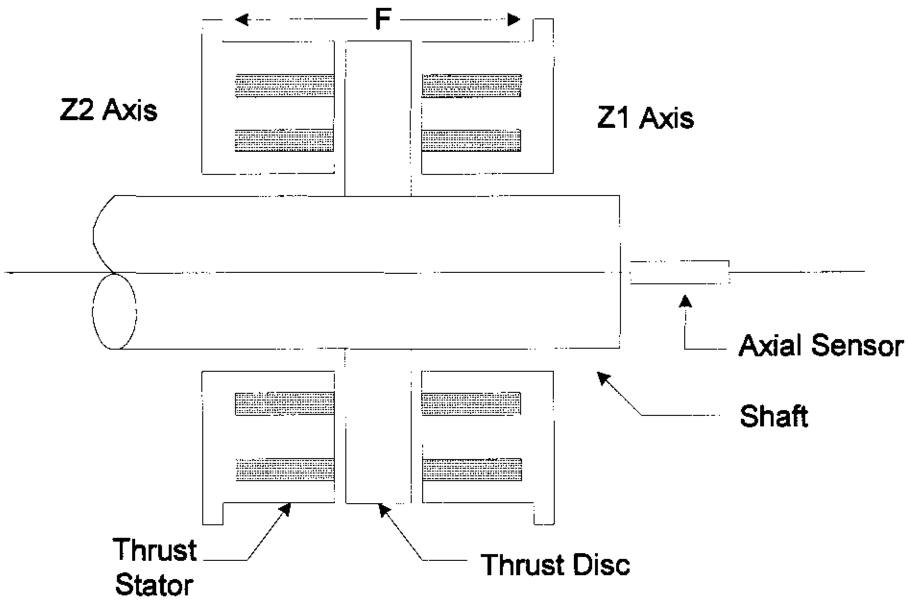

Figure 2.5: Thrust bearing [16]

2.5. BENEFITS OF MAGNETIC BEARINGS

2.5.1. HIGH RELIABILITY

With magnetic bearings there is no contact between the rotating and stationary parts, meaning there is no wear. In most cases failure modes are limited to control electronics, power electronics, and electrical windings. These components have design lives far greater than that of conventional bearings.

Magnetic bearings are fitted with protective back-up bearings. In addition, magnetic bearings have built-in overload protection. Magnetic bearings can signal process control equipment to stop the machine instantaneously in the case of excessive load.

Magnetic bearings provide high reliability and long service intervals in time critical applications for semiconductor manufacturing, vacuum pumps, and natural gas pipeline compression equipment. [25]

2.5.2. CLEAN ENVIRONMENTS

In a magnetic bearing system, particle generation due to wear and the need for lubrication are eliminated. There is therefore no chance of contaminating a clean process with oil, grease or solid particles. [17]

Magnetic bearings offer a dry, clean and economic solution for semiconductor fabrication equipment, vacuum pumps, gas and air compressors, and various other turbo machines that require submersion in a process fluid, even under pressure.

2.5.3. HIGH SPEED APPLICATIONS

The fact that a rotor spins in space without contact with the stator means drag on the rotor is minimal. That opens up the opportunity for the bearing to run at exceptionally high speeds, where the only limitation becomes the yield strength of the rotor material. [17] Please note windage losses under limitations of magnetic bearings (section 2.6).

2.5.4. POSITION AND VIBRATION CONTROL

Magnetic bearings use advanced control algorithms to influence the motion of the shaft and therefore have the inherent capability to precisely control the position of the shaft within microns and to virtually eliminate vibrations.

2.5.5. EXTREME CONDITIONS

2.5.5.1. TEMPERATURE

The magnetic bearing system is capable of operating through an extremely wide temperature range. Magnetic bearings can operate as low as -256°C and as high as 220°C, thus allowing operation where traditional bearings will not function. [1]

2.5.5.2. CORROSIVE FLUIDS

Magnetic bearings can operate in corrosive environments by means of canning both the stationary and rotating parts. [27]

2.5.5.3. PRESSURE

Magnetic bearings are virtually insensitive to pressure. They can be submerged in process fluid under pressure without the need for seals, as is the case with conventional bearings. Magnetic bearings can also operate in vacuum where their operation is even more efficient due to lack of windage. [4]

2.5.6. EQUIPMENT DESIGN, DEVELOPMENT AND TESTING

A magnetic bearing system can be used as an exciter, where the bearing force is modulated for deliberately exciting vibrations. The excitation force is applied to the rotor without contact and can be measured precisely. This makes magnetic bearings a valuable tool in equipment design, development and testing as well as in rotor dynamic research. [23]

2.5.7. MACHINE DIAGNOSTICS / SMART MACHINES

In order to function, a magnetic bearing must determine rotor position, rotor vibration and bearing load. This information is processed into an electronic database which provides an output to the end users, such that there is a constant knowledge of the operating state of the machine. This allows the user to detect incipient faults, plan maintenance and optimise performance. [17]

2.5.8. ELIMINATION OF OIL SUPPLY

Magnetic bearings do not require oil lubrication so they are well suited to applications such as canned pumps, turbo-molecular vacuum pumps, turbo-expanders and centrifuges where oil cannot be employed. [4]

2.5.9. VERY LOW POWER CONSUMPTION AND VERY LONG LIFE

There is no contact between the rotor and stator, this means no wear. Where fluid film bearings have high friction losses due to the oil shearing effects, magnetic bearing losses are due to low level air drag, eddy currents and hysteresis.

Also the losses associated with oil pumps, filters and piping are much greater than the power associated with controls and power amplifiers. Overall, magnetic bearings normally have an order of magnitude lower power consumption than oil film bearings. [4]

2.5.10. LOW WEIGHT

A recent study of aircraft gas turbine engines indicates that the elimination of oil supply and associated components with magnetic bearings could reduce the engine weight by approximately 25%. [4]

2.6. LIMITATIONS OF MAGNETIC BEARINGS

2.6.1. LARGER BEARINGS

Magnetic bearings have a specific load capacity (maximum load per unit of area of application) lower than most conventional bearing systems. This results in bearings which may be physically larger than other similarly specified bearings. Therefore magnetic bearings have a lower load capacity. [20], [4]

2.6.2. HIGHER COMPLEXITY AND COST

The higher complexity of magnetic bearings often means the initial purchase price is higher than competing technologies. However, magnetic bearings life cycle cost can often be less than traditional bearings. This is particularly true where the alternatives are exotic bearings. [5], [4]

2.6.3. REQUIRES ELECTRICAL POWER

Magnetic bearings require power to drive the control systems, sensors and electromagnets. [25]

2.6.4. WINDAGE LOSSES

At high rotating speed, windage (friction between moving parts and air) becomes a problem. For inline electric motors the circumferential speed needs to be limited not due to the material strength but due to high windage losses at the motor surface. These windage losses increase linearly with the pressure. [13]

Modern flywheel uninterruptible power supplies has an useful power delivery for 10 to 50 seconds, a maximum surface speed of 122 m/s and losses over 1 kW for windage losses not in a vacuum. [14]

2.7. FUTURE AMB CONTROL TECHNOLOGIES

Future AMB control technologies are likely to be driven by: (1) higher operating speeds, (2) lower power loss, (3) greater use of available clearance, (4) generalised actuation, sensing and control and (5) control of unbalance response.

2.7.1. HIGHER OPERATING SPEEDS

Magnetic bearings already permit higher operating speeds than conventional bearings. However, demand for even greater speed is likely to be strong, e.g., for energy storage flywheel systems for electric vehicles. Higher rotational speed implies a greater rotor gyroscopic effect which results in the plant being linear parameter-varying (LPV).

2.7.2. LOWER POWER LOSS

Lower power loss is especially important for high-speed applications since rotation of the rotor in a supporting magnetic field can cause significant losses. These result in both reduced machine efficiency and excessive rotor heating.

For some applications, rotating losses can be reduced significantly if the AMB is operated with a bias flux. However this gives a low (zero) minimum force slew rate (i.e., time derivative of force) and has an obvious impact on both rotor stabilisation and disturbance rejection. [18]

A common approach to improve the force slew rate is to introduce a bias current (or flux ϕ). With a bias, the actuator may also be accurately modeled as linear. The disadvantage of operation with a bias is the associated ohmic loss in the coil ($IR^2 \propto \phi^2$), rotating hysteresis loss ($\propto \phi$), alternating hysteresis loss ($\propto \phi^{1.6}$), and eddy current loss ($\propto \phi^2$). [26]

For high speed rotating machinery, the eddy current loss is dominant; herein we refer to it as the rotating loss. This rotating loss may result in excessive rotor heating. Moreover, it results in decreased machine efficiency. Thus, operation without bias is appealing in applications where efficiency is critical, for example energy storage flywheels. [26]

2.7.3. GREATER USE OF THE AVAILABLE AIR GAP

Most industrial magnetic bearing systems use a large air gap during operation. A larger air gap (e.g. 1mm) results in greater actuator linearity near the centered position and thus simplifies control design and tuning.

However to reduce bearing size, weight and power consumption, it is desirable to use a smaller air gap during operation. For some applications, such as precision positioning platforms, the required motion may be large and use of a large air gap would be impractical. [18]

2.7.4. GENERALISED ACTUATION, SENSING AND CONTROL

Usually for every axis of motion there has been a devoted sensor, actuator, amplifier and control system. That is, each function of a magnet suspension has its own dedicated component. Recently there has been a shift away from this approach. For example, magnetic actuators are used to inductively sense position as well as to apply forces.

Motor and bearing functions are achieved with a single actuator. Direct digital control of amplifier switching is used to eliminate the separate amplifier servo-control loop, thus uniting the amplifier and rotor controllers. The advantages of these generalised actuation, sensing and control methods are reduced cost and increased design flexibility. [10]

2.7.5. CONTROL OF UNBALANCED RESPONSE

Control of unbalanced response is an area of intense research over the last decade. This is a considerably more mature area and substantial laboratory and industrial experience already exist. Generally the goal has been to reduce either the applied forces or the rotor vibration.

Herzog *et al.* propose a generalized notch filter which can be inserted into a multivariable feedback loop to reduce the response of the control system to rotor imbalance so as to avoid actuator saturation. [10]

2.8. SUMMARY

Magnetic bearings have structured themselves in bearing technology over the past few years. Industries, small companies and even the everyday man can benefit from the advantages of magnetic bearings.

High reliability, clean environments, high speed applications together with advantages in position and vibration control are only a few of the advantages of magnetic bearings.

Like any other bearing, magnetic bearings also have limitations. Larger bearings, higher complexity and higher cost are a few of the limitations of magnetic bearings.

CHAPTER 3
AXIAL AMB MODEL DESIGN

3.1. INTRODUCTION

When starting an axial AMB model design it is important to know the specifications of the model. These specifications together with the core dimensions will be used to obtain a theoretical design of the model. In the theoretical design the number of turns in the coil and the thickness of the copper wire can be calculated. This is then used to obtain the dimensions of the electromagnet.

To verify the calculations a finite element package (Quickfield®) is used. The design of the model is done in this package and the total flux density, strength and energy density is verified.

3.2. SPECIFICATIONS OF THE AXIAL AMB MODEL

In this section the mass of the rotor will be calculated and a summary of the specifications of the model will be provided in a table. From this table the number of turns needed for the coils and other important model parameters will be calculated.

Figure 3.1 provides the basic layout of the base and shaft. The aim is to vertically suspend a steel base between two electromagnets. For this purpose it was decided that a shaft should run through the middle of the steel base, thus keeping it from moving in the horizontal direction.

At start certain values was chosen for the radius and height parameters. The complete model design was then done. New radius and height parameters were chosen to best fit the current model and the process was repeated, until the optimum model was found.

For this design we will use the last radius and height parameters as starting values. They are as follow:

$$r_1 = 70 \text{ mm}$$

$$r_2 = 5 \text{ mm}$$

$$h_1 = 15 \text{ mm}$$

$$h_2 = 130 \text{ mm}$$

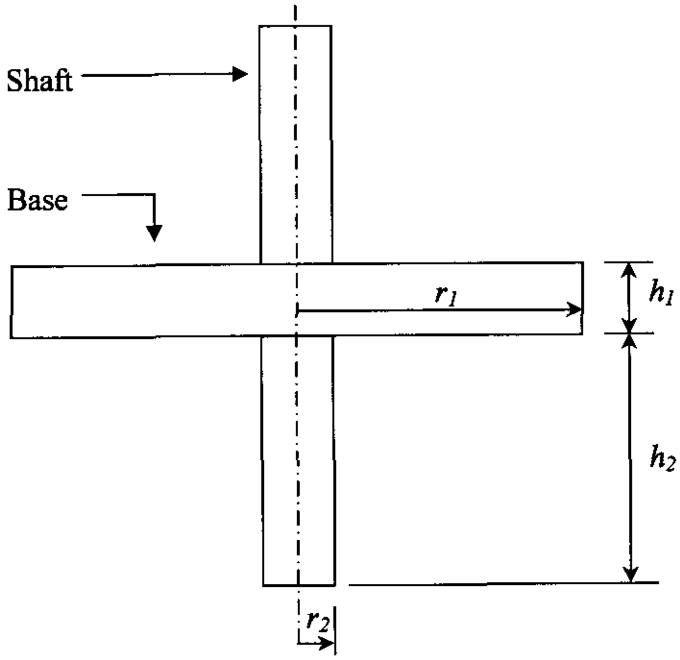

Figure 3.1: Rotor calculation

The volume of the complete rotor (base + shaft) is given by:

$$\begin{aligned} V_{rotor} &= (\pi \cdot r_1^2 \cdot h_1) + 2 \cdot (\pi \cdot r_2^2 \cdot h_2) \\ &= \pi \cdot 70^2 \cdot 15 + 2 \cdot \pi \cdot 5^2 \cdot 130\,\text{mm}^3 \\ &= 251327.4\,\text{mm}^3 \end{aligned}$$

The density of Bright steel is 7.8×10^3 kg/m^3, therefore the mass of the rotor (base + shaft) is:

$$\begin{aligned} m_{rotor} &= \rho \cdot V_{rotor} \\ &= (7.8 \times 10^3)(251327.4 \times 10^{-9})\,\text{kg} \\ &= 1.96\,\text{kg} \\ &\approx 2\,\text{kg} \end{aligned}$$

Table 3.1 provides a summary of the model specifications for the design of the electromagnets. The design of the electromagnets is for steady state and the dynamics is verified in section 3.5.

SPECIFICATION	**PARAMETER**
Rotor base diameter	$2 \cdot r_1 = 140$ mm
Rotor shaft diameter	$2 \cdot r_2 = 10$ mm
Length of base	$h_1 = 15$ mm
Length of shaft	$h_2 = 260$ mm
Mass of rotor (base + shaft)	$m_{rotor} \approx 2$ kg
Working distance	$l = 3$ mm
Maximum attraction distance	$l_{max} = 6$ mm
Axial disturbance force	No specific force (System over-designed)

Table 3.1: Summary of model specifications

3.3. CORE DIMENSIONS

It was decided to use a pot core type of electromagnet with a centre hole due to the symmetrical nature of the force exerted on the rotor. The dimensions that have to be considered are shown in figure 3.2 with l_l the leakage flux path length and l the main flux inner and outer path length. From this figure it can be seen where and in what direction the magnetic flux flows.

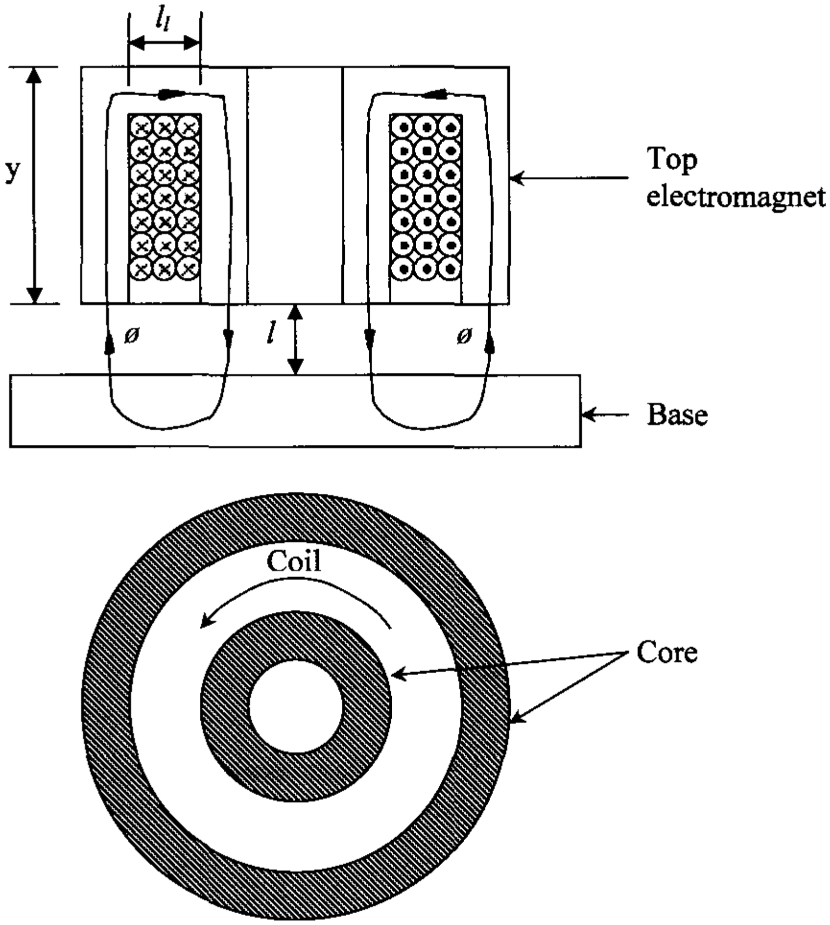

Figure 3.2: Basic structure of the magnet core

The y-dimension of the core will be determined as one of the design parameters when the window area needed for the coil is determined. It is assumed that there will be leakage flux of 10%. Bearing this in mind and with the distance l given as a specification, the distance l_l must be chosen such that the leakage flux is only 10% of the main flux.

The only way this can be achieved, is to design the reluctances of the two flux paths to be equal. This is mainly attempted by keeping the air path lengths of the main flux and the leakage flux the same. To minimize the chances for the core material to saturate, steel with a maximum flux density of 1.8 T will be used. Figure 3.3 shows the dimensions of the core to be used.

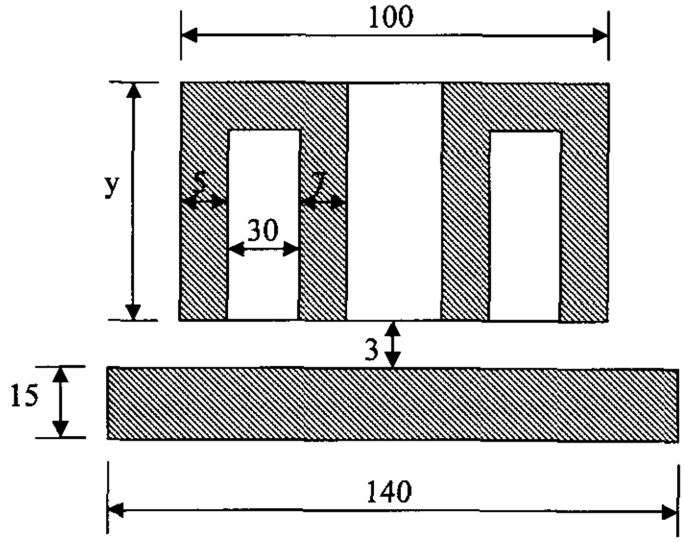

Figure 3.3: Dimensions of the core

3.4. THEORETICAL DESIGN

After the core has been specified for the magnet, the next step would be to determine the number of turns needed in the coil, to generate the required force to levitate the rotor at a distance of 3 mm and to attract it from a distance of 6 mm.

The force needed to lift the rotor is given by (1).

$$\begin{aligned} F &= mg \\ &= 2 \cdot 9.8 \\ &= 19.6\,\mathrm{N} \approx 20\mathrm{N} \end{aligned} \tag{1}$$

The inner area of the core (figure 3.4) is given by (2).

$$\begin{aligned} A_i &= \pi\,(r_2^2 - r_1^2) \\ &= \pi \cdot (0.015^2 - 0.008^2)\ \mathrm{m}^2 \\ &= 505.796 \times 10^{-6}\ \mathrm{m}^2 \end{aligned} \tag{2}$$

The outer area of the core is given by (3).

$$\begin{aligned} A_o &= \pi\,(r_4^2 - r_3^2) \\ &= \pi \cdot (0.05^2 - 0.045^2)\ \mathrm{m}^2 \\ &= 1.49 \times 10^{-3}\ \mathrm{m}^2 \end{aligned} \tag{3}$$

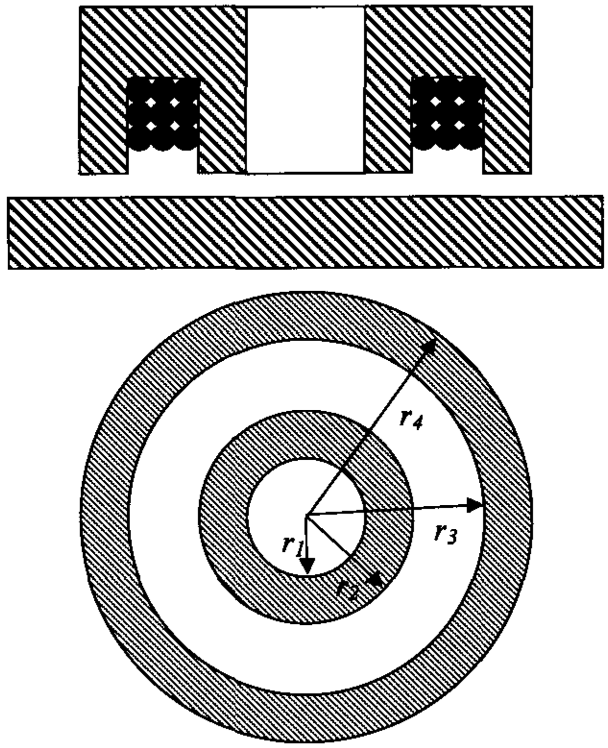

Figure 3.4: Area of the core

The flux required to lift the rotor is determined using (4).

$$\begin{aligned}
F &= mg = F_i + F_o \\
&= \frac{\phi^2}{2\cdot\mu_o\cdot A_i} + \frac{\phi^2}{2\cdot\mu_o\cdot A_o} \\
&= \frac{\phi^2}{2\cdot\mu_o}\left[\frac{1}{A_i}+\frac{1}{A_0}\right] \\
\therefore \phi &= \sqrt{2\cdot F\cdot\mu_0\cdot\left[\frac{1}{A_i}+\frac{1}{A_o}\right]^{-1}} \\
&= \sqrt{2\cdot 20\cdot 4\pi\times10^{-7}\cdot 377.61\times10^{-6}}\ \text{Wb} \\
&= 137.77\times10^{-6}\ \text{Wb}
\end{aligned} \tag{4}$$

where A_i is the inner core area, A_o is the outer core area, μ_o is the permeability of free space and $\o$ is the flux required to lift the rotor.

Due to the 10% flux leakage assumed, the total flux required would be:

$$\begin{aligned}
\phi_t &= \frac{100}{90}\times\phi \\
&= \frac{10}{9}\times 137.77\,\mu\text{Wb} \\
&= 153.078\,\mu\text{Wb}
\end{aligned} \tag{5}$$

It is important to verify that the core of the electromagnet does not saturate. The flux density of the inner and outer core is calculated using (6).

$$
\begin{aligned}
B_i &= \frac{\phi_t}{A_i} & \qquad B_o &= \frac{\phi_t}{A_o} \\
&= \frac{153.078\times10^{-6}}{505.796\times10^{-6}}\,\mathrm{T} & &= \frac{153.078\times10^{-6}}{1.49\times10^{-3}}\,\mathrm{T} \\
&= 0.303\,\mathrm{T} & &= 0.103\,\mathrm{T}
\end{aligned}
\tag{6}
$$

The reason for the low flux density is because the model was over designed. For an optimum design, the inner and outer areas must be chosen much smaller. This will result in larger values of the flux density. The end result will be a more cost effective model.

From the B-H curve for Bright steel in figure 3.5, it can be seen that the core is far from saturation. From this curve it can be seen that bright steel saturates at approximately 1.8 T.

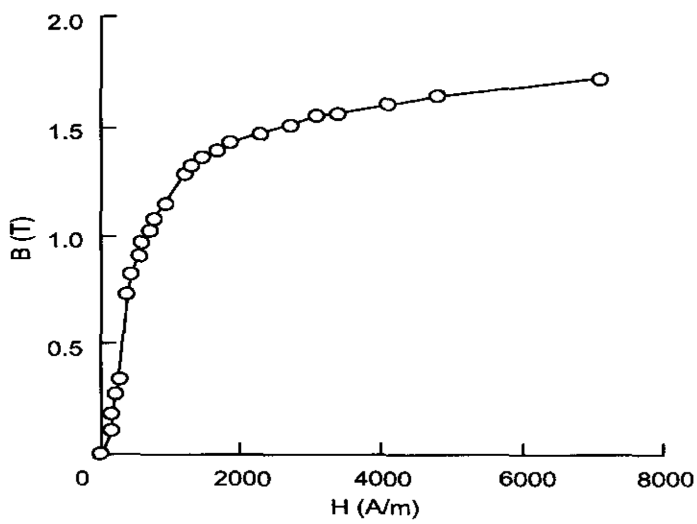

Figure 3.5: B-H curve of Bright Steel [21]

The equivalent magnetic circuit of the magnet is typically as given in figure 3.6 with $\mathscr{R}_\ell$ the reluctance of the leakage flux path, $\mathscr{R}_i$ the reluctance of the inner flux path and $\mathscr{R}_o$ the reluctance of the outer flux path.

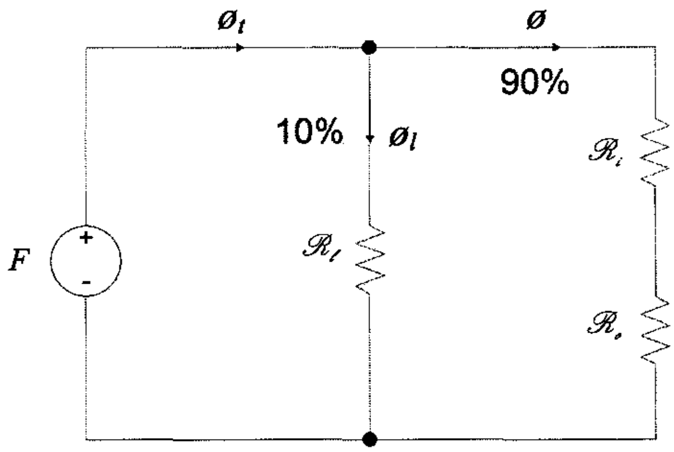

Figure 3.6: Magnetic circuit of the electromagnet

The total magnetomotive force (mmf) required to set up the desired flux in the airgap is given by

$$F = \phi_t \cdot \mathscr{R}_t \tag{7}$$

with ϕ_t the total flux in the circuit and $\mathscr{R}_t$ the total reluctance.

The reluctance of the inner air path is given by (8).

$$\begin{aligned} \mathscr{R}_i &= \frac{l}{\mu_0 A_i} \\ &= \frac{0.006}{4\pi \times 10^{-7} \cdot 505.796 \times 10^{-6}} \text{ At/Wb} \\ &= 9.44 \times 10^6 \text{ At/Wb} \end{aligned} \tag{8}$$

The reluctance of the outer air path is given by (9).

$$\begin{aligned} \mathscr{R}_o &= \frac{l}{\mu_0 A_o} \\ &= \frac{0.006}{4\pi \times 10^{-7} \cdot 1.49 \times 10^{-3}} \text{ At/Wb} \\ &= 3.204 \times 10^6 \text{ At/Wb} \end{aligned} \tag{9}$$

Since a 10% leakage flux is assumed the reluctance of the leakage path must be 10% of the reluctance of the main path. The reluctance of the main flux path is the sum of $\mathscr{R}_i$ and $\mathscr{R}_o$.

$$\begin{aligned} \mathscr{R} &= \mathscr{R}_i + \mathscr{R}_o \\ &= 12.644 \times 10^6 \text{ At/Wb} \end{aligned} \tag{10}$$

The reluctance of the leakage path is thus is given by:

$$\phi_l = \frac{\mathcal{R}_i + \mathcal{R}_e}{\mathcal{R}_i + \mathcal{R}_e + \mathcal{R}_f} \cdot \phi_t$$
$$\therefore \mathcal{R}_f = [\mathcal{R}_i + \mathcal{R}_e]\left[\frac{\phi_t}{\phi_l} - 1\right] \tag{11}$$
$$= 0.1137 \times 10^9 \text{ At/Wb}$$

The total reluctance $\mathcal{R}_t$ is then given by (12).

$$\mathcal{R}_t = \left[(\mathcal{R}_i + \mathcal{R}_e)^{-1} + (\mathcal{R}_f)^{-1}\right]^{-1} \tag{12}$$
$$= 11.378 \times 10^6 \text{ At/Wb}$$

Using (7) it is determined that:

$$F = \phi_t \cdot \mathcal{R}_t$$
$$= 153.078 \times 10^{-6} \cdot 11.378 \times 10^6 \text{ At} \tag{13}$$
$$= 1.742 \times 10^3 \text{ At}$$

The number of turns in the coil is determined by using (14).

$$F = N \cdot I \tag{14}$$

A current of 1 A is chosen since it can easily be supplied. It would however be necessary to verify that the coil inductance does not impair the control performance. The choice of 1 A current results in the number of turns to be, N = 1742. Therefore 1750 turns was chosen for each coil.

The current density (J) in the wire is chosen to be 3 A/mm^2. The diameter of the wire d_w can thus be calculated using (15).

$$d_w = \sqrt{I \cdot \frac{4}{J \cdot \pi}}$$
$$= \sqrt{1 \cdot \frac{4}{3 \cdot \pi}} \text{ mm} \tag{15}$$
$$= 0.652 \text{ mm}$$
$$\approx 0.7 \text{ mm}$$

Copper wire with a diameter of 0.7 mm is therefore selected to be used for the magnet coil.

To determine the steady state voltage needed for the electromagnet to operate, the resistance of the copper in the coil has to be determined. We have already specified the current at which the magnet will operate and thus the required voltage can be determined using Ohm's law.

We calculate the resistance of the wire by using equation (15) and therefore the cross sectional area (A_w) and the electrical resistivity of copper (ρ_w) has to be calculated, before the resistance of the wire can be calculated.

Average circumference of the coil:

$$\begin{aligned} C_{ave} &= 2\pi r_{ave} \\ &= 2 \cdot \pi \cdot 20 \text{ mm} \\ &= 125.66 \text{ mm} \end{aligned} \tag{16}$$

The length of wire needed is given by:

$$\begin{aligned} l_w &= C_{ave} \cdot N \\ &= 125.66 \times 10^{-3} \cdot 1750 \text{ m} \\ &= 220 \text{ m} \end{aligned} \tag{17}$$

The cross sectional area of wire is therefore:

$$\begin{aligned} A_w &= \pi \cdot r_w^{\ 2} \\ &= \pi \cdot (0.35)^2 \text{ mm}^2 \\ &= 384.8 \times 10^{-3} \text{mm}^2 \end{aligned} \tag{18}$$

The resistivity of copper at an assumed temperature of 50 °C is determined using (19).

$$\begin{aligned} \rho_c &= \rho_0 (1 + \alpha_c T) \\ &= 1.6 \times 10^{-6} (1 + 0.00393 \cdot 50) \ \Omega\text{m} \\ &= 19.22 \times 10^{-9} \ \Omega\text{m} \end{aligned} \tag{19}$$

The resistance of the coil is then given by:

$$\begin{aligned} R &= \frac{\rho_c \cdot l_w}{A_w} \\ &= \frac{19.22 \times 10^{-9} \cdot 220}{384.8 \times 10^{-9}} \ \Omega \\ &= 10.99 \ \Omega \end{aligned} \tag{20}$$

The steady state voltage needed for the coil can then be determined by:

$$\begin{aligned} V &= i \cdot R \\ &= 1 \cdot 10.99\,\text{V} \\ &= 10.99\,\text{V} \\ &\approx 11\,\text{V} \end{aligned} \tag{21}$$

The y-dimension of the core can now be determined. The total area A_{cu} of copper to be used in the coil is given by (22).

$$\begin{aligned} A_{cu} &= A_w \cdot N \\ &= 384.8 \times 10^{-3} \cdot 1750\ \text{mm}^2 \\ &= 673.4\ \text{mm}^2 \end{aligned} \tag{22}$$

To insert the coil into the pot core type electromagnet with a centre hole a bobbin with the dimensions given in figure 3.7 will be used. Due to the area taken up by the bobbin, the window width of the coil will be reduced to 28 mm.

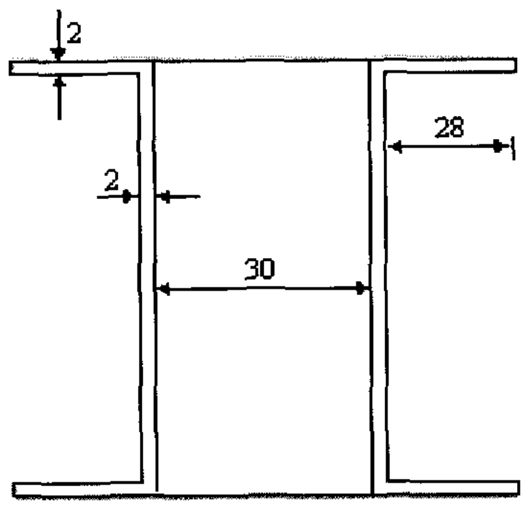

Figure 3.7: Coil-bobbin of electromagnet

The y-dimension, y_w, of the coil window is then calculated using (23) with K the filling factor taken as 0.47.

$$\begin{aligned} y_w &= \frac{A_{cu}}{x_w \cdot K} \\ &= \frac{673.4}{28 \cdot 0.47}\ \text{mm} \\ &= 51.1\,\text{mm} \\ &\approx 51\,\text{mm} \end{aligned} \tag{23}$$

The inductance of the electromagnet is calculated by (24).

$$\begin{aligned} L &= \frac{N^2 \mu_0 A_l}{l} \\ &= \frac{1750^2 \cdot 4\pi \times 10^{-7} \cdot 997 \times 10^{-6}}{2 \cdot 3 \times 10^{-3}} \\ &= 639.48\,\mathrm{mH} \end{aligned} \tag{24}$$

The final dimensions of the electromagnet can be found in figure 3.8. All the values are given in mm.

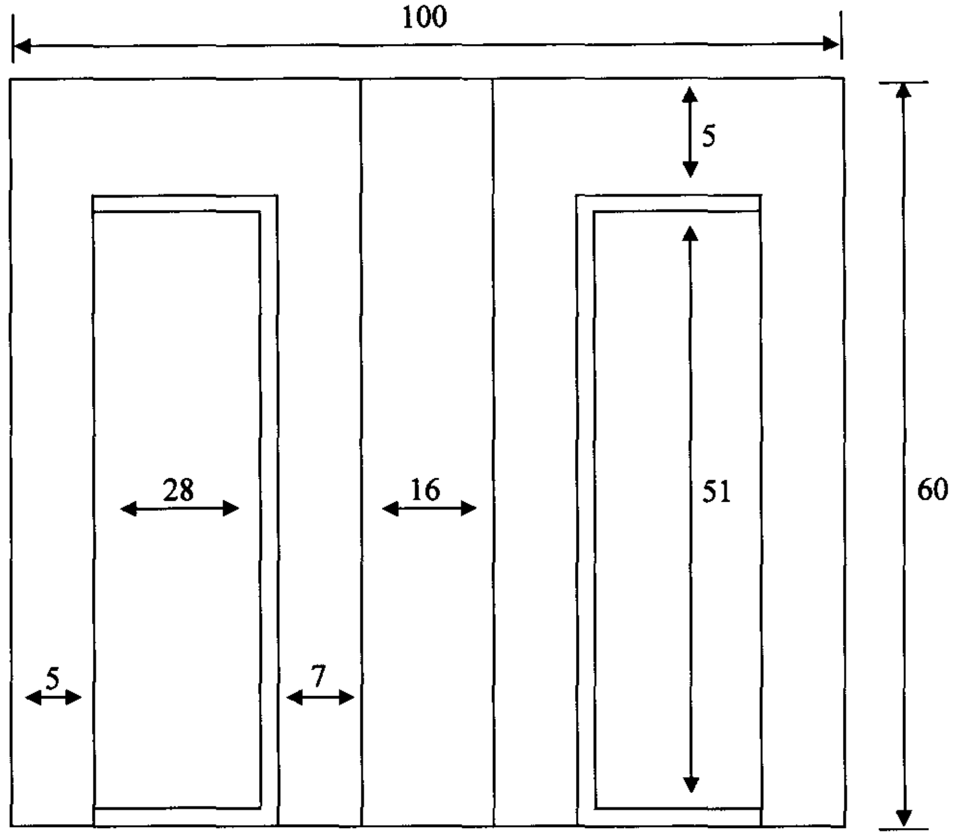

Figure 3.8: Final dimensions of the electromagnet

Table 3.2 provides a summary of the potential, current and inductance with an air gap of 3 mm and 6 mm. These values will be used in the design of the controller.

AIR GAP (X)	POTENTIAL (V)	CURRENT (I)	INDUCTANCE (L)
3 mm	6.59 V	0.6 A	639.48 mH
6 mm	10.99 V	1 A	319.74 mH

Table 3.2: Summary of the steady state value at 3 mm and 6 mm.

3.5. QUICKFIELD® ANALYSIS AND DESIGN VERIFICATION

This section provides analysis information about the electromagnet. The tests were performed using finite element analysis software called Quickfield®. This educational software has a limitation of 200 nodes on the mesh and thus the model had to be broken up in pieces to be analysed.

The Cartesian coordinate system was used and the model was created using the dimensions defined in figure 3.8. Edge labels and vertex labels was created using the magnetic potential equation $A = A_0$, where $A_0 = 0x + 0y$ Wb/m. Three main data block sets were chosen namely: Air, Coil and Steel. The following values were used for each.

3.5.1. AIR

Table 3.3 provides the air parameters.

SPECIFICATIONS	PARAMETERS
Permeability (relative parameters)	$\mu_x = 1, \mu_y = 1$
Area (Simulated window area)	$S = 277$ cm^2
Field source	$i = 0$ A/m^2
Electrical charge density	$\rho = 0$ C/m^3
Magnitude and directional coercive force of magnet	$M_{cf} = 0$ A/m, $D_{cf} = 0$ Deg

Table 3.3: Parameters of the air

3.5.2. COIL

Table 3.4 provides the parameters used for the coil.

SPECIFICATIONS	PARAMETERS
Permeability (relative parameters)	$\mu_x = 1, \mu_y = 1$
Area (Simulated window area)	$S = 14.28$cm^2
Field source current density	$I = 1750$ Ampere-turns
Conductor's connected	In parallel
Magnitude and Directional coercive force of magnet	$M_{cf} = 0$ A/m, $D_{cf} = 0$ Deg

Table 3.4: Parameters of the coil

3.5.3. STEEL

Figure 3.9 provides the B-H curve used for the steel.

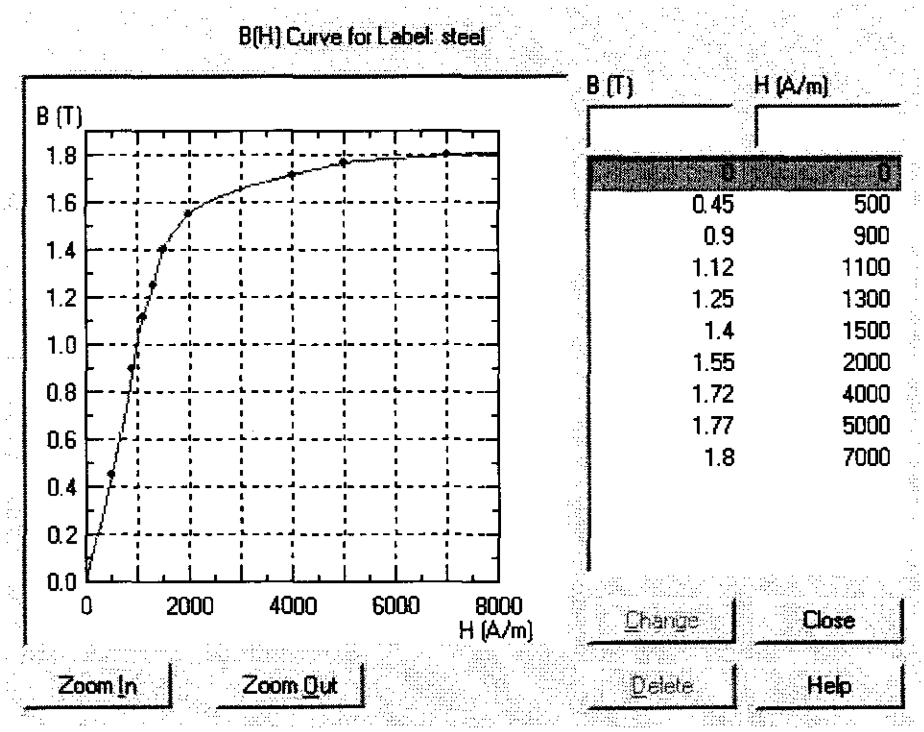

Figure 3.9: B-H Curve for steel

3.6. RESULTS OBTAINED USING QUICKFIELD®

Results were obtained by analysing the model at different local values and contour integral paths. Figure 3.10 provides a magnetic vector potential plot of the model. Only one half of the electromagnet was used for analysis. This half of the electromagnet has a C-shape.

From figure 3.10 it is clear that the maximum potential is inside the C-shape electromagnet. The right side of figure 3.10 provides a color spectrum of the magnetic vector potential A. The value of A is used to determine the magnetic flux density, magnetic field strength and energy density.

Figure 3.10 also shows the magnetic flux distribution. The distance between the flood lines increase with an increase in the distance from the electromagnet. The magnetic flux is the highest where the flux lines are the closest. This can be seen between the steel base and the electromagnet.

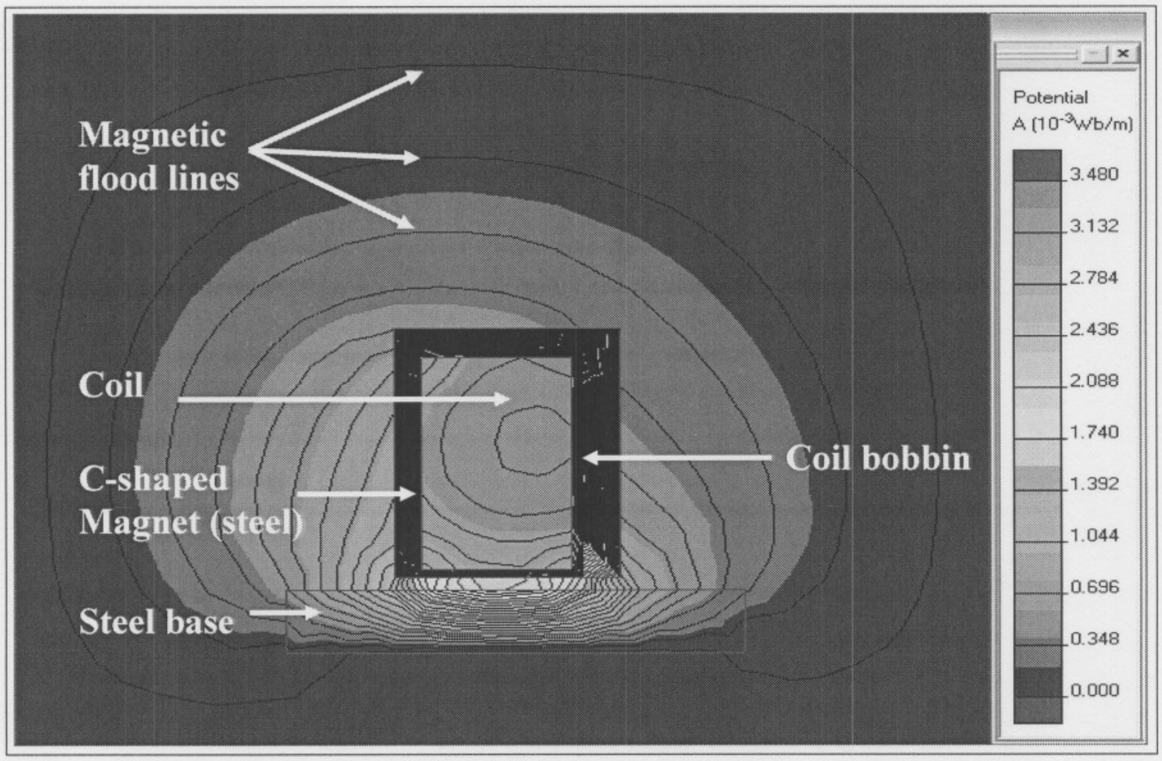

Figure 3.10: Potential plot[1]

The local values of the inner and outer core sections can be found in table 3.5. From this table it can be seen that the flux densities of the inner and outer core sections are way below the saturation point of Bright steel given as 1.8 T in figure 3.5.

SPECIFICATION	LOCAL VALUE CALCULATION (INNER CORE)	LOCAL VALUE CALCULATION (OUTER CORE)
Potential	$A = 0.0018812$ Wb/m	$A = 0.0012067$ Wb/m
Flux density	$B = 0.30714$ T	$B = 0.21597$ T
Strength	$H = 3221.6$ A/m	$H = 1298.9$ A/m
Energy Density	$w = 251.01$ J/m^3	$w = 75.348$ J/m^3
Permeability	$\mu_r = 75.869$	$\mu_r = 138.44$

Table 3.5: Local values of inner and outer core

Table 3.6 provides the contour integral path calculations. From this table the values of the mechanical force, mechanical torque, flux linkage per one turn, magnetomotive force and magnetic flux can be seen.

[1] This picture is available in full colour on the CD, available on request.

SPECIFICATION	CONTOUR INTEGRAL PATH CALCULATION
Mechanical force	$f = 54.742$ N $\varphi = 30.764$ °
Flux linkage per one turn	$\psi = 0.001642$ Wb
Magnetomotive force	$F = 844.05$ At
Magnetic flux	$\Phi = 206.6 \times 10^{-6}$ Wb

Table 3.6: Contour integral path calculations

The model has been simulated with a depth of 100 cm, but the real depth is only 31.42 cm ($2 \cdot \pi \cdot r_4$). Therefore the calculations obtained with the Quickfield® simulations must be fitted with a factor of 0.31.

If the areas A_i and A_o in equations (8) and (9) decreases with a certain factor, then the reluctance $\mathscr{R}$ will increase with a certain factor. This will result in a factor increase in the magnetomotive force F given by equation (13). The magnetomotive force obtained with Quickfield® is 844.05 At. If the values of the areas decrease, then the magnetomotive force obtained with Quickfield® will increase. This value will be close to the theoretical value of 1742 At.

If the areas A_i and A_o of equation (4) decrease then the magnetic flux $\o$ also decreases. The magnetic flux obtained with Quickfield® is 206.6 μWb. If this value is fitted with a factor of 0.31 the result is 65 μWb. This value does not correspond with the theoretical value of 153.078 μWb.

Appendix D provides graphs of the mesh of the complete system (figure D.1), potential (figure D.2), flux density (figure D.3), field strength (figure D.4), energy density (figure D.5) and permeability (figure D.6) for both the pot core type electromagnets. From these figures the forces exerted on the complete model can be viewed.

The total mechanical design of the axial AMB model can be found in Appendix C. In this appendix detailed dimensional drawings of the construction of the complete model and a 3-D drawing of the complete model can be viewed.

3.7. CONCLUSIONS

The depth parameter in Quickfield® can only be measured in block format and has a fixed value of 100 cm. This caused a problem in terms of the accuracy of the data obtained. The data had to be fitted by with a factor of 0.31. A further limitation of the Quickfield® software, was the limitation in the amount of nodes that can be used. The software used is a student version of Quickfield® and has a limitation of 200 nodes.

After fitting the data, the value obtained from Quickfield® for the magnetic flux does not closely agree with the theoretical data. The data obtained from Quickfield® only provides us with an estimate of what the magnetic flux must be and therefore the theoretical values will be used for future reference.

CHAPTER 4
INDUCTIVE SENSOR DESIGN

4.1. INTRODUCTION

In this chapter the design of the inductive position sensor is done. The sensor will measure the distance of the air gap and provide position feedback. The aim is to maintain a uniform air gap between the bottom and top electromagnets.

The sensors must be designed for a linear response between the position and the output voltage. The sensors must be noise insensitive, temperature independent and sensitive to any change in position.

4.2. POSITION SENSOR DESIGN

Figure 4.1 shows the inductive sensor configuration used to measure the position of the steel base. The focus is to keep the steel base in the middle of the two sensors, thus vertically suspending it. The inductances L_1 and L_2 in figure 4.1 is a function of the air gap length ($L_1 = L_0 \frac{d}{d-x}$ and $L_2 = L_0 \frac{d}{d+x}$). [15] The impedances thus change with a change in the air gap length. This change in impedance will be used to obtain a change in the position sensor output voltage.

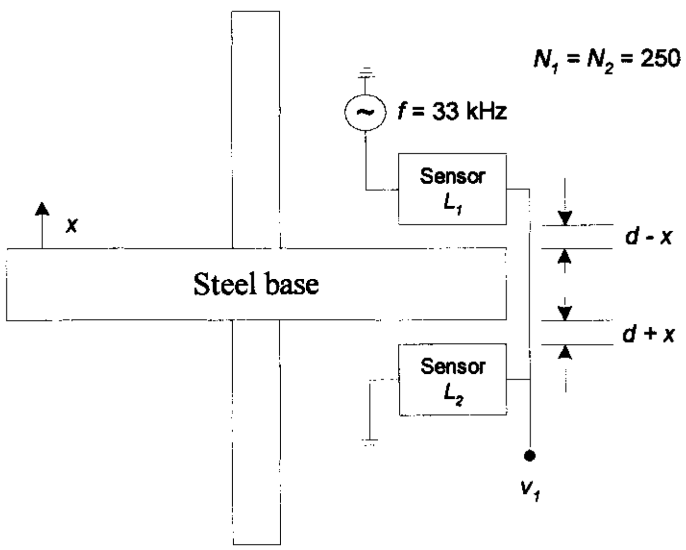

Figure 4.1: Position sensors in the AMB model [15]

4.3. DETAIL ON THE CIRCUIT DIAGRAM

Figure 4.2 shows the sensor block diagram. This diagram describes the basic principle of operation of the sensor. The complete position sensor circuit diagram can be found in Appendix B. This circuit will be used to measure the amplitude of v_1 (as shown in figure 4.1). The following explanation pertains to figure 4.2 and Appendix F.

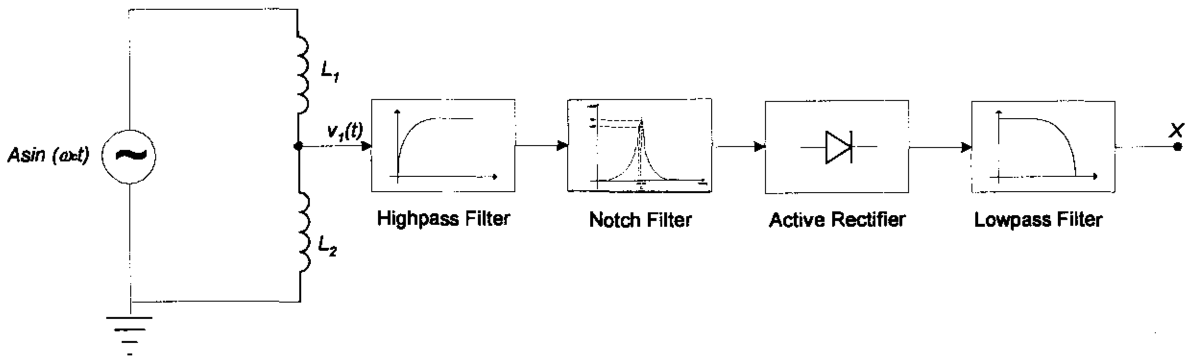

Figure 4.2: Sensor block diagram

A 33 kHz sinus wave is generated by a waveform generator (ICL8038). The signal generated has a THVD $\approx$ 1% and THID $\approx$ 1%. This signal is fed to a precision amplifier U2 (TL082). This amplifier is used as a follower to provide current to the two inductors L_1 and L_2.

These inductors are connected to function as a voltage divider. A difference in the inductance of L_1 or L_2, provide a difference in the output signal $v_1(t)$. If the inductance of $L_2 > L_1$ then the new output signal $v_{1New}(t) > v_{1Old}(t)$ and the inverse, if $L_2 < L_1$ then $v_{1New}(t) < v_{1Old}(t)$.

This signal is fed to a precision amplifier U3 (TL082), which provides high input impedance and also helps not to overload the coils. Precision amplifier U4 is a second order Butterworth high pass filter. This amplifier filters out all the low frequency noise on the system.

Flux coupling takes place, because the position sensor coils and the electromagnet are located very close to each other. This problem is solved using a notch filter. Precision amplifier U5 (TL082) is a second order Butterworth band pass filter (also known as a notch filter).

The position signal is passed through the notch filter, while any noise from the electromagnetic coil is filtered. A Butterworth filter is used, because it has a flat amplitude response in the pass-band and a steep cut-off response in the stopband.

Precision amplifier U6 (TL082) is an active rectifier. The active rectifier functions as an ideal peak detector and provides a d.c. output that is smoothed using a 47 nF capacitor. A low pass filter (f_a = 1 kHz) and difference amplifier can be used to filter out any high frequencies and to center the output around zero. Precision amplifier U7 (TL082) is a non-inverting amplifier used to adjust the gain.

4.4. CHARACTERISTICS OF THE NOTCH FILTER

After the design calculations have been performed, tests must be performed on the notch filter to verify that it is working properly. For this purpose the maximum output amplitude of the notch filter was determined. A frequency spectrum around this maximum point is then plotted. This plot can be seen in figure 4.3.

From figure 4.3 it is clear that the center frequency is at ≈33 kHz and the –3dB points are at ≈29.5 kHz and ≈36.5 kHz. This corresponds with the chosen 7 kHz for the –3dB point, done during the design calculations. The 33 kHz centre frequency can also be seen in the phase plot of figure 4.3. The waveform generator can now be verified to see if it is working at 33 kHz.

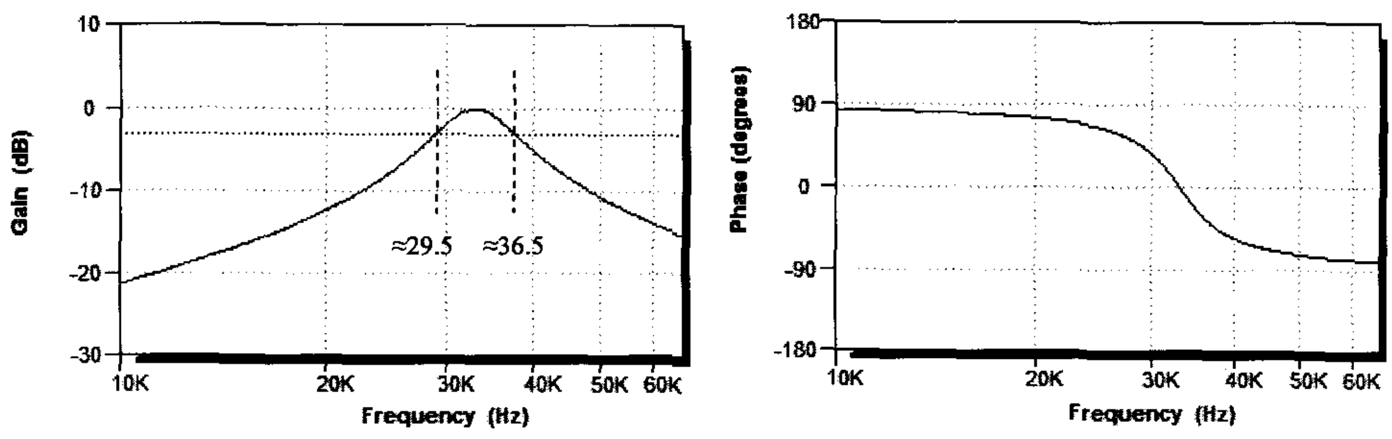

Figure 4.3: Characteristics of the notch filter

4.5. CHARACTERISTICS OF THE ACTIVE RECTIFIER

Figure 4.4 is an AM modulator that is used for the calculation of the characteristics of the active rectifier. The signal $v_1(t)$ of figure 4.2 is multiplied with a signal $Bsin(\omega_m t)$. The new signal $v_2(t)$ is then passed onto the highpass filter shown in figure 4.2. The frequency of the modulator (ω_m) is then varied and the output obtained can be seen in figure 4.5 and figure 4.6.

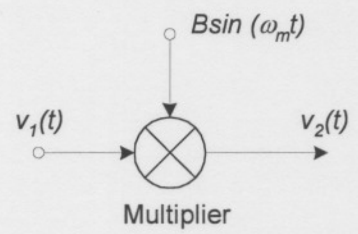

Figure 4.4: AM modulator

The purpose of the active rectifier is to convert the a.c. voltage to a d.c. voltage. With low frequency signal multiplication the result is a changing d.c. voltage proportional to the positive envelope of the rectified a.c. voltage. This can be seen in figure 4.5.

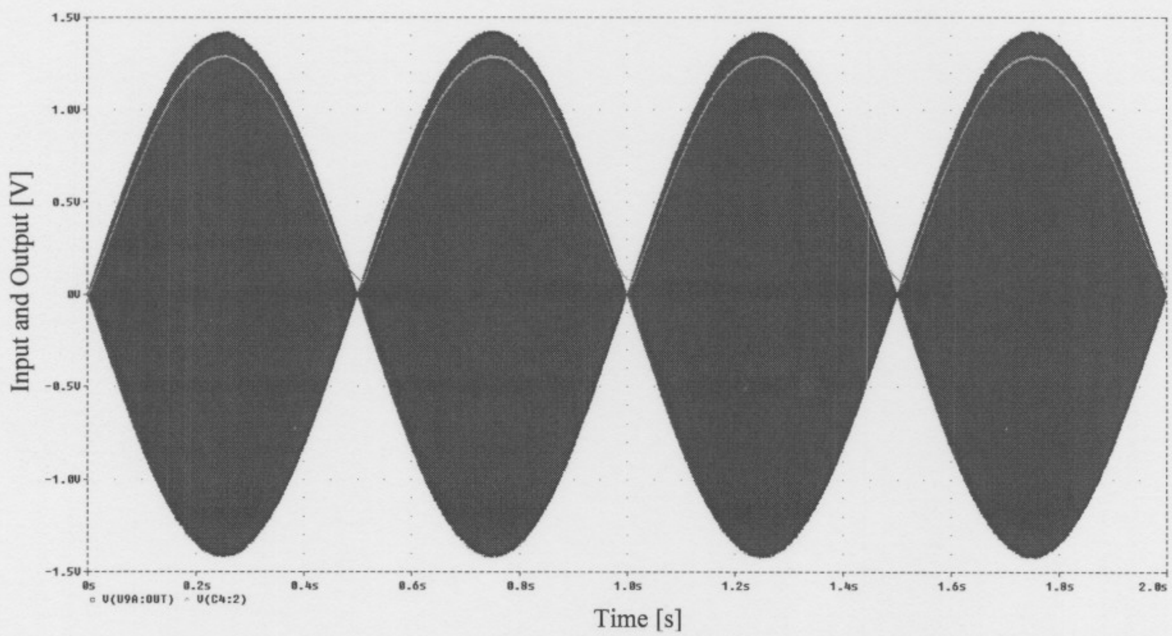

Figure 4.5: Active rectifier with low frequency signal multiplication

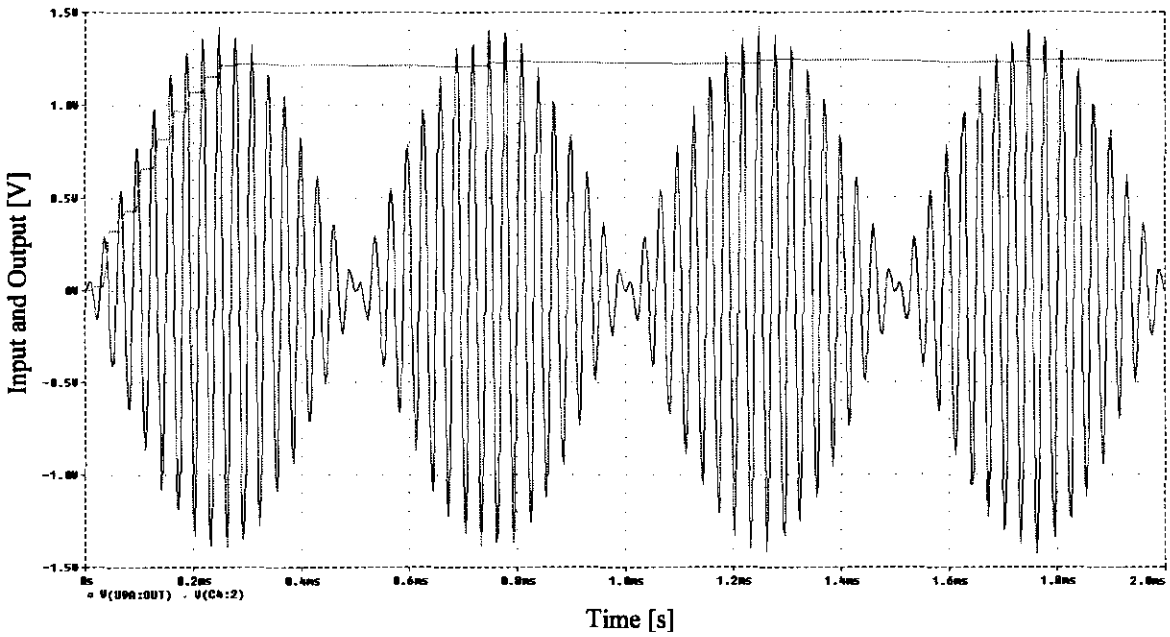

Figure 4.6: Active rectifier with high frequency signal multiplication

With high signal multiplication the output does not follow the input signal. A constant d.c. voltage on the positive envelope can be seen in figure 4.6.

4.6. RESULTS OBTAINED

Figure 4.7 provides a picture of the top half of the AMB. In this figure the direction of the magnetic fields can be seen. If the steel base in figure 4.7 moves towards the coil, then the inductance increases and the sensor output decreases.

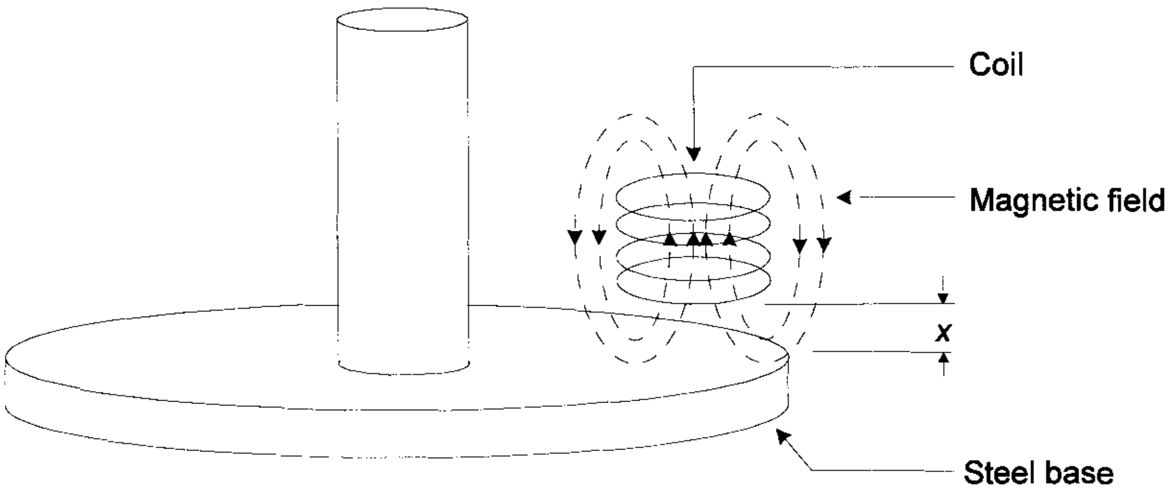

Figure 4.7: Top half of the AMB showing the magnetic fields

Figure 4.8 provides a graph of the output voltage (v) of the sensor with a change in the air gap distance (x). The data has a linear response. Therefore a straight line fitting can be done on these data. The resulting equation can be seen in the figure.

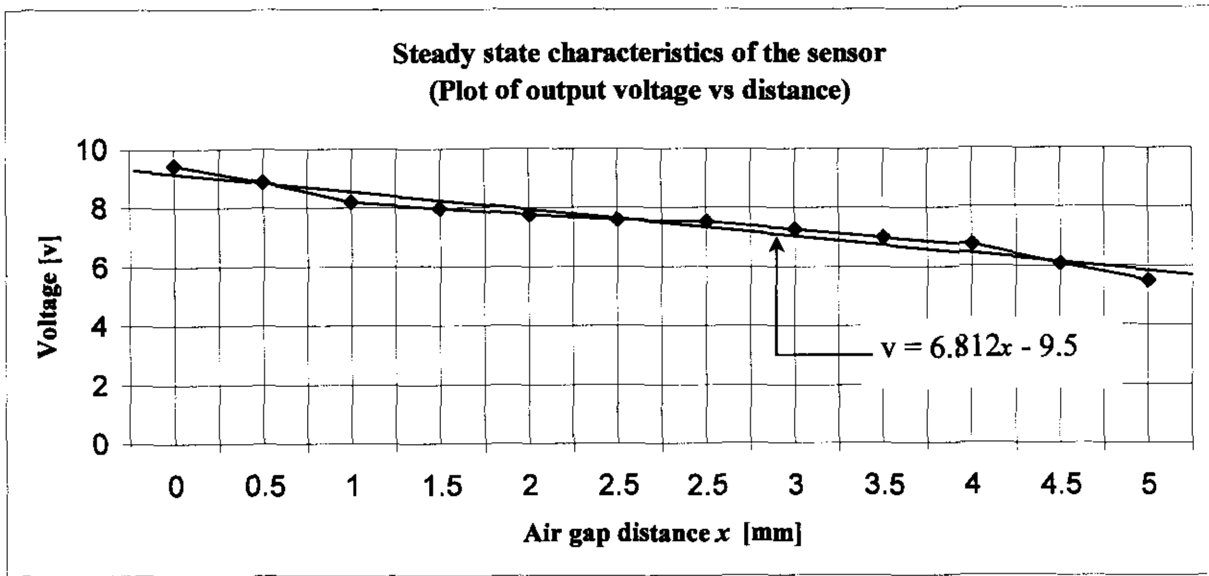

Figure 4.8: Plot of distance against output voltage for f = 33 kHz

The output voltage simulations of the sensors were done in PSPICE® and the results can be found in Appendix F. Figure F.1 gives the output of the sensor with $L_1 = L_2$. In this figure the input signal is 3 V, the signal measured at the output of the coils is 1.5 V and the output of the system is 7.5 V. When $L_1 < L_2$ the amplitude of the output signal increases and when $L_1 > L_2$ the amplitude decreases.

These results are verified with a digital oscilloscope. Figure G.1 gives the output of the sensor with $L_1 = L_2$. The d.c. output in this figure is 7.625 V. With the impedance $L_1 < L_2$ the output of the sensors increase and with the impedance $L_1 > L_2$ the output decreases.

Figure G.2 provides the sensor input and inductor output with $L_1 = L_2$. From this figure it can be seen that the input is 1.909 V and the output is 950 mV.

4.7. CONCLUSIONS

The position sensor is designed to measure the distance of the air gap between the steel base and the electromagnets. The distance between the air gap and the output voltage has a linear response. This makes it ideal to use the sensors over a wide air gap range. The output of the sensor will be used as input for the dSpace® controller card.

The position sensor can be used in various applications, because it is not dependent on temperature change, insensitive for dusty environments and sensitive to change in position. A disadvantage of the sensor is that it is sensitive to magnetic noise.

This noise can be classified in two categories, internal and external noise. The internal noise is generated by the system itself, which provides the main concern, because the magnetic bearing is one large nonlinear field.

The external noise is noise generated by any system in the vicinity of the sensor, like motors and generator which relies on magnetism. Therefore care must be taken to minimize these kind of noises.

Improvements on these sensors can be achieved by using a full wave rectifier instead of a half wave rectifier, using a higher order notch filter to obtain a faster cut-off frequency and increasing the signal to noise ratio (SNR) by using components less sensitive to noise in the specific frequency band.

CHAPTER 5
CONTROLLER DEVELOPMENT AND IMPLEMENTATION

5.1. INTRODUCTION

The focus of this chapter is the development and implementation of the controllers. In fulfilling this purpose, dynamics of the electromagnetic suspension model will first be done. Concepts about the static characteristics of the electromagnet and parameters used for dynamic modelling will be discussed.

The simulation design of the PID and lead controllers, followed by the analog design of the PID and lead controllers will then be done. The different components will be discussed and the necessary Bode diagrams and simulations will be done.

This chapter ends with the dSpace® implementation of the PID and lead controllers. The different component used for the simulation will be discussed and the simulation will be implemented to run as a real-time application.

5.2. ELECTROMAGNETIC SUSPENSION MODEL DYNAMICS

For any given current $i(t)$ in a winding with inductance L, the magnetic co-energy is $1/2L[i(t)]^2$. Thus if this winding is put on an electromagnet which is separated from a ferromagnetic object by a distance $z(t)$, the force of attraction between the two magnetised bodies is equal to the rate of change of co-energy with respect to the distance, i.e. $F_a = dW_m(t)/dz = d/dz\{\frac{1}{2}L(z)[i_m(t)]^2\}$ where $i_m(t)$ is the current through the magnet winding with nonlinear inductance $L(z)$.

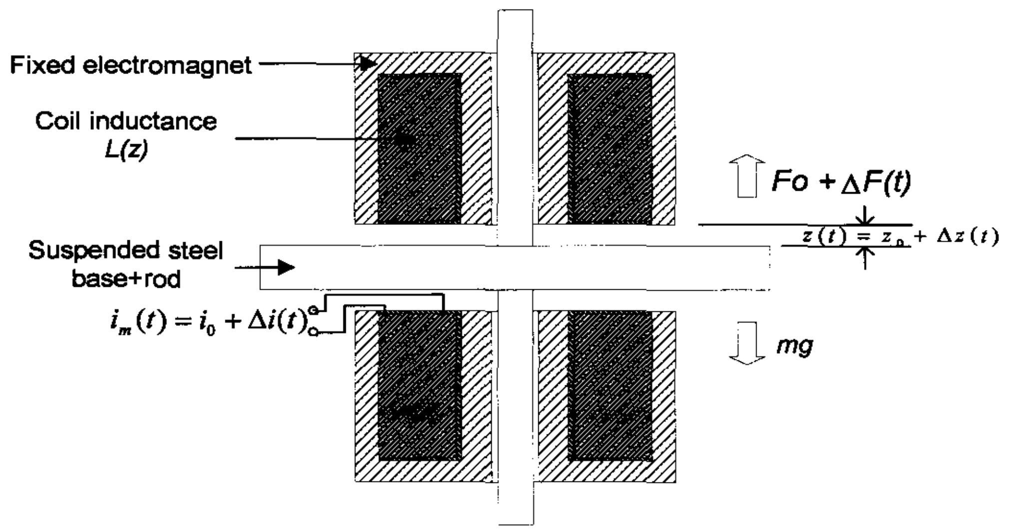

Figure 5.1: Parameters for dynamic modelling

If the magnet is fixed and a ferromagnetic object, of mass *m*, is free to move (figure 5.1) the force of attraction will be towards the electromagnet. Thus if the excitation current is independent of variations in winding inductance, the vertical motion of the suspended object is described by

$$m\ddot{z}(t) = F_a - mg = \frac{1}{2}[i_m(t)]^2 \frac{dL(z)}{dz} - mg$$

To obtain a linearised version of the above equation, the magnet current $i_m(t)$ may be assumed to have two parts: a steady-state component (i_0) which generates the vertical attraction force at an equilibrium point (i_0, z_0), and a much smaller component $\Delta i(t)$ which provides the attraction force for variations around (i_0, z_0). Thus for small perturbations Δi and Δz around this equilibrium point, the restoring force may be expressed as

$$\begin{aligned}\Delta F_a &= \frac{\partial F_a}{\partial i}\Delta i + \frac{\partial F_a}{\partial z}\Delta z \\ &\approx i_0 \left.\frac{dL(z)}{dz}\right|_{z_0} \Delta i + \frac{1}{2} i_0^2 \left.\frac{d^2L(z)}{dz^2}\right|_{z_0} \Delta z + second-order-terms\end{aligned}$$

Since the inductance *L(z)* is inversely proportional to the reluctance in the magnetic circuit, the constant k_{z1} is always negative. The above expression for the restoring force may also be derived through experimental force-distance-current characteristics of an electromagnet shown in figure 5.2. For very small excursions around a nominal operating point, the vertical attraction force may be expressed as $-\Delta f = k_{i2}\Delta i - k_{z2}\Delta z$ where the values of the slopes k_{i2} and k_{z2} may be obtained from the calibrations of the respective x and y axes.

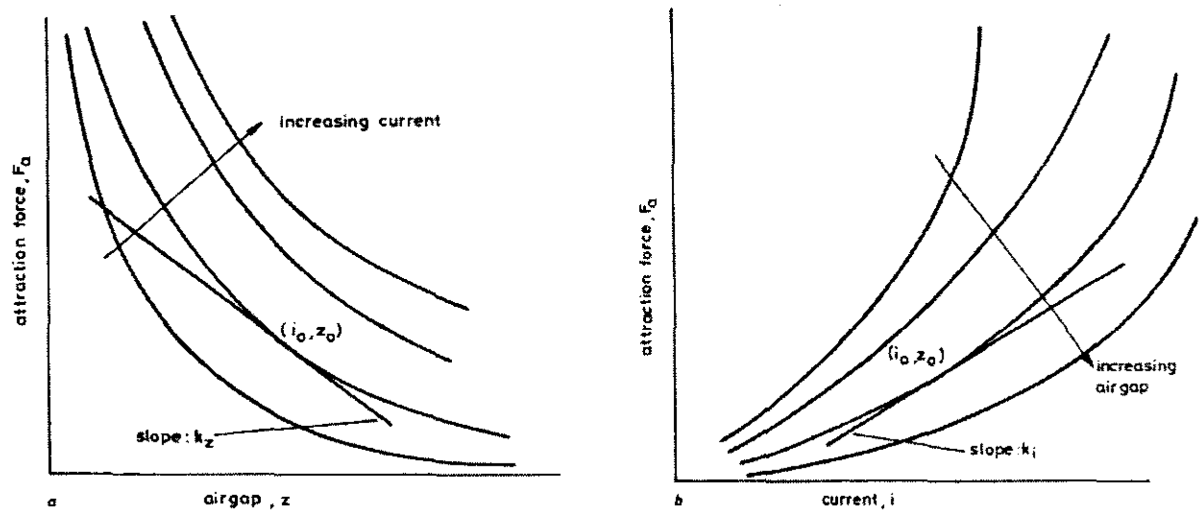

Figure 5.2: Static characteristics of the electromagnet [20]

a) Force-distance characteristics at constant current

b) Force-current characteristics at constant airgap

Thus if the movement of the suspended object in figure 5.1 is restricted within the linear force-current-distance curves, the linear motion of this electromagnetic suspension in the vertical direction is described by

$$mg = \frac{1}{2} i_0^2 \left.\frac{dL(z)}{dz}\right|_{z_0} \qquad \text{and} \qquad m\Delta \ddot{z}(t) = -k_i \Delta i(t) + k_z \Delta z(t)t$$

where

$$k_{i1} = k_{i2} = k_i \text{ and } k_{z1} = -k_{z2} = -k_z.$$

If a true current amplifier is used to generate the excitation current, then, in a first analysis, the magnet winding may be treated as a small resistance in series with the high output resistance of the power amplifier. Thus if R is the total resistance on the output side of the amplifier, the transfer function of the suspension system may be expressed as [6]

$$\Delta Z(s) = -\left[\frac{k_i}{ms^2 - k_z}\right]\frac{\Delta V(s)}{R}$$
$$= -\left[\frac{(kk_i)/m}{s^2 - (k_z/m)}\right]\Delta V(s)$$

where k is the voltage to current gain of the amplifier magnet combination. The above transfer function shows that a suspension system using ferromagnetic attraction forces is unstable in open-loop owing to the pole on the right-half s-plane $[+\sqrt{(k_z/m)}]$, and feedback of at least position (airgap) is needed to achieve stability.

5.3. SIMULATION DESIGN OF THE PID CONTROLLER

The complete axial AMB system is composed of two magnetic coils, two actuating units, two position sensors and a steel disc suspended by magnetic forces. This principle is shown in figure 5.3.

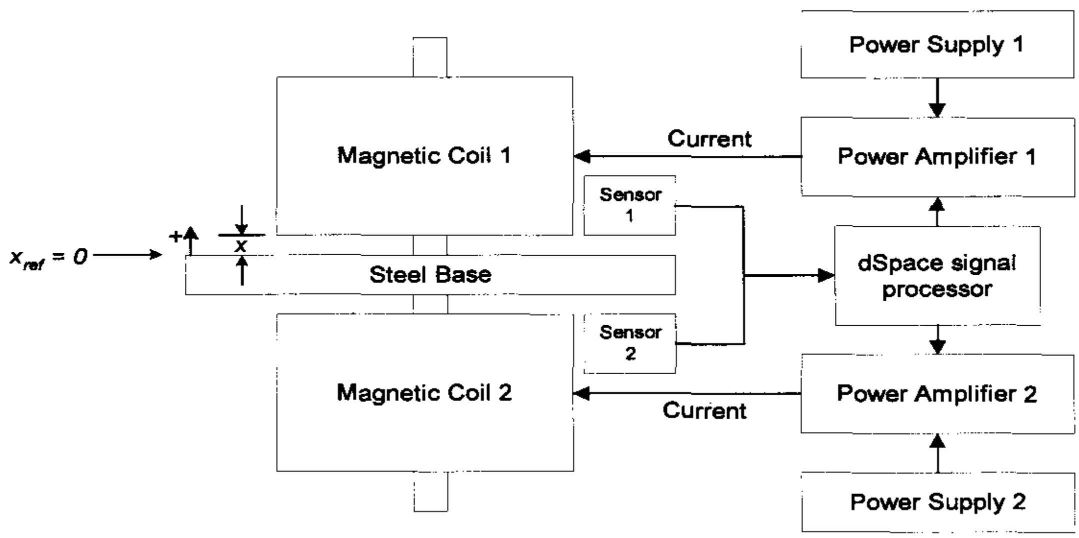

Figure 5.3: Complete AMB system

A position sensor measures the position of the steel base from a reference position. The control output determines the current that the actuating unit must supply to the magnet. The electro-mechanical part of the axial AMB system can be described using a force equation. The nonlinear single-input-single-output is represented by the state-space model:

$$\dot{x}_1 = x_2$$
$$\dot{x}_2 = 1/m \cdot f(x_1, u)$$
$$y = x_1$$

where u is the current input, m the mass of the steel disc. $f(x_1,u)$ is a nonlinear function and shown in figure 5.4.

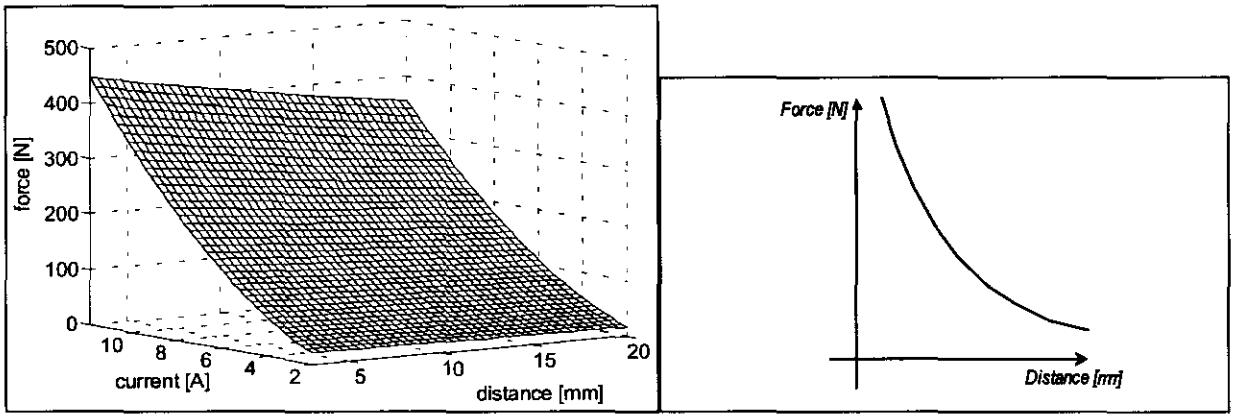

Figure 5.4: Nonlinear AMB characteristics [11]

Because of the highly nonlinear system it is normally linearised at an operation point:

$$m\ddot{x} = k_i i + k_s x + F_e - mg$$

where x is the air gap between the steel base and the magnetic coil, F_e is the external disturbance force, k_i is the current gain and k_s is the position stiffness. This equation can be presented as a block diagram with positive feedback of k_s. This means that the system is unstable without a feedback controller. [8], [11]

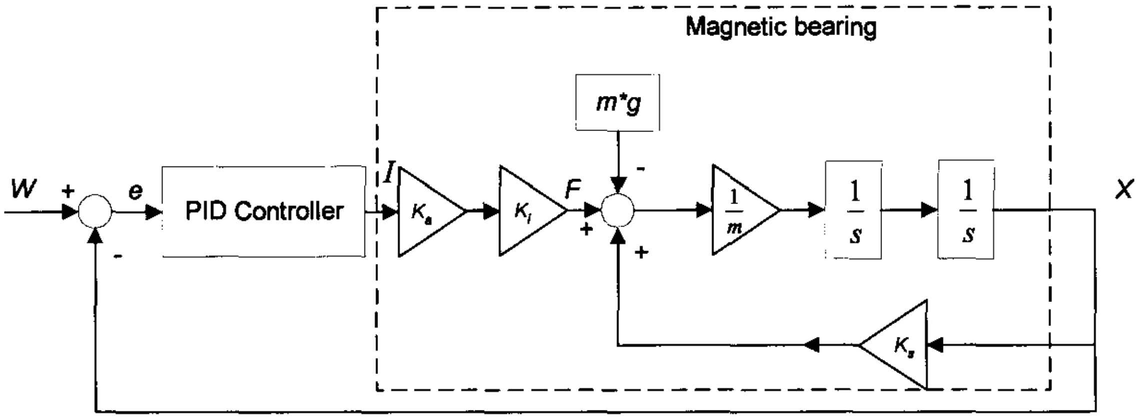

Figure 5.5: Linear block diagram of the AMB system with one controller

The force equation has two states so that a PD controller should be sufficient. However, to eliminate a steady state error a PID-controller is needed. The control system usually contains a current controller too, but because of the small time constant compared to the rest of the system it can be neglected. Figure 5.5 gives a linear block diagram of the AMB system with only one PID controller.

From figure 5.5 the complete system with two PID controllers can be designed. Figure 5.6 provides a block diagram where both PID controllers are implemented. PID controller 1 is for control of the top electromagnet and PID controller 2 is for the bottom electromagnet.

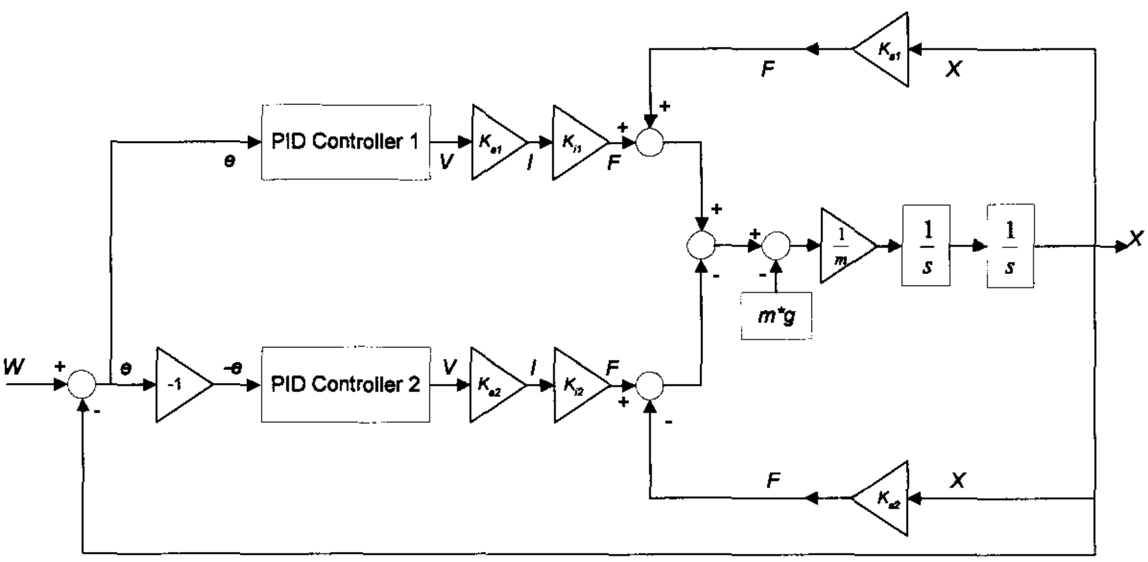

Figure 5.6: Block diagram of the AMB system with both PID controllers

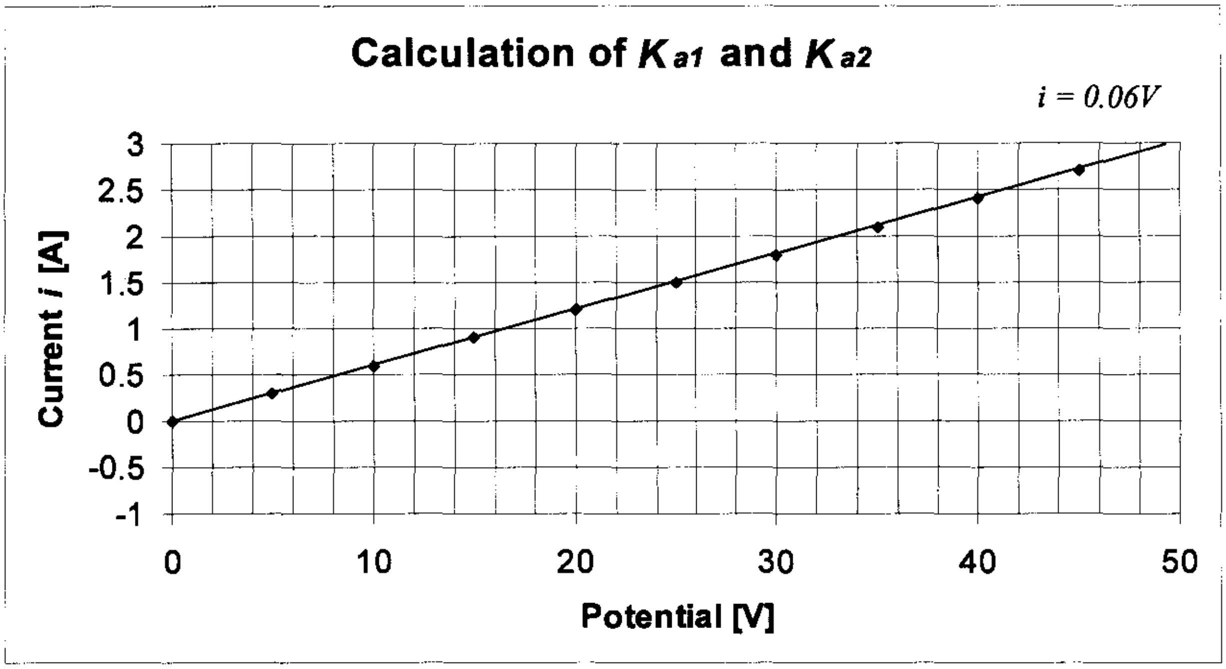

Figure 5.7: Calculation of K_{a1} and K_{a2}

From figure 5.6 the simulation model can be created. Figure 5.7 provides a graph of the current versus potential. A straight line fit provides the equation $i = 0.06\ V$. The equation $F_a = 79.2i - 20$ for the K_{i1} constant is obtained from figure 5.8. K_{i1} is the current gain of the top electromagnet and a working current of 0.5 A was chosen.

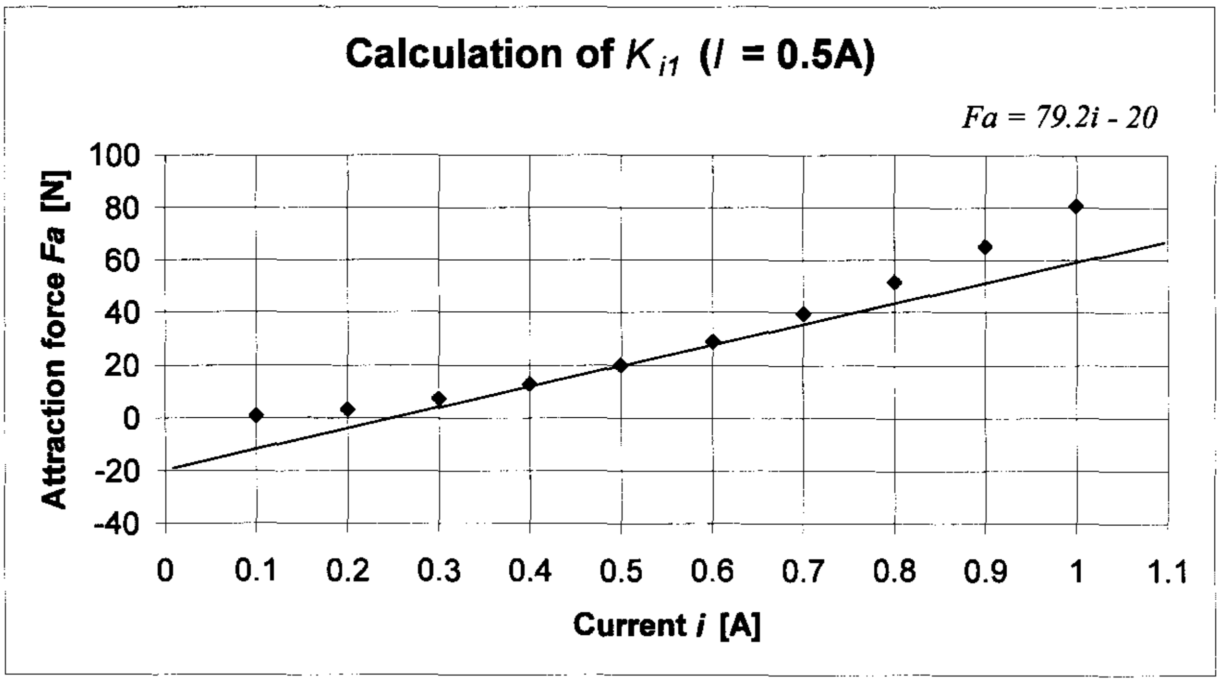

Figure 5.8: Calculation of K_{i1} for $I = 0.5$A

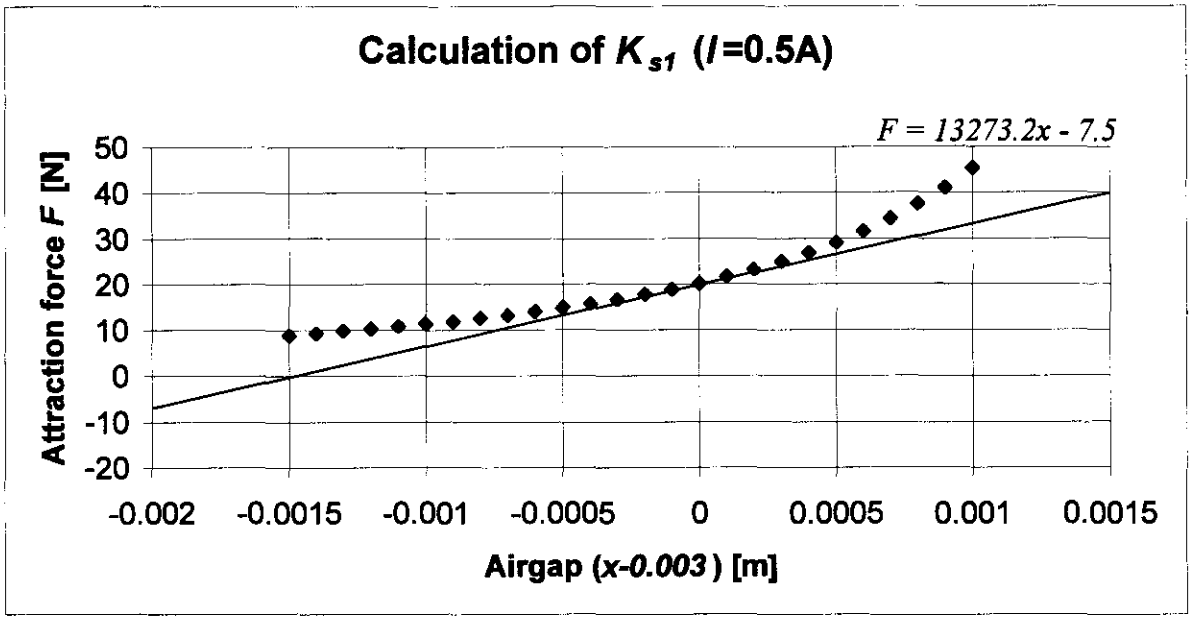

Figure 5.9: Calculation of K_{s1} for $I = 0.5$A

Figure 5.9 provides the equation $F = 13273.2x - 7.5$ for the straight line fitted through the data. The constant K_{s1} is the position stiffness for the top electromagnet and the working current was chosen at 0.5 A.

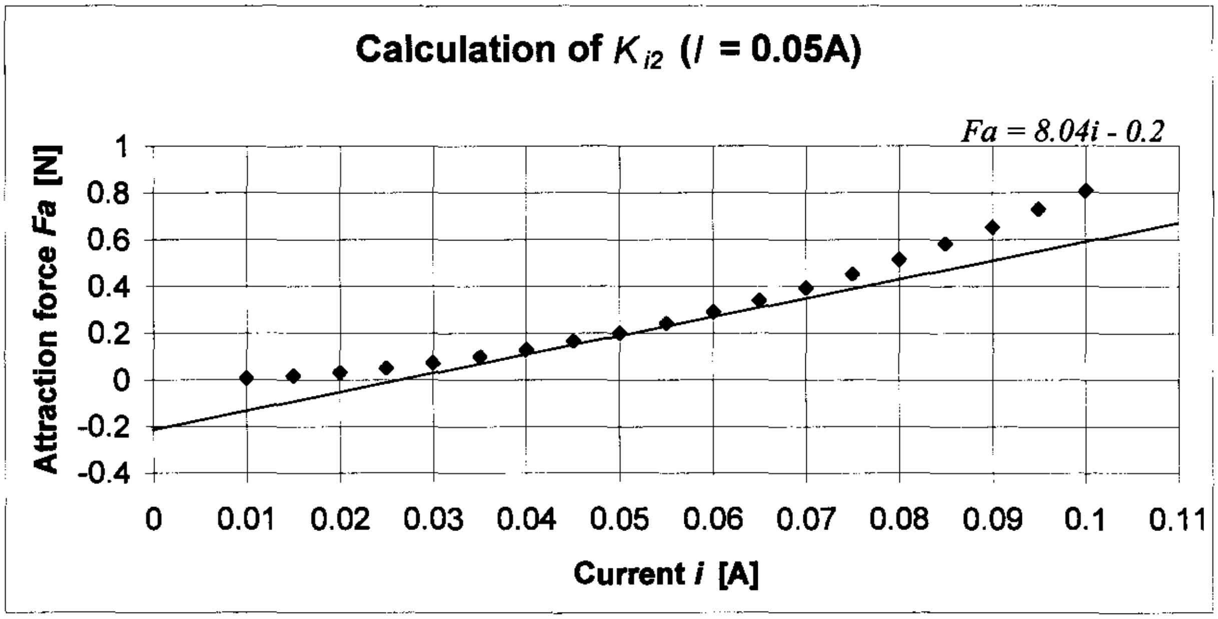

Figure 5.10: Calculation of K_{i2} for $I = 0.05$A

From figure 5.10 the relation between current and attraction force are obtained. K_{i2} is the current gain for the bottom electromagnet and it was chosen to work with a current of 10 times smaller, because of the gravitational force adding up with this electromagnet. The current is chosen at 0.05A. The straight line fitting provides an equation $F_a = 8.04i - 0.2$.

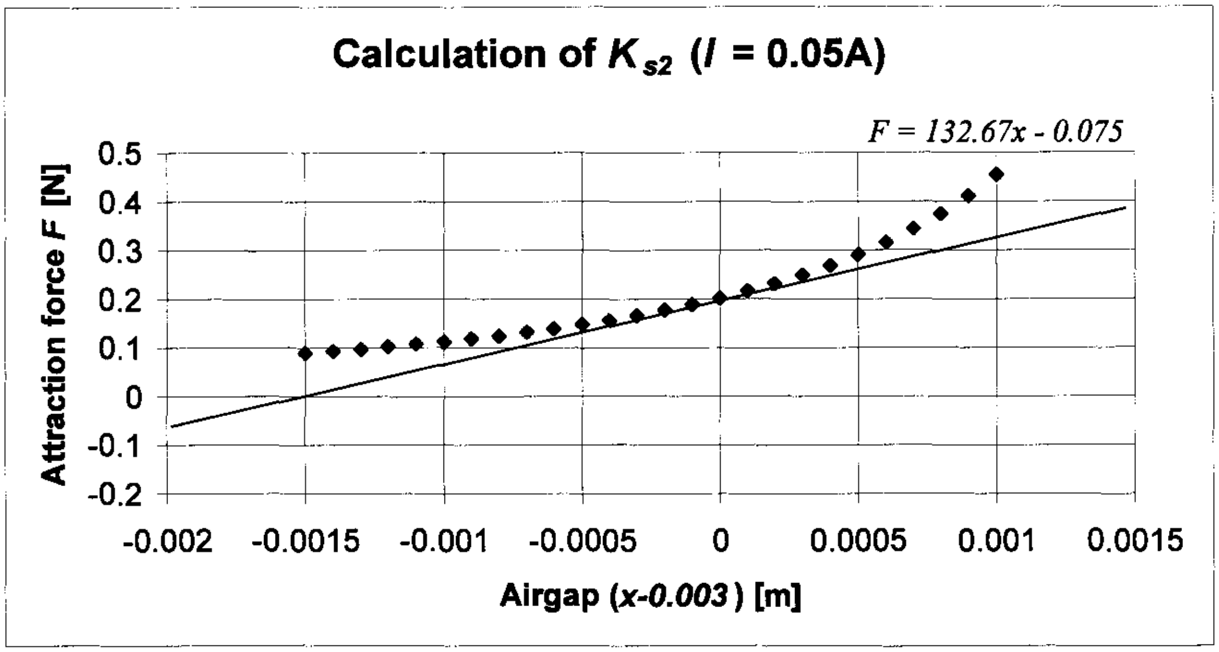

Figure 5.11: Calculation of K_{s2} for $I = 0.05$A

The equation $F = 132.67x - 0.075$ was obtained with the straight line fitting of the data in figure 5.11. K_{s2} is the position stiffness for the bottom electromagnet. The current was chosen at 0.05 A.

Figure 5.12 provides the complete simulation model. This model will be used to obtain the correct constants for the PID controllers that will be used in the real-time simulation model. Different constants were implemented and the model was simulated using a signal generator with a square wave as input for the system. The best result obtained can be seen in figure 5.13.

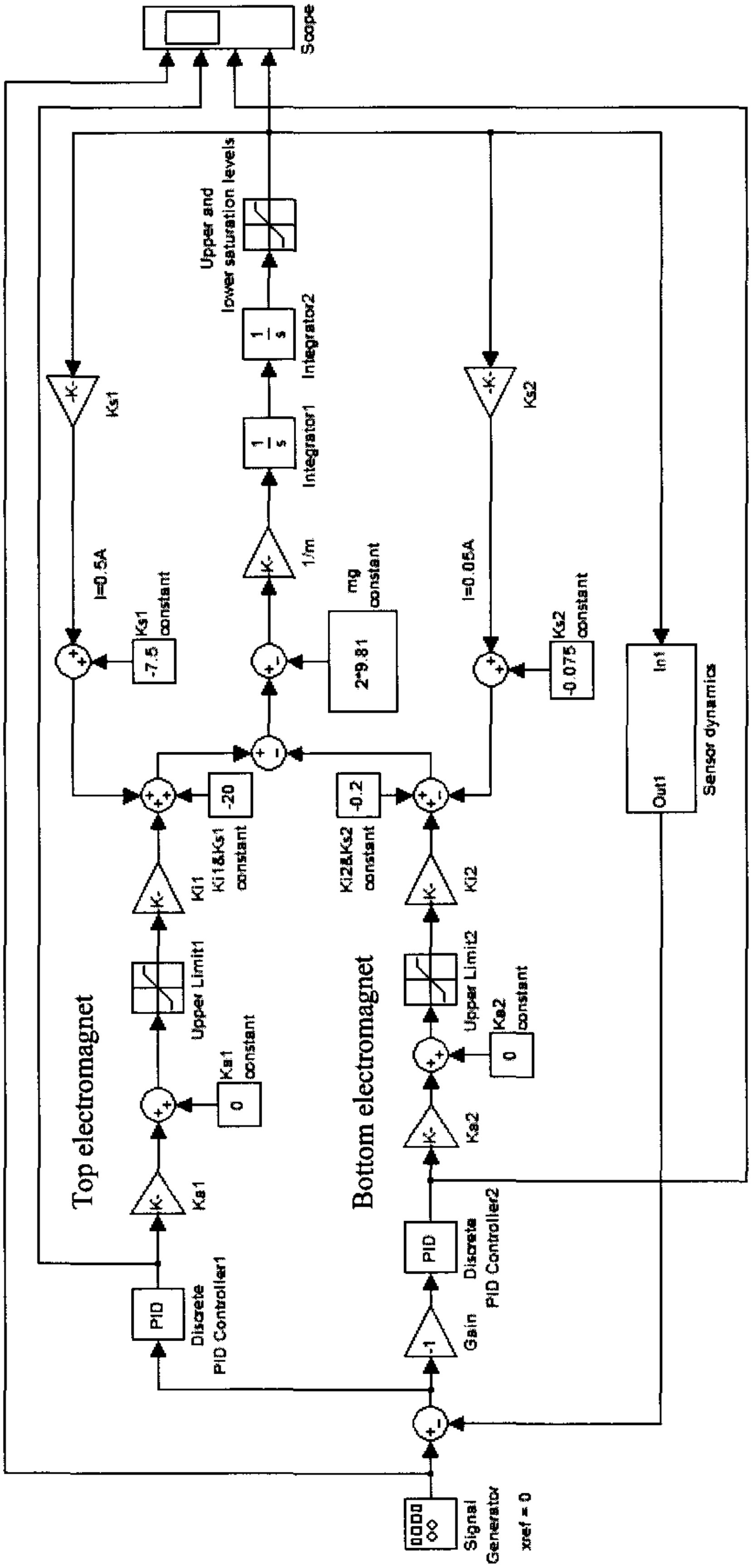

Figure 5.12: Complete Simulink® model with discrete PID controllers

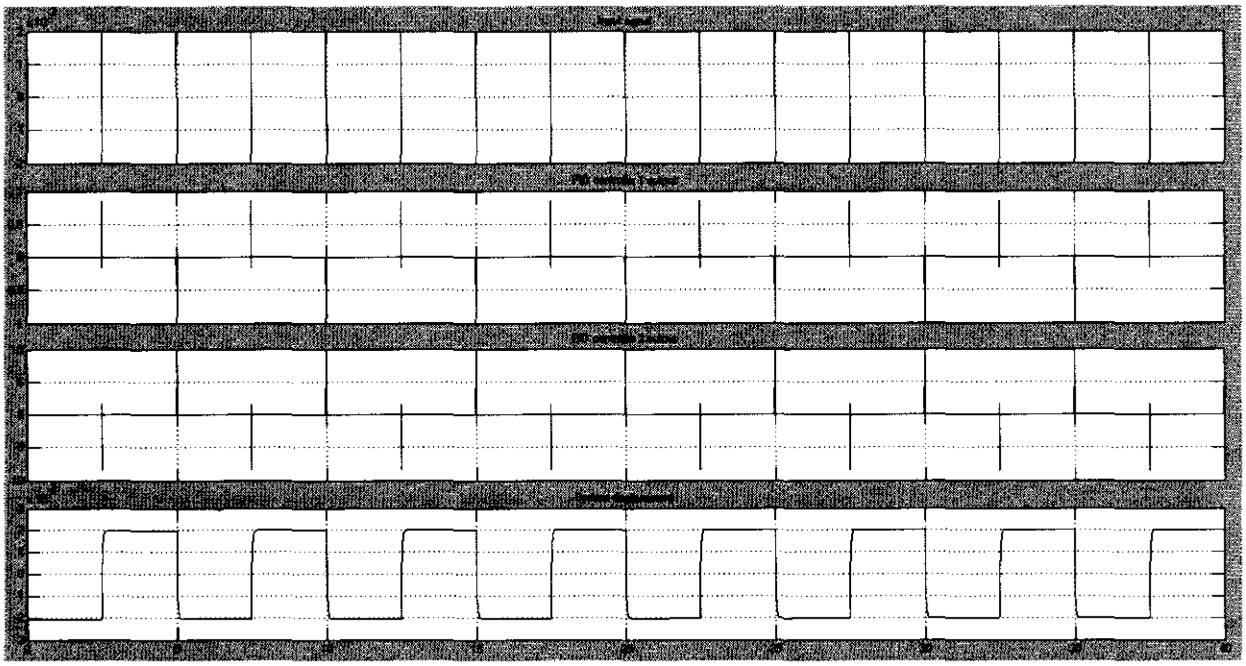

Figure 5.13: Output of the complete Simulink® model with discrete PID controllers

The best values obtained from the simulation for the first controller is $K_{P1} = 10$, $K_{I1} = 1$, $K_{D1} = 0.3$ and for the second controller is $K_{P2} = 100$, $K_{I2} = 10$ and $K_{D2} = 3$. From figure 5.13 it is clear that the model will suspend and follow the square wave input signal. The firing of the PID controllers can be seen each time the input signal changes direction.

5.4. ANALOG PID CONTROLLER DESIGN

In this section the analog design of the PID controller from the simulation constants will be done. Only one standard controller will be designed with variable resistors. The gain of the different stages can then be changed to get the best result.

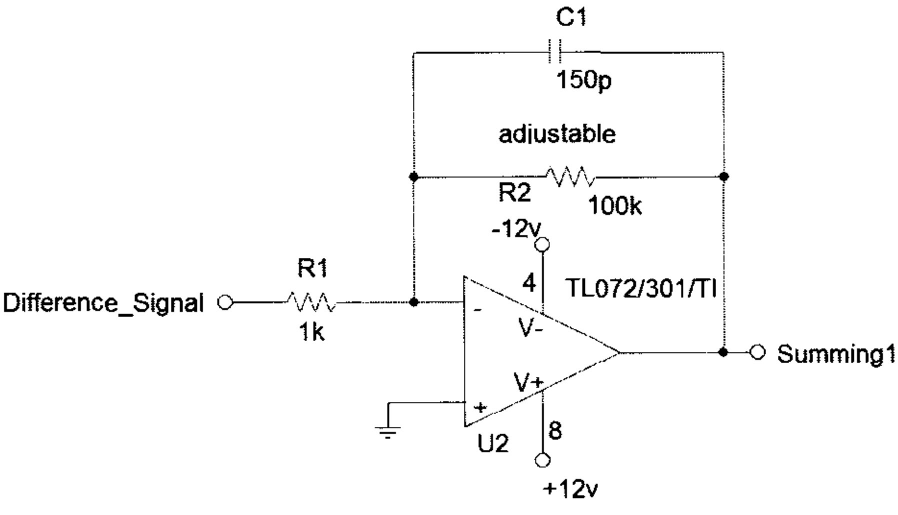

Figure 5.14: Proportional gain (K_P)

Figure 5.14 provides the proportional gain K_P. The value of the resistors was calculated as follow:

$$Gain(K_P) = \frac{\text{Summing1}}{\text{Difference\_Signal}} = \frac{\text{R2}}{\text{R1}} = \frac{100\times10^3}{1\times10^3} = 100$$

It was decided to place a low pass filter of ≈10 kHz at each stage. The capacitor value was calculated as follow:

$$f = \frac{1}{2\cdot\pi\cdot\text{R2}\cdot\text{C1}} = \frac{1}{2\cdot\pi\cdot100\times10^3\cdot150\times10^{-12}} = 10.610\,\text{kHz}$$

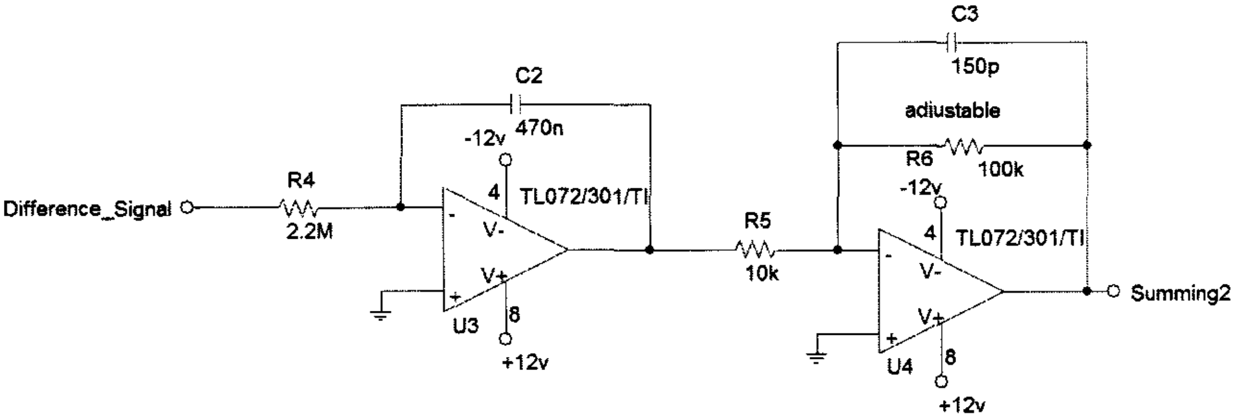

Figure 5.15: Integral gain (K_I)

Figure 5.15 shows the integral gain (K_I) of the PID controller. The first op-amp serves as an integrator with $T = 1/\text{R4}\cdot\text{C2} = 1/2.2\times10^6\cdot470\times10^{-9} = 0.98 \approx 1$ and the second is an inverting amplifier with gain of 10.

The resistor values are calculated as follows:

$$Gain(K_I) = \frac{\text{Summing2}}{\text{Difference\_Signal}} = \frac{\text{R6}}{\text{R5}} = \frac{100\times10^3}{10\times10^3} = 10$$

The value of the capacitor (C3) for the low pass filter was calculated with:

$$f = \frac{1}{2\cdot\pi\cdot\text{R6}\cdot\text{C3}} = \frac{1}{2\cdot\pi\cdot100\times10^3\cdot150\times10^{-12}} = 10.610\,\text{kHz}$$

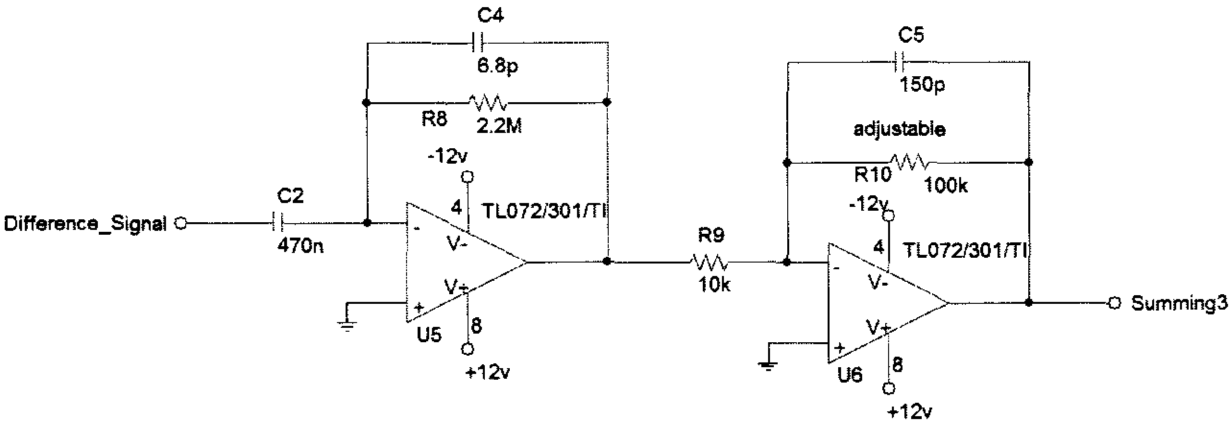

Figure 5.16: Derivative gain (K_D)

The first operational amplifier in figure 5.16 serves as a differentiator with $T = 1/\mathrm{R8}\cdot\mathrm{C2} = 1/2.2\times10^{6}\cdot 470\times10^{-9} = 0.98 \approx 1$ and the second is the gain of the derivative.

The resistor values are calculated as follow:

$$Gain(K_D) = \frac{\text{Summing3}}{\text{Difference\_Signal}} = \frac{\mathrm{R10}}{\mathrm{R9}} = \frac{100\times10^{3}}{10\times10^{3}} = 10$$

The calculation of the capacitor C5 was done as follow:

$$f = \frac{1}{2\cdot\pi\cdot\mathrm{R10}\cdot\mathrm{C5}} = \frac{1}{2\cdot\pi\cdot100\times10^{3}\cdot150\times10^{-12}} = 10.610\,\mathrm{kHz}$$

A capacitor C4 was added to the design of the differentiator. This capacitor makes the differentiator react as if it is an active differentiator. The cut-off frequency was calculated as follow:

$$f = \frac{1}{2\cdot\pi\cdot\mathrm{R8}\cdot\mathrm{C4}} = \frac{1}{2\cdot\pi\cdot2.2\times10^{6}\cdot6.8\times10^{-12}} = 10.610\,\mathrm{kHz}$$

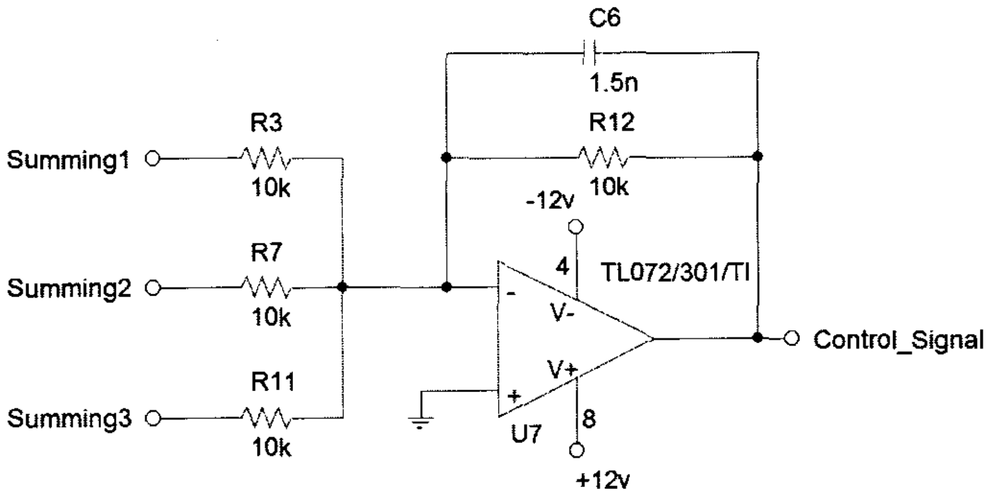

Figure 5.17: Summing of gains

The final stage of the PID controller design is the summing of the gains. The different resistor values are calculated as follow:

$$\begin{aligned}
\text{Control_Signal} &= -\left[\frac{\text{R12}}{\text{R3}}\text{Summing1} + \frac{\text{R12}}{\text{R7}}\text{Summing2} + \frac{\text{R12}}{\text{R11}}\text{Summing3}\right] \\
&= -\left[\frac{10\times10^3}{10\times10^3}\text{Summing1} + \frac{10\times10^3}{10\times10^3}\text{Summing2} + \frac{10\times10^3}{10\times10^3}\text{Summing3}\right] \\
&= -[\text{Summing1} + \text{Summing2} + \text{Summing3}]
\end{aligned}$$

The calculation of the capacitor C6 for the low pass filtering was done as follow:

$$f = \frac{1}{2\cdot\pi\cdot\text{R12}\cdot\text{C6}} = \frac{1}{2\cdot\pi\cdot10\times10^3\cdot1.5\times10^{-9}} = 10.610\,\text{kHz}$$

The complete circuit diagram can be seen in appendix B.

5.5. ANALOG LEAD CONTROLLER DESIGN

The lead compensator has the transfer function

$$G_c(s) = \frac{K(s+z)}{(s+p)}$$

The uncompensated system transfer function will be used to obtain the constants of the lead compensator. For this purpose the transfer function of the plant *G(s)* must be obtained. Figure 5.18 shows the block diagram of the compensation network.

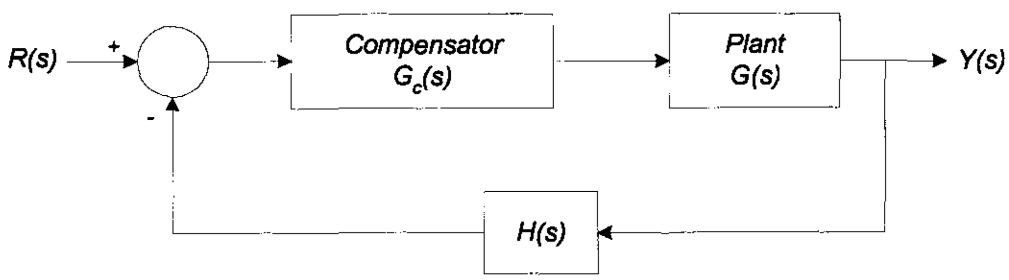

Figure 5.18: Compensation network

The plant transfer function *G(s)* is obtained by analysing the transfer function of the magnetic bearing block in figure 5.5.

$$[IK_aK_i + K_sX - mg]\left[\frac{1}{m}\right]\left[\frac{1}{s}\right]\left[\frac{1}{s}\right] = X$$

$$\Rightarrow I\left[\frac{K_aK_i}{ms^2}\right] + \frac{K_sX}{ms^2} - \frac{mg}{ms^2} = X$$

$$\Rightarrow I\left[\frac{K_aK_i}{ms^2}\right] = X\left[1 - \frac{K_s}{ms^2}\right] + \frac{mg}{ms^2}$$

$$\therefore \frac{X}{I} = \frac{\left[\frac{K_aK_i}{ms^2}\right]}{\left[1 - \frac{K_s}{ms^2}\right]} - \frac{mg}{ms^2 I\left[1 - \frac{K_s}{ms^2}\right]}$$

$$G(s) = \left.\frac{X}{I}\right|_{mg=0} = \frac{\left[\frac{K_aK_i}{ms^2}\right]}{\left[1 - \frac{K_s}{ms^2}\right]}$$

$$\therefore G(s) = \frac{500}{s^2 - 0.05}$$

A gain K must now be chosen to satisfy the steady-state requirements. This gain was chosen to be $K = 10$. The Bode diagram of $KG(s)$ can now be drawn, where the amount of necessary phase lead can be determined. Figure 5.19 provides the Bode diagram of $KG(s)$.

The phase margin (θ_m) can be calculated by using the margin command in Matlab®. The value of θ_m was calculated to be 1.2217 rad/sec. The value of α can be obtained by using the phase margin and the equation

$$\sin\theta_m = \frac{(\alpha - 1)}{(\alpha + 1)}$$

The value of α was calculated to be 32.1634. The total magnitude gain of the system is 20 log α dB, therefore we expect a gain of 10 log α dB at ω_m. The frequency ω_m can be obtained by plotting -10 log α.

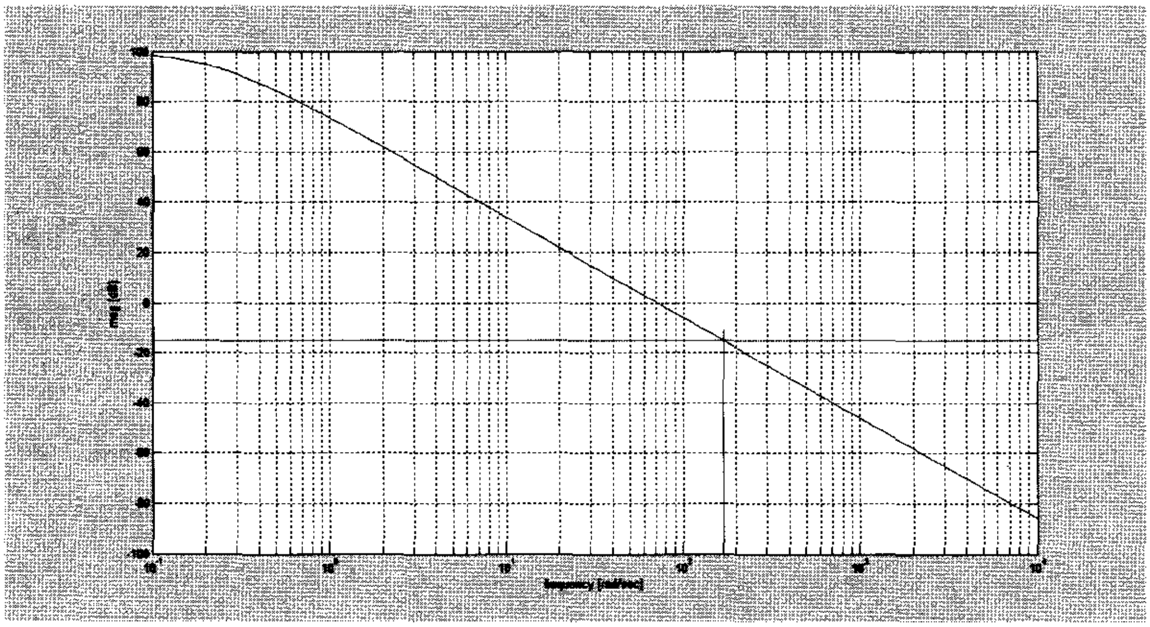

Figure 5.19: Bode diagram of $KG(s)$

The plot of -10log α provides a straight line of -15.07 dB. This straight line can be seen in figure 5.19. The crossover frequency (ω_m) is then calculated as 170 rad/sec. The complete Matlab® source code can be found in appendix H.

With α = 32.1634 and ω_m = 170 rad/sec the constants p and z can now be calculated.

$$\begin{aligned} p &= \omega_m \sqrt{\alpha} \\ &= 170\sqrt{32.1634} \\ &= 964.1 \end{aligned} \qquad \text{and} \qquad \begin{aligned} z &= \frac{p}{\alpha} \\ &= \frac{964.1}{32.1634} \\ &= 29.98 \end{aligned}$$

The lead compensator then looks as follow:

$$\begin{aligned} G(s) &= \frac{K(s+z)}{(s+p)} \\ &= \frac{100(s+29.98)}{(s+964.1)} \end{aligned}$$

A gain of 100 was chosen, since it is desired to have a steady-state error for a ramp input equal to $\approx$1% of the magnitude of the ramp. ($K_V = \frac{A}{e_{ss}} = \frac{A}{0.01A} = 100$)

The analog design of the resistor and capacitor values can now be obtained from the following equations:

$$\begin{aligned} \alpha &= \frac{\mathrm{R1}+\mathrm{R2}}{\mathrm{R2}} \\ \frac{\mathrm{R2}}{\mathrm{R1}+\mathrm{R2}} &= \frac{1}{32.1634} \end{aligned} \qquad \begin{aligned} \tau &= \frac{1}{\omega_m \sqrt{\alpha}} \\ &= \frac{1}{170\sqrt{32.1634}} \\ &= 1.037 \times 10^{-3}\ \mathrm{s} \end{aligned}$$

Choose C = 200 nF

$$\begin{aligned} \tau &= \frac{\mathrm{R1}\cdot\mathrm{R2}}{\mathrm{R1}+\mathrm{R2}}\mathrm{C} \\ 1.037 \times 10^{-3} &= \frac{\mathrm{R1}}{32.1634}\mathrm{C} \\ \mathrm{R1} &= 166.77\,\mathrm{k\Omega} \end{aligned}$$

and therefore R2 = 5.35 kΩ

The complete circuit diagram for the lead controller can be found in figure 5.20.

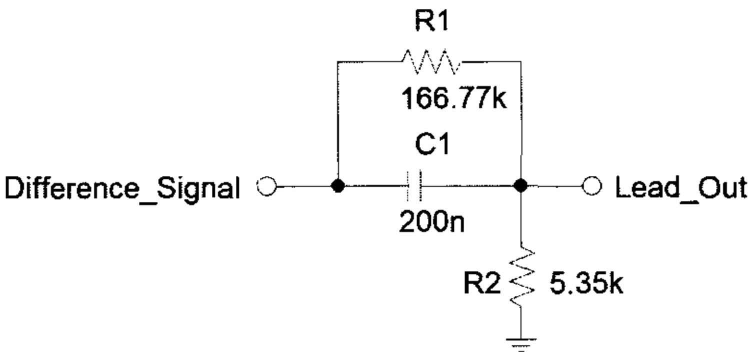

Figure 5.20: Lead controller circuit diagram

The gain of the lead controller is:

$$Gain = \frac{\text{R2}}{\text{R1}+\text{R2}} = \frac{5.35\times10^3}{166.77\times10^3 + 5.35\times10^3} = 0.031$$

Figure 5.21 provides the circuit diagram for the proportional gain (K). It was decided to use a variable resistor in the design of the gain (K). The gain can then be changed to obtain the best result.

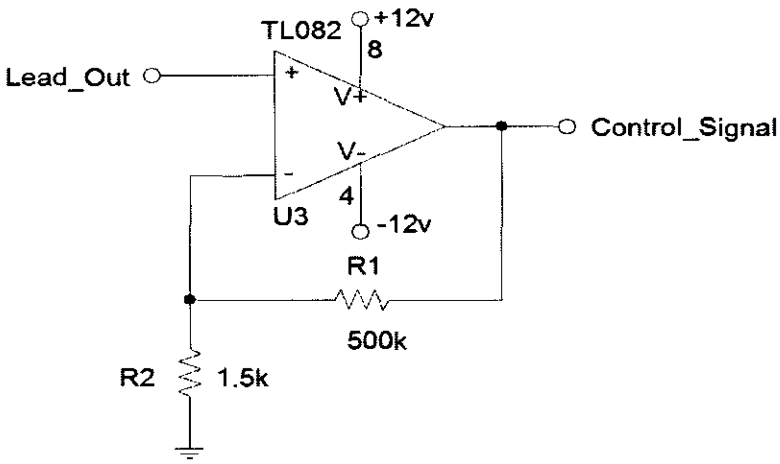

Figure 5.21: Proportional gain circuit diagram

The resistor values are calculated as follow:

$$Gain = \frac{\text{R1}}{\text{R2}} = \frac{500\times10^3}{1.5\times10^3} = 333.33 \text{ (With R1 being the variable resistor)}$$

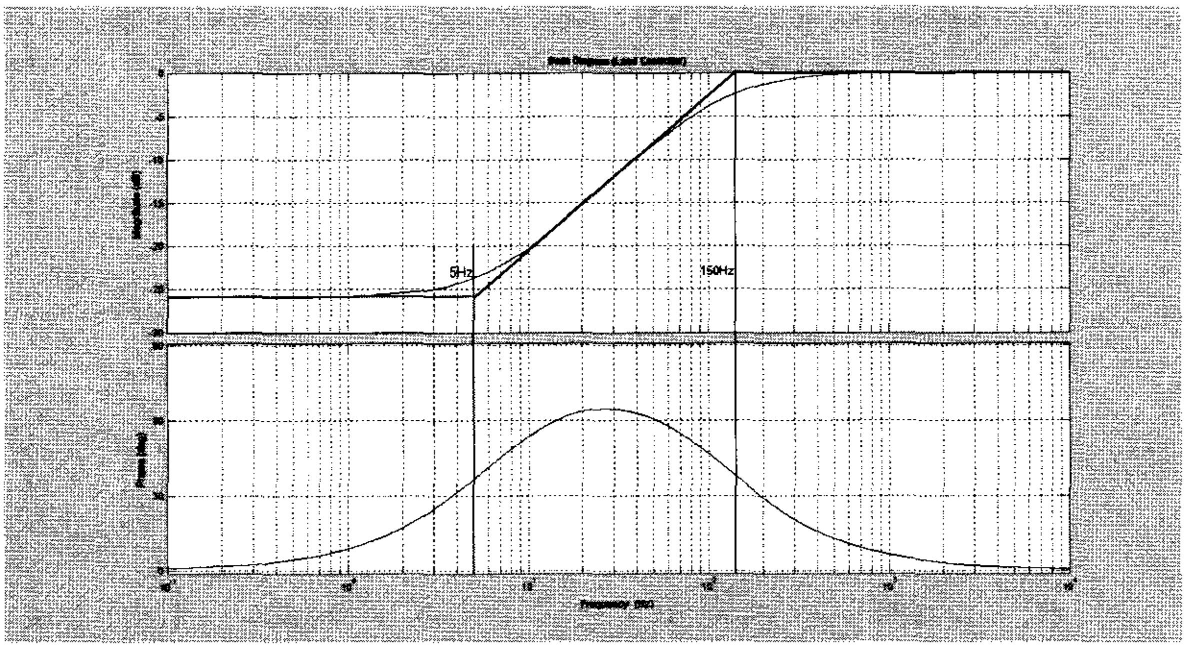

Figure 5.22: Lead controller Bode diagram

The lower breakpoint frequency for the lead controller is:

$$f_1 = \frac{1}{2 \cdot \pi \cdot \mathrm{R1} \cdot \mathrm{C}} = \frac{1}{2 \cdot \pi \cdot 166.77 \times 10^3 \cdot 200 \times 10^{-9}} = 4.7\,\mathrm{Hz}$$

The upper breakpoint frequency for the lead controller is:

$$f_2 = \frac{1}{2 \cdot \pi \cdot (\mathrm{R1} \parallel \mathrm{R2})\mathrm{C}} = \frac{1}{2 \cdot \pi \cdot (166.77 \times 10^3 \parallel 5.35 \times 10^3) \cdot 200 \times 10^{-9}} = 153.5\,\mathrm{Hz}$$

5.6. SIMULATION DESIGN OF THE LEAD CONTROLLERS

In this section the analog lead controller will be converted into a discrete lead controller. The simulation design of the lead controllers will be done by using the complete Simulink® model with discrete PID controllers (figure 5.12) as basis for the simulation.

The analog and discrete transfer function for the lead compensator has the form:

$$G_c(s) = \frac{K_a(s - s_0)}{(s - s_p)} \rightarrow G_c(z) = \frac{K_d(s - z_0)}{(s - z_p)}$$

The equation $G_c(s)$ = 100(s+20)/(s+929.1) was obtained from the analog design of the lead controller. The values of z_0 and z_p can be obtained from (1) and (2). A sampling time of $T = 0.0001$ s (f = 10 kHz) was used.

$$z_0 = e^{S_0 T} = 0.998 \tag{1}$$

$$z_p = e^{S_p T} = 0.911 \tag{2}$$

The constant K_d can be obtained by using (3).

$$\begin{aligned} \lim_{s \to 0} \frac{K_a(s - s_0)}{(s - s_p)} &= \lim_{z \to 1} \frac{K_d(z - z_0)}{(z - z_p)} \\ \therefore \frac{K_a s_0}{s_p} &= K_d\left(\frac{1 - z_0}{1 - z_p}\right) \end{aligned} \tag{3}$$

The discrete transfer function of the lead controller then looks as follow:

$$G_c(z) = \frac{95.69(z - 0.998)}{z - 0.911}$$

The discrete PID controller from figure 5.12 was replaced with the discrete lead transfer function to obtain the best values for the constant K. $K = 95.69$ was found to be the best value for the top electromagnet and $K = 287.07$ for the bottom one. These blocks can be seen in figure 5.23.

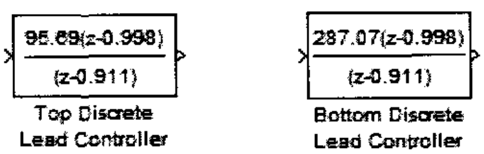

Figure 5.23: The top and bottom discrete lead controllers

Figure 5.24 provides the simulation output of the discrete lead controllers. From this figure it can be seen that the position output follows the input signal. The firing of lead controller 1 (for the top electromagnet) and lead controller 2 (bottom electromagnet) can also be seen in this figure.

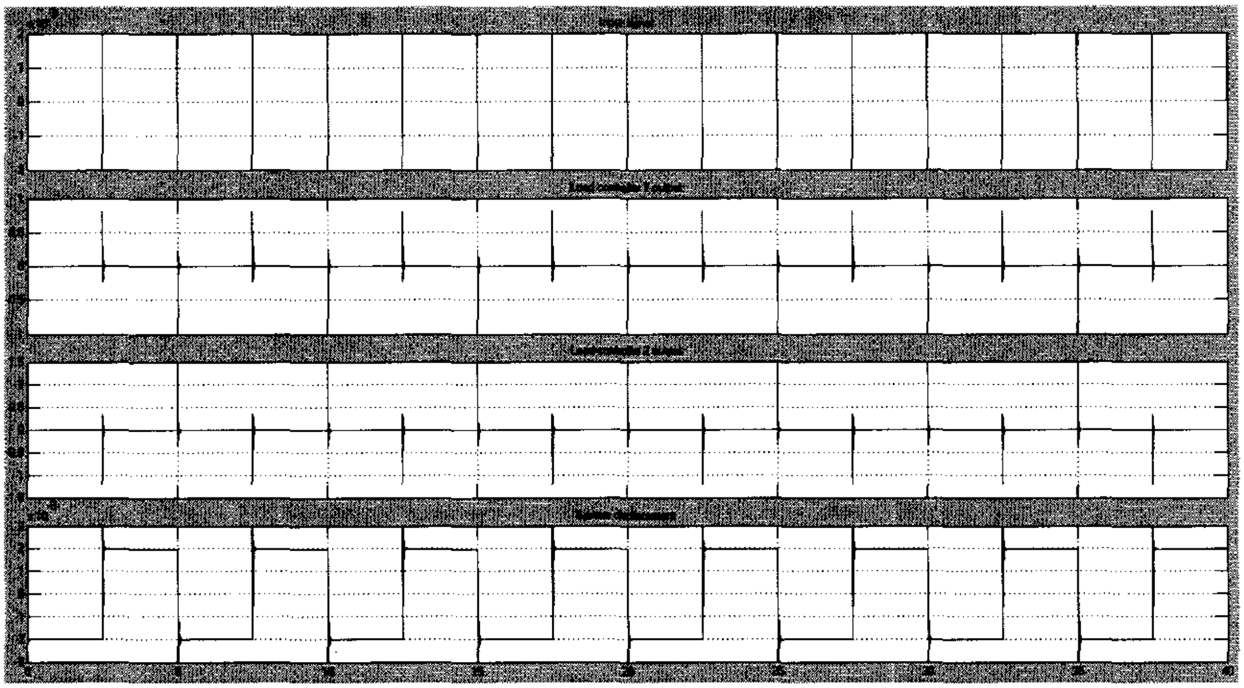

Figure 5.24: Output of the Simulink® model with discrete lead controllers

5.7. FINALISING THE ANALOG DESIGN

The final steps of the analog design are the design of the difference circuit and the actuating unit. The difference circuit centres the sensor signal around the zero point. The output of the difference circuit will then change form -10 to +10 according to the position of the steel disc.

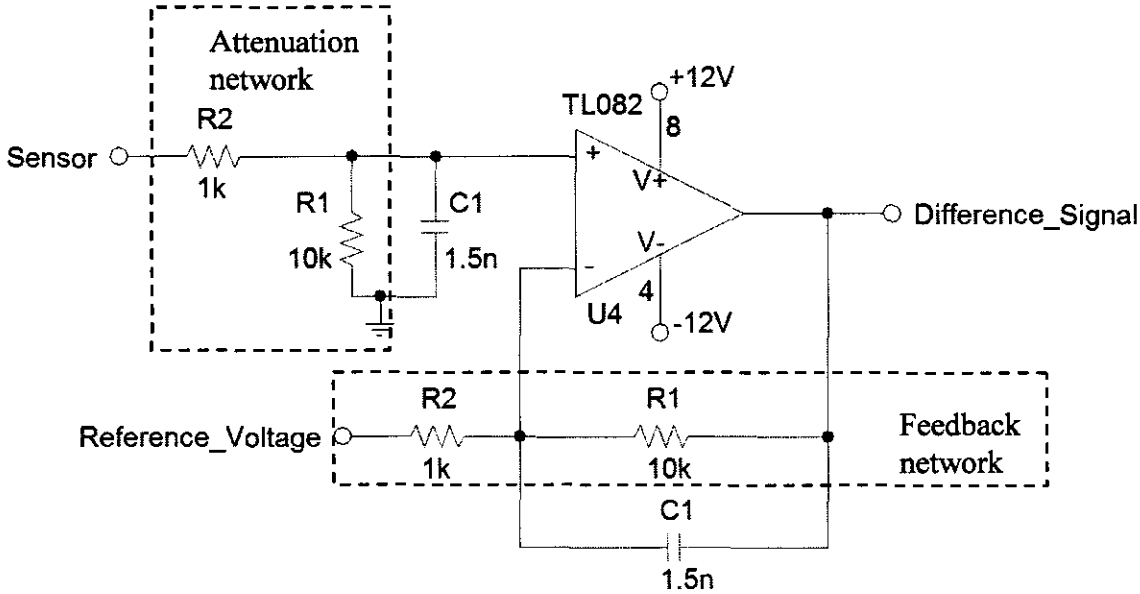

Figure 5.25: Difference circuit diagram

Figure 5.25 provides the difference circuit diagram with the necessary component values. The design and calculation of the resistor and capacitor values are done as follow:

The voltage divider attenuates V_{sensor} so that $V_+ = mV_{Sensor}$, where

$$m = \frac{\mathrm{R1}}{\mathrm{R1}+\mathrm{R2}}$$

The difference output signal is calculated as follow

$$\begin{aligned} V_{Difference\_Signal} &= \frac{\mathrm{R1}+\mathrm{R2}}{\mathrm{R2}} mV_{Sensor} - \frac{\mathrm{R1}}{\mathrm{R2}} V_{Reference\_Voltage} \\ &= \frac{\mathrm{R1}+\mathrm{R2}}{\mathrm{R2}} \frac{\mathrm{R1}}{\mathrm{R1}+\mathrm{R2}} V_{Sensor} - \frac{\mathrm{R1}}{\mathrm{R2}} V_{Reference\_Voltage} \\ &= \frac{\mathrm{R1}}{\mathrm{R2}} (V_{Sensor} - V_{Reference\_Voltage}) \end{aligned}$$

With R1 = 10 kΩ and R2 = 1 kΩ the total gain is

$$Gain = \frac{\mathrm{R1}}{\mathrm{R2}} = \frac{10\times10^3}{1\times10^3} = 10$$

The capacitor/resistor pair serves as a low pass filter with frequency:

$$f = \frac{1}{2\cdot\pi\cdot\mathrm{R1}\cdot\mathrm{C1}} = \frac{1}{2\cdot\pi\cdot10\times10^3\cdot1.5\times10^{-9}} = 10.61 \text{ kHz}$$

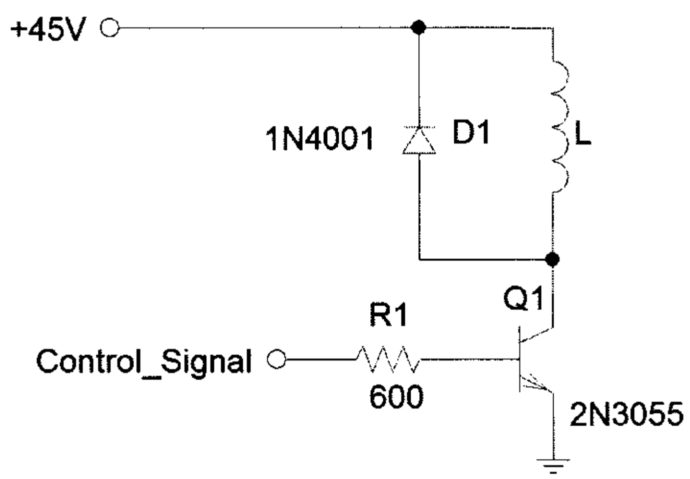

Figure 5.26: Actuating unit circuit diagram

The circuit in figure 5.26 controls the current in the electromagnetic levitation coil L. The 2N3055 transistor has a beta of more than 50, which is sufficient to drive loads of up to 2 amperes without any additional circuitry.

The base resistor R1 provides current protection. It limits the output current demand on the op-amp. The op-amp works at 12 V and the base terminal is 0.7 V. Therefore the maximum base current will be $I_b = (12 - 0.7)/600 = 18.83$ mA.

The actual maximum value of the base resistor that can be used depends on the maximum collector current required and the gain (beta) of the transistor.

5.8. dSPACE® PID AND LEAD CONTROLLER DESIGNS

In this section the PID and lead controller designs for the dSpace® controller will be done. The constants obtained from the simulation of the discrete PID controller will be used to design the real-time model.

It was decided to choose the sample time (Ts) of the real time interface (RTI) at least 7 times the bandwidth of the sensor. The bandwidth of the sensor is ≈1 kHz, therefore $fs_{real\ time} > 7$ kHz. The sample time was chosen at $Ts_{real\ time} = 0.0001$ ($fs_{real\ time} = 10$ kHz).

The real-time Simulink® model can be seen in figure 5.27. In this figure the sensor signal enters the dSpace® controller at ADC port 5. Upper and lower limits of -10 and +10 are then placed on the signal.

The signal is then passed onto the sensor calibration, where the gain and reference position of the sensor signal can be fine tuned. The signal "sensor2" is then passed onto the position reference of the model. By changing the value of this constant, the steel disc can be moved up and down.

This signal is then passed onto the different PID controller stages. The constants: "Constant1" and "Constant2" change the working position of the controllers. By changing these constants, the amount of work done by the electromagnets can be changed.

A lower limit of zero has been placed on "Control1" and "Control2". This will prevent the output from going negative. The controller 1 signal is then written out to actuator 1 via port 1 of the DAC and the controller 2 signal is written out to actuator 2 via port 3 of the DAC.

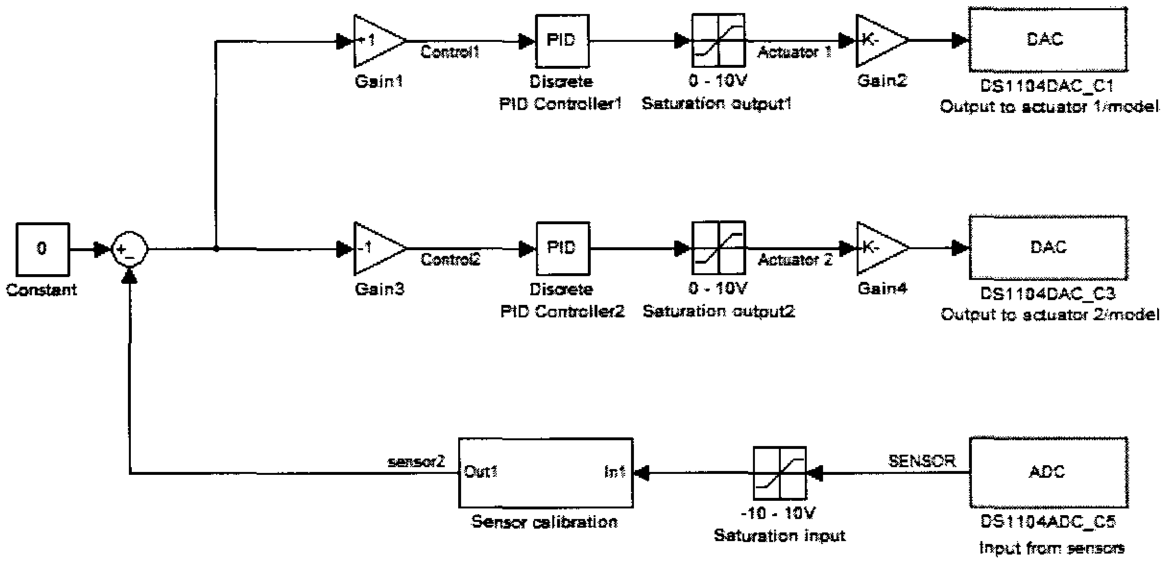

Figure 5.27: Real time PID controller Simulink® model

For the real time lead controller Simulink® model the discrete PID controller blocks of the above figure are replaced with the discrete lead controller blocks shown in figure 5.23.

5.9. STIFFNESS OF THE MODEL

In this section the open loop stiffness and current gain of the model will be evaluated. The stiffness of a bearing characterizes its spring-like behaviour, i.e. the ratio of the supported load with respect to the resulting displacement of that load.

The term is based on the understanding that a bearing is a mechanical element. In classical bearings the stiffness stems for example from the elasticity of the oil film or the deformation of balls and inner ring of a ball bearing.

In an AMB the force is generated by a control current, which can be adjusted to the needs and opens a novel way of shaping the stiffness and even the overall dynamic behaviour, and thus the term "stiffness" may not be the best way to describe the performance of an AMB, but is still used for comparison reasons with classical bearings.

One way of obtaining a high *static stiffness* is by applying PID-control. In that way, the current i and implicitly the force as well, is shaped depending on the displacement x of the rotor within the air gap as [19].

$$i = Px + I\int x\mathrm{d}t + Ddx/dt$$

The integral part of the PID control brings the position x to the same value before and after the load step, and thus the rotor shows a behaviour that cannot be obtained with classical bearings (figure 5.28). The time constant for that compensation cannot be made arbitrarily small without increasing the stiffness constant P and the damping constant D.

Looking at the bearing only, its static stiffness has become infinite as under stationary load there is no displacement, as long as the maximum carrying force is respected. For comparison, the behaviour without compensating integrator is shown, as it would correspond to a classical bearing with spring/damper characteristics as well.

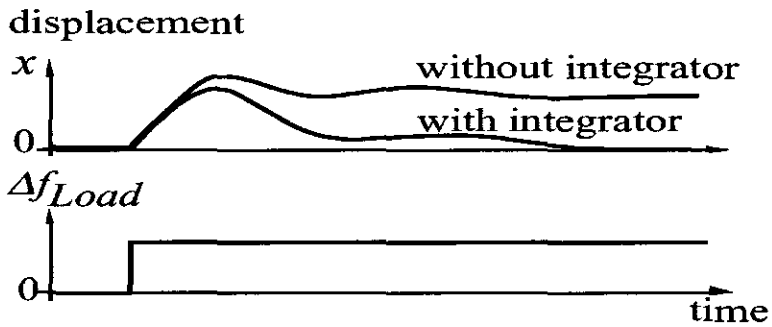

Figure 5.28: Step response of rotor position to a change in load force with PD and PID control. [19]

From figure 5.9 the open loop stiffness of the system can be calculated. The working distance of the disc is chosen at 3 mm. Therefore the open loop stiffness k_s of the system is:

$$\begin{aligned} k_s &= \frac{F}{x} \\ &= \frac{20.18418}{0.003} \\ &= 6728.06\,\mathrm{Nm}^{-1} \end{aligned}$$

where F is the attraction force of the electromagnet, x is the distance of the air gap and k_s is the open loop stiffness of the model.

The natural frequency of k_s can be obtained by using the open loop stiffness k_s and the mass of the system.

$$\omega_{n(ks)} = \sqrt{\frac{k_s}{m}}$$
$$= \sqrt{\frac{6728.06}{2}}$$
$$= 58\,\mathrm{rad\,s^{-1}}$$

where $\omega_{n(ks)}$ is the natural frequency of k_s, k_s is the open loop stiffness and m is the mass of the disc.

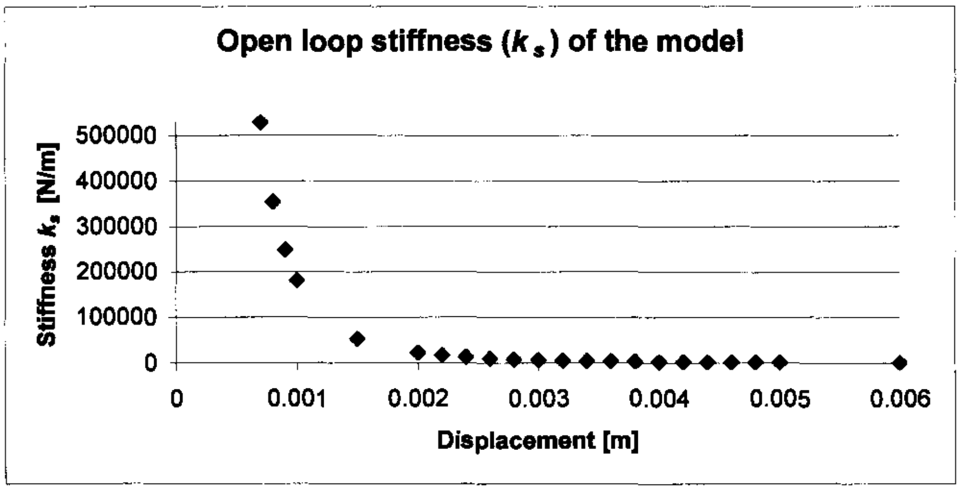

Figure 5.29: Stiffness k_s of the model with increasing displacement

Figure 5.29 provides the open loop stiffness k_s of the model with increasing displacement. The open loop stiffness k_s of the system increases dramatically when the distance is changed from 3 mm to 1 mm and decreases dramatically when the distance is increased.

The working current of the disc at 3 mm is 1 A. The gain k_i can be calculated as follow:

$$k_i = \frac{F}{i}$$
$$= \frac{80.764}{1}$$
$$= 80.764\,\mathrm{NA^{-1}}$$

where k_i is the gain, F is the attraction force of the electromagnet and i is the current.

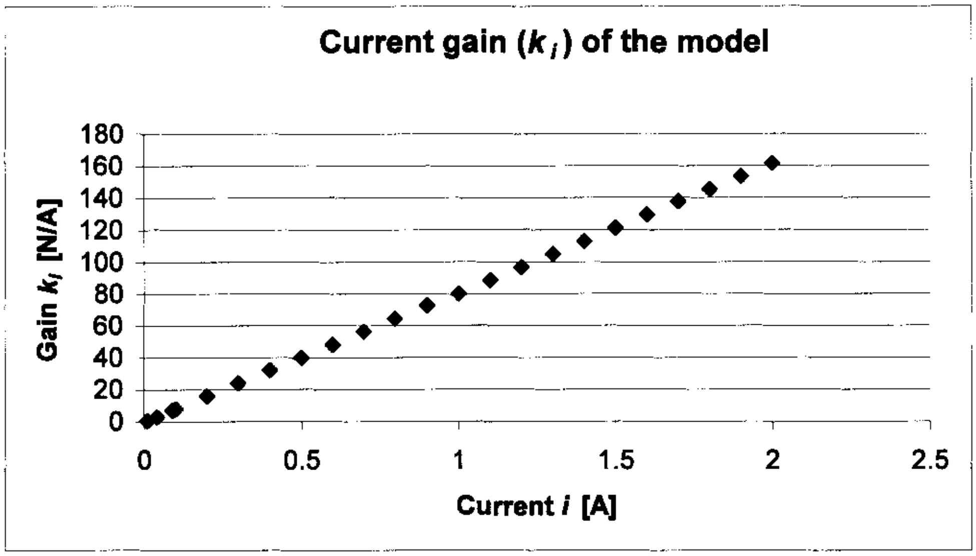

Figure 5.30: Current gain k_i of the model with increasing current

Figure 5.30 provides the current gain k_i of the model with increasing current. The gain k_i of the system increases linearly with an increase in the current.

5.10. CONCLUSIONS

In this chapter the PID and lead controllers were designed and implemented successfully. The analog model was integrated and the complete system of figure B.2 and figure B.3 was built and tested. Both analog models provided stable suspension of the model. Appendix G provides oscilloscope printouts of the controllers.

The dSpace® real-time Simulink® model was downloaded onto the DSP controller and the result obtained can be found in chapter 6. The Simulink® model provides useful information about the constants of the real time model and these constants can be used to suspend the model in real-time.

CHAPTER 6

RESULTS OBTAINED WITH DSPACE® AND SYSTEM EVALUATION

6.1. INTRODUCTION

This chapter focuses on the results obtained with the dSpace® DS1104 controller and the complete system evaluation. The dSpace® software Controldesk was used to obtain results and load and disturbance tests were performed for system evaluation.

6.2. DSPACE® CONTROLDESK INTERFACE

Controldesk is a software package of dSpace® where the user can perform experiments and automate test operations in a platform environment. Controldesk provides graphs and buttons for easy use, but the source code must still be written for each device used. When working in the real time interface (RTI) of Controldesk care must be taken with defining the correct sampling time, solver type and block reduction for each device otherwise the processor will stop responding.

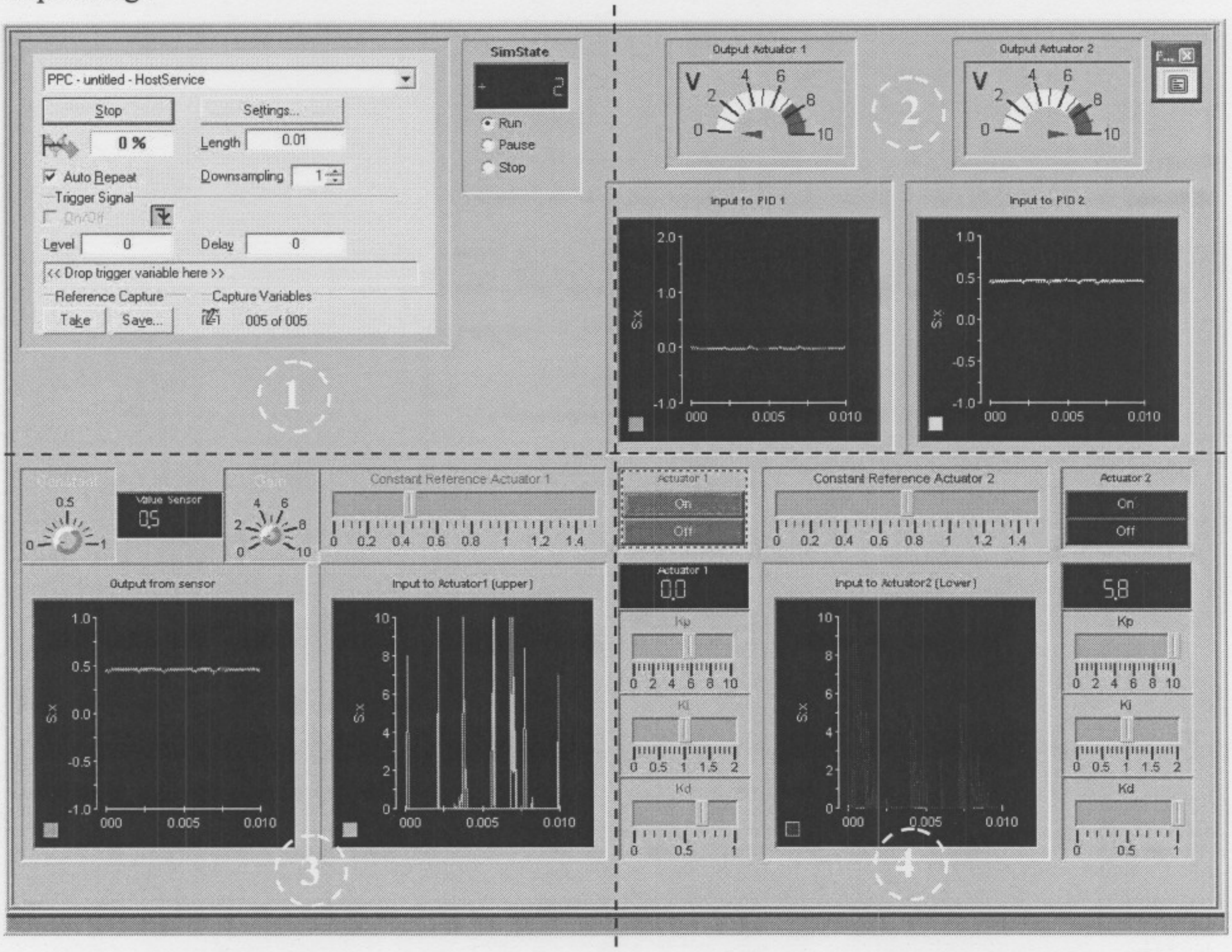

Figure 6.1: Layout of the Controldesk interface[2]

[2] This figure is best viewed in full colour on the CD. File: dSpace.jpg, available on request.

Figure 6.1 provides the layout of the Controldesk interface. This figure is divided into 4 parts. Part 1 provides the capture variables and simulation state. The capture variables window makes it possible to display sampling of input and output variables in Controldesk. It was chosen to make this window visible, with a sampling length of 0.01 s. For monitoring the model in real time, the delay levels were chosen as zero.

The simulation state (SimState) window makes it possible to stop, run and pause the real time controller at any time. This is quite useful in case of an emergency. Care must be taken when working with SimState, since it writes real time code (RTC) to the processor. This RTC stops the processor and clears the memory. The run button must be pressed, which will reload the RTC to the processor, before analysis can continue.

The second part provides the voltage output of actuator 1 and actuator 2 and shows the input signals to PID controller 1 and PID controller 2. The voltage output of actuator 1 (for the top electromagnet) is close to zero and therefore it is releasing the disc, while the voltage output of actuator 2 (for the bottom electromagnet) is close to 10 and therefore it is attracting the disc. This is correct, since the disc has moved above the reference point and needs to be attracted downwards to stay in suspension.

The two graphs in part 2 show the input signals to PID controller 1 and PID controller 2. The signals of these graphs are labeled Control1 and Control2.

Part 3 shows graphs of the output of the sensor and input signal to actuator 1. These signals are labeled sensor2 and Actuator 1 in figure 5.27. The graph of the output of the sensor provides useful information about the position of the steel disc. The input signal to actuator 1 is the signal just before it leaves the dSpace® controller.

The gain and constant turn buttons are the gain and constant variables used for sensor calibration. Changing these values will change the reference position of the steel disc. The slide bar labeled constant reference actuator 1 provides the value of the constant parameter in figure 5.27. This value changes the reference position of actuator 1.

Part 4 shows the PID constants for actuator 1 (left side) and actuator 2 (right side). Changing the values of K_P, K_I and K_D changes the values of the PID controller in real time. There is no delay time and no need for waiting for the code to be written down to the dSpace® controller.

Two on/off push buttons has been inserted, one for actuator 1 and the other of actuator 2. These push buttons send out a zero output when the off button is pressed. These buttons are quite useful, because there is no need to wait for the RTC to be written down to the processor and all the parameters stay the same.

When using SimState the parameters are reset and reloaded onto the controller. This usually takes a while. The slide bar labeled constant reference actuator 2 and graph labeled input to actuator 1 (lower) is the same as for actuator 1.

6.3. SYSTEM ANALYSIS

In this section the system will be evaluated with square waves as inputs for the different systems. Only the discrete controller could be simulated in dSpace®. The necessary oscilloscope printouts for the analog controllers can be found in appendix G.

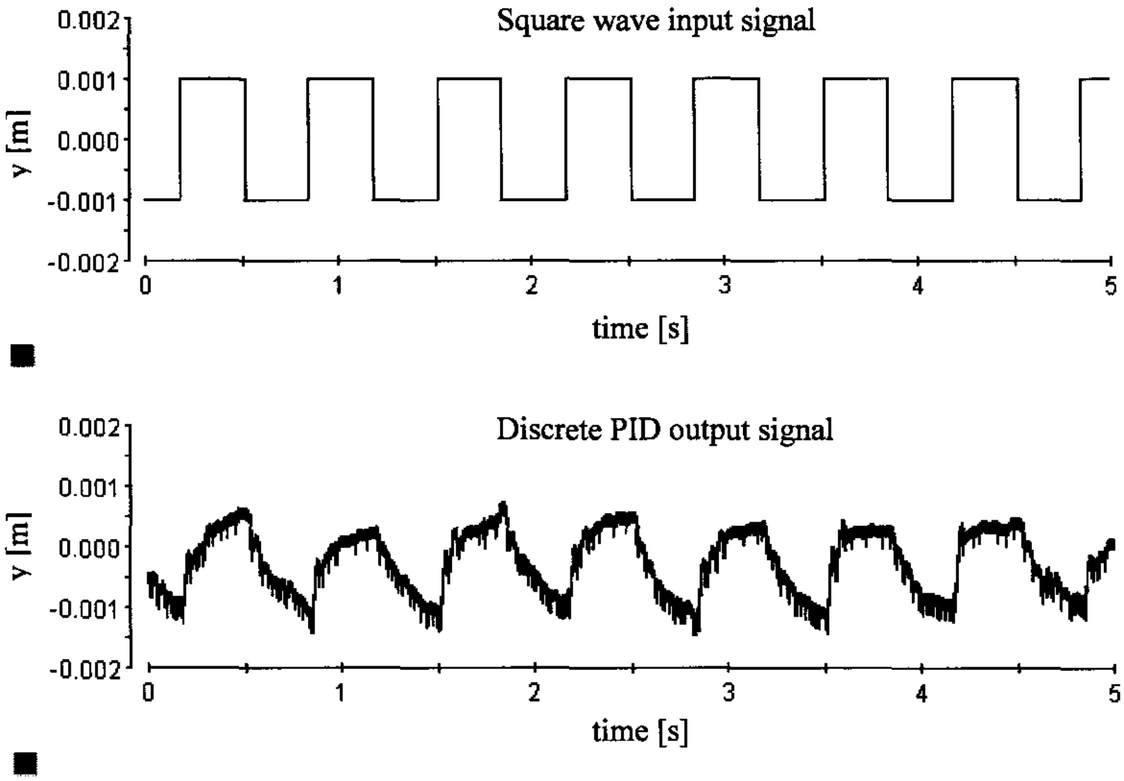

Figure 6.2: Discrete PID controller output signal with square wave as input signal

Figure 6.2 provides the output of the discrete PID controller with a square wave as input signal. A square wave was given as reference signal for the system and the output was obtained from the sensor output.

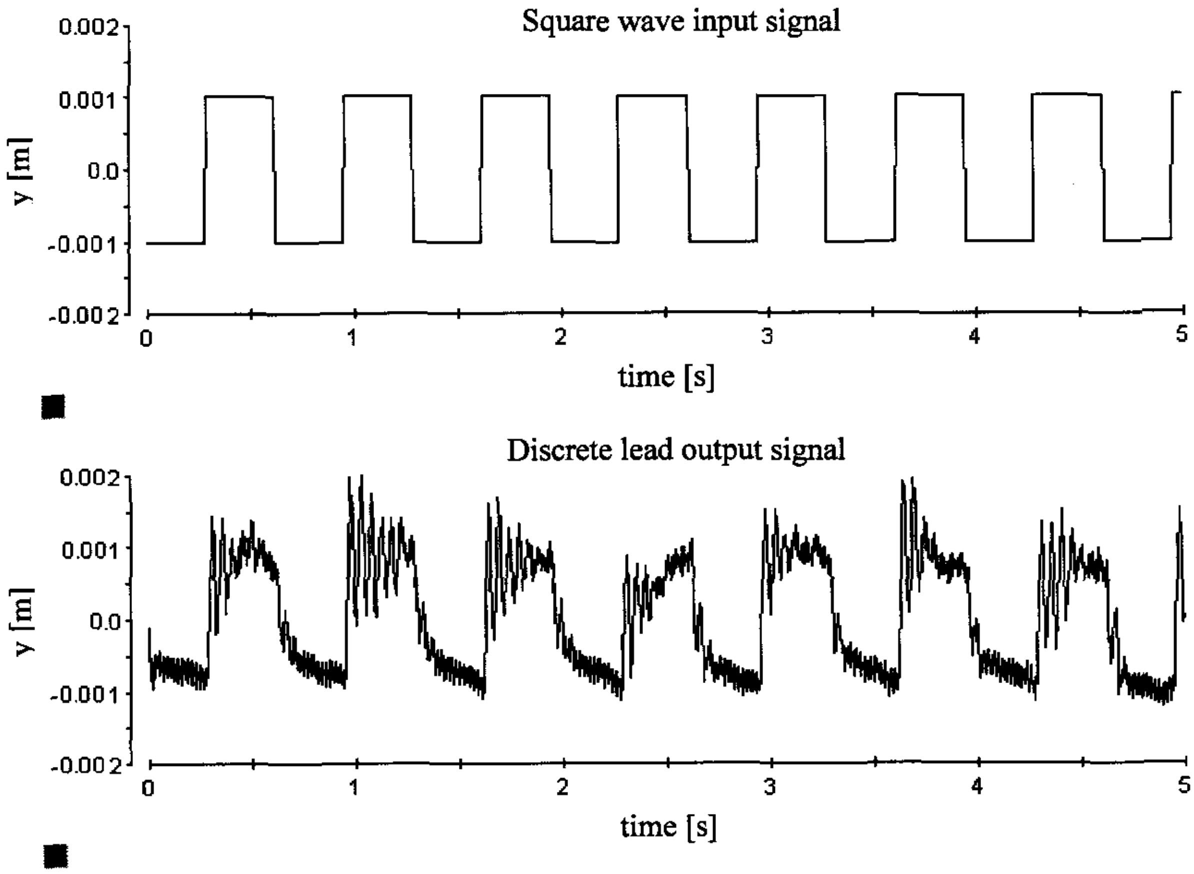

Figure 6.3: Discrete lead controller output signal with square wave as input signal

The frequency and amplitude for the discrete lead controller (figure 6.3) was chosen the same as for the discrete PID controller (figure 6.2).

In figure 6.4 the discrete PID controller output with a step response as input can be seen. From this figure it can be seen that the discrete PID controller a time-to-peak $T_p \approx 37.5$ ms and a settling time $T_s \approx 100$ ms.

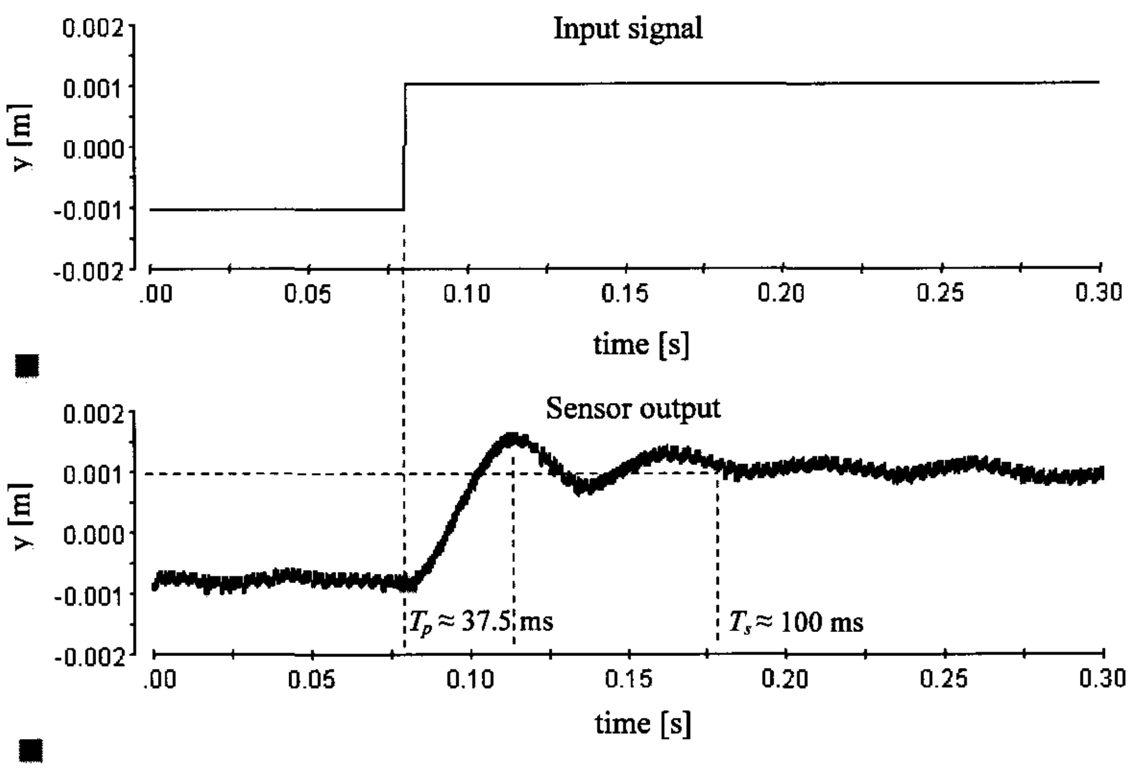

Figure 6.4: Discrete PID controller output with an input step response

The discrete lead controller output with an input step response can be seen in figure 6.5. From this figure it can be seen that the time-to-peak $T_p \approx 30$ ms and the settling time $T_s \approx 130$ ms.

Oscilloscope printouts of the analog PID controller (figure G.6) and analog lead controller (figure G.8) output signals with step response as input signal can be seen in appendix G. From these figures it can be seen that the time-to-peak and settling time for the analog PID controller are $T_p \approx 60$ ms and $T_s \approx 190$ ms respectively. For the analog lead controller $T_p \approx 40$ ms and $T_s \approx 180$ ms.

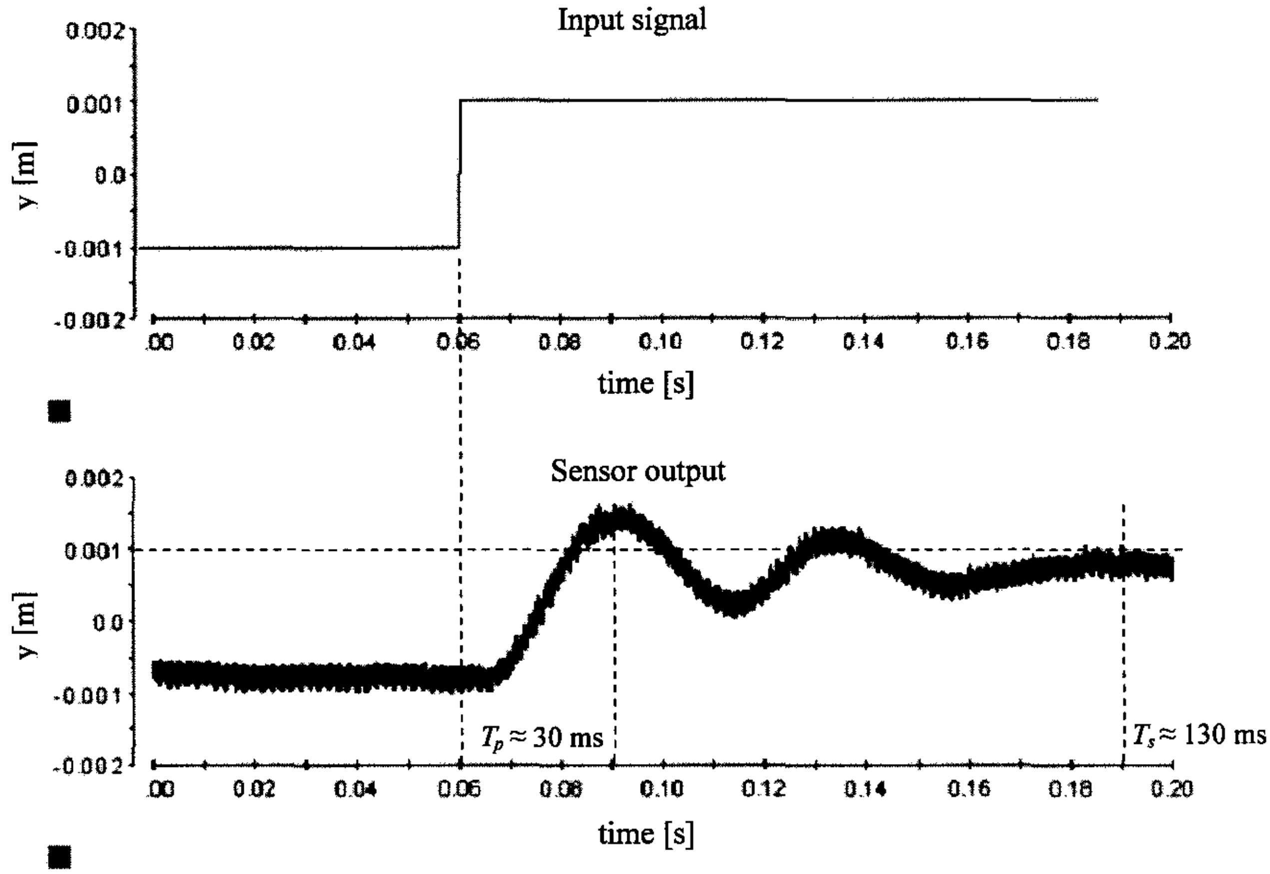

Figure 6.5: Discrete lead controller output with an input step response

6.4. LOAD TEST PERFORMED ON THE MODEL

The load test was conducted by placing different size weights on top of the steel rod of the model and to observe what impact the downward force (F_{down}) of the weights has on the amount of current necessary to keep the steel disc in suspension.

For this test the reference air gap (x) is chosen between the steel disc and the bottom electromagnet (as seen in figure 6.6). Four 1.25 kg weights and one 500 g weight were placed on the model. Table 6.1 provide the data obtained with the load test.

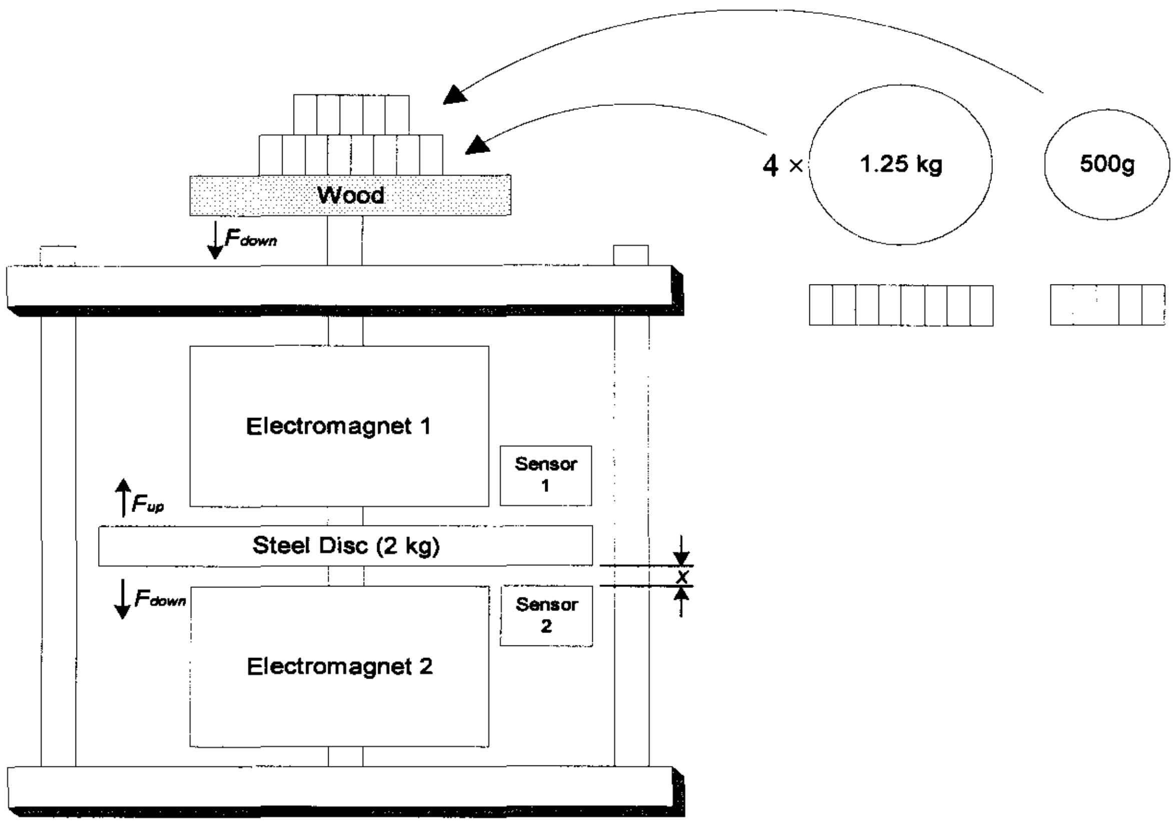

Figure 6.6: Load test performed on the axial AMB model

Figures 6.7 and 6.8 provide the analog lead and PID controller outputs under load conditions. To obtain these graphs, the analog controllers were used for controlling purposes and the position sensor output was fed into Controldesk through the A/D port of the dSpace® controller. Figure 6.7 was captured under a load condition of 3.75 kg. The steady state error $e_{ss} \approx 1.5$ mm and the air gap $x \approx 1.5$ mm.

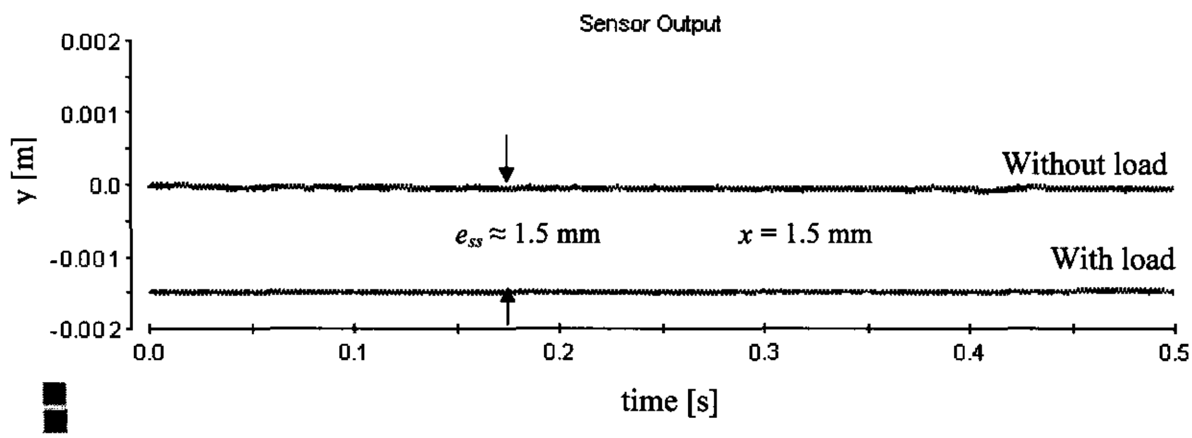

Figure 6.7: Analog lead controller output under load conditions

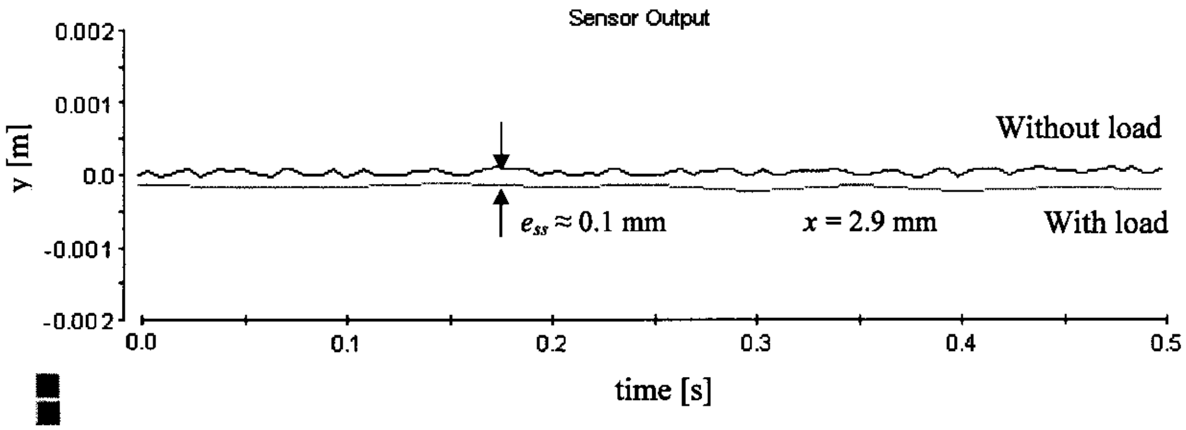

Figure 6.8: Analog PID controller output under load conditions

Figures 6.8, 6.9 and 6.10 provide graphs of the controller outputs taken under a load condition of 3.75 kg. The steady state error for the PID controllers (figures 6.8 and 6.10) is ≈0.1 mm, while the steady state error for the discrete lead controller (figure 6.9) is ≈1.4 mm.

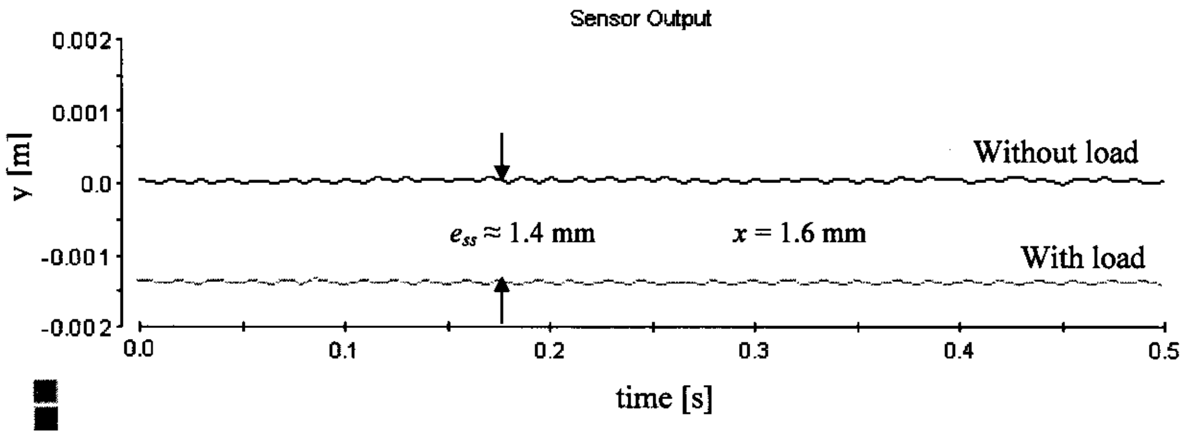

Figure 6.9: Discrete lead controller output under load conditions

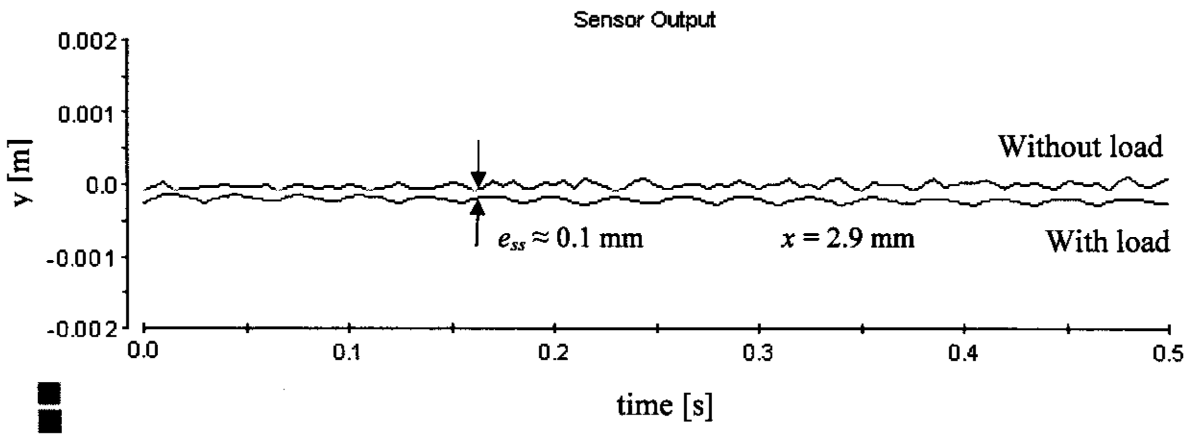

Figure 6.10: Discrete PID controller output under load conditions

Mass [kg]	Top electromagnet Current [A]				Air gap x [mm]				Steady state error e_{ss} [mm]			
	Analog Lead	Discrete Lead	Analog PID	Discrete PID	Analog Lead	Discrete Lead	Analog PID	Discrete PID	Analog Lead	Discrete Lead	Analog PID	Discrete PID
{2 kg steel disc}	0.31	0.5	0.65	0.8	3	3	3	3	0	0	0	0
0.5	0.35	0.7	0.8	1.0	3	3	3	3	0	0	0	0
1.25	0.42	0.9	0.97	1.4	2.9	2.9	3	3	0.1	0.1	0	0
2.5	0.55	1.2	1.15	1.7	2.4	2.5	3	3	0.6	0.5	0	0
3.75	0.73	1.5	1.55	2.1	1.5	1.6	2.9	2.9	1.5 (Oscillating)	1.4	0.1 (Oscillating)	0.1
5	0.98	1.7	1.79	2.5	0	0	0	0	3 (∞)	3 (∞)	3 (∞)	3 (∞)

Table 6.1: Data obtained with the load test

Table 6.1 provides the current to air gap and steady state error relation with different weights. From this table it can be seen that the steady state error stays zero for all the controllers up to an added mass of 0.5 kg. The steady state error for the PID controllers stays zero up to an added mass of 2.5 kg. When the weight increases to 5 kg the steady state error increases to 3 mm. The steel disc at this stage lies on top of the bottom electromagnet.

6.5. DISTURBANCE TEST PERFORMED ON THE MODEL

In figure 6.11 the system is evaluated by applying disturbance forces on it. A 500 g ball falling from different heights is used as disturbance on the system to see if the system can recover from the disturbance force and stably suspend the disc again.

The ball falls from a distance defined as x_{ball}, which provides a downward disturbance force of F_{down} and a reaction force of $F_{reaction}$. The downward deviation of the steel disc is defined by x_{down}. Figure 6.11 illustrates the disturbance test setup.

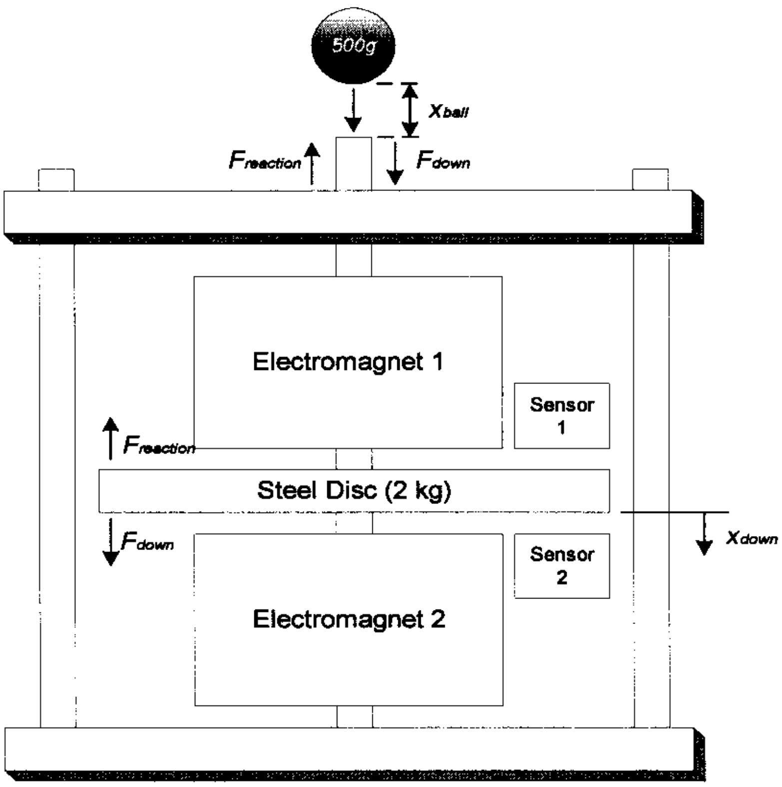

Figure 6.11: Disturbance test on the axial AMB model

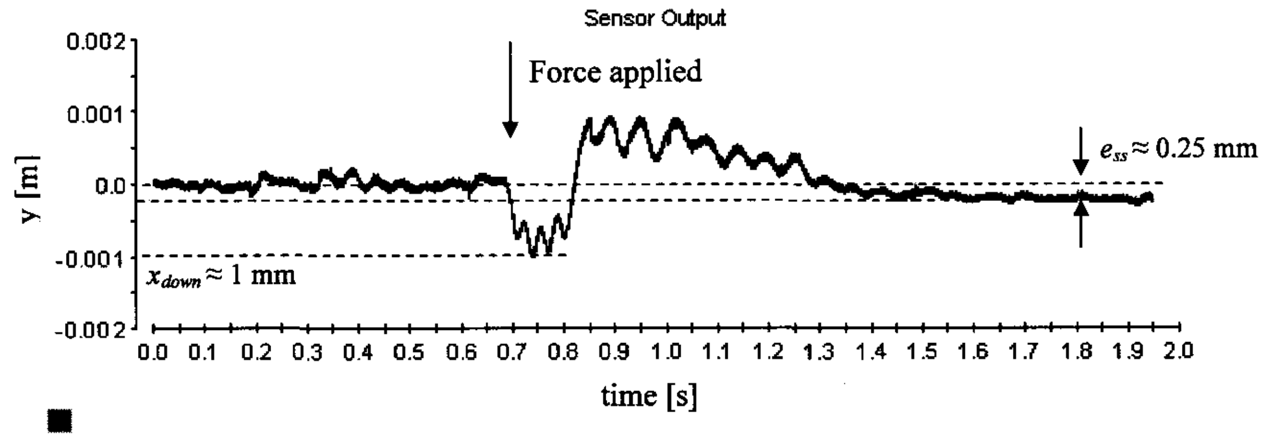

Figure 6.12: Analog lead controller output under disturbance conditions

Figures 6.12 and 6.13 provide outputs of the lead controllers under disturbance conditions. An arrow shows where the force has been applied. The ball height $x_{ball} \approx 5$ mm was chosen and figures 6.12 and 6.13 were captured accordingly. The ball height of ≈5 mm produced a maximum downward deviation of $x_{down} \approx 1$ mm for the analog lead controller and $x_{down} \approx 1.25$ mm for the discrete lead controller.

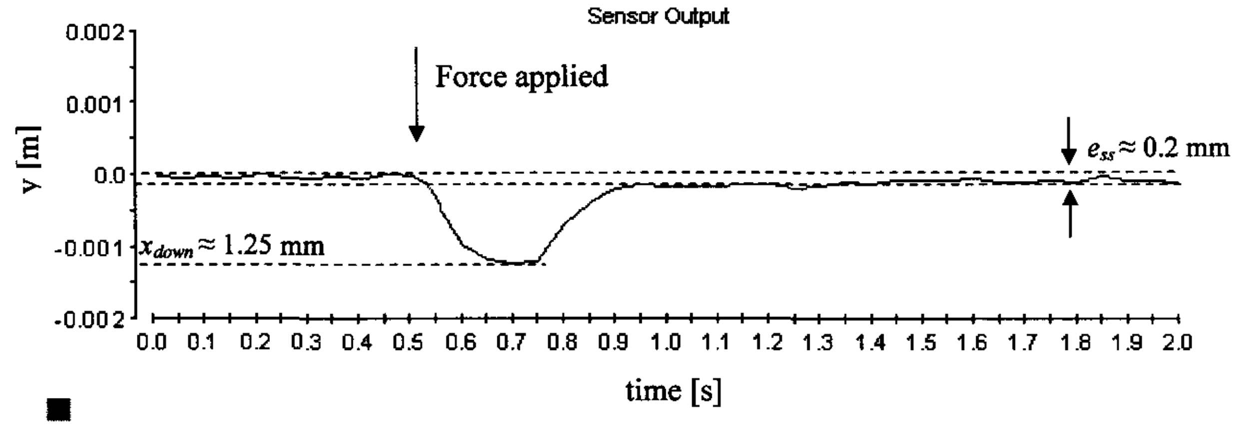

Figure 6.13: Discrete lead controller output under disturbance conditions

Figures 6.14 and 6.15 provide the output of the PID controllers under disturbance conditions. A disturbance force of $x_{ball} \approx 10$ mm was chosen for the analog PID controller (figure 6.14) and produced a maximum downward deviation $x_{down} \approx 1.2$ mm. A disturbance force of $x_{ball} \approx 20$ mm was chosen for the discrete PID controller and produced a maximum downward deviation of $x_{down} \approx 2$ mm. The steady state errors for both PID controllers are zero.

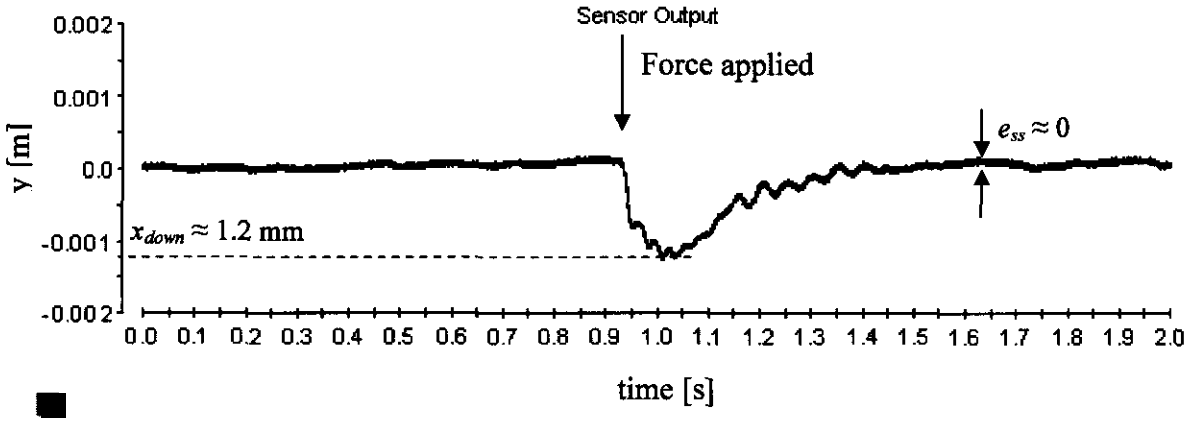

Figure 6.14: Analog PID controller output under disturbance conditions

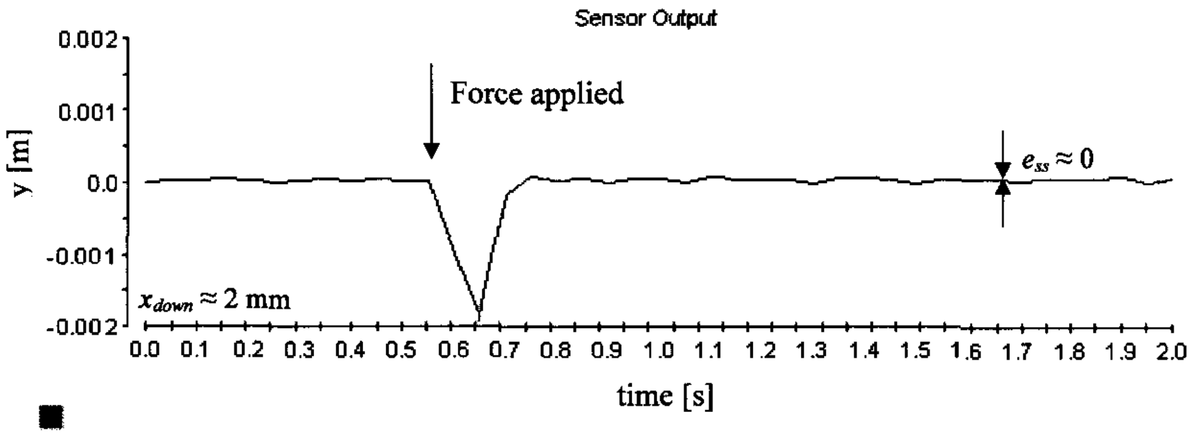

Figure 6.15: Discrete PID controller output under disturbance conditions

Table 6.2 provides the disturbance output of the system with a ball falling from different heights. The maximum deviation and steady state error stays the same for all the controllers when the height of the ball is between 1 – 2 mm. When the ball falls from a height of 25 mm, the steady state errors for the PID controllers are zero. The steel disc at this stage is hammered down onto the bottom electromagnet.

Ball Height x_{ball} [mm]	Maximum Deviation x_{down} [mm]				Steady State Error e_{ss} [mm]			
	Analog Lead	Discrete Lead	Analog PID	Discrete PID	Analog Lead	Discrete Lead	Analog PID	Discrete PID
1-2	0.5	0.5	0.5	0.5	0	0	0	0
5	1.0	1.25	0.8	0.8	0.25	0.2	0	0
10	1.7	1.5	1.2	1.1	0.4	0.3	0	0
15	2.2	2.0	1.7	1.5	0.45	0.35	0	0
20	2.7	2.4	2.2	2.0	0.5	0.4	0	0
25	3	3	3	3	0.55	0.45	0	0

Table 6.2: Data obtained with disturbance test

6.6. EQUIVALENT SPRING-MASS-DAMPER CALCULATION

The AMB system is equivalent to a spring-mass-damper system. In this section the calculation of the spring-mass-damper constants are done. Appendix E provides the calculation of the equations for the constants for the spring-mass-damper. Block diagrams and signal flow diagrams can be found in this appendix.

The following equation was used for the calculation of the natural frequency (ω_n).

$$T_s = \frac{4}{\zeta\omega_n} \qquad T_p = \frac{\pi}{\omega_n\sqrt{1-\zeta^2}} \qquad \omega_n = \sqrt{\frac{\pi^2}{T_p^2} + \left(\frac{4}{T_s}\right)^2}$$

where T_s is the settling time, T_p is the time-to-peak, ω_n is the natural frequency and ζ is the damping ratio.

The following equations will be used for the calculation of the damping constant and stiffness of the model.

$$2\zeta\omega_n = \frac{b_{eq}}{m} \qquad \omega_n^2 = \frac{k_{eq}}{m}$$

$$\therefore b_{eq} = 2\zeta\omega_n m \qquad \therefore k_{eq} = \omega_n^2 m$$

where b_{eq} is the damping constant and k_{eq} is the stiffness.

Table 6.3 shows the system output with variation in input step response amplitude. This table provides information about the time-to-peak, settling time, percentage overshoot, natural frequency, damping ratio, damping constant and stiffness of the different controllers with variation in the input step response amplitude.

Figures 6.4, 6.5, G.6 and G.8 provide graphs of the discrete PID, discrete lead, analog PID and analog lead controller outputs respectively with an input step response.

	Time-to-peak T_p [ms]		Settling Time T_s [ms]		Percentage Overshoot $P.O.$ [%]		Natural Frequency ω_n [rad/s]		Damping Ratio ζ		Damping Constant b_{eq} [$Nm^{-1}s^{-1}$]		Stiffness k_{eq} [N/m]	
Step Response Input Amplitude [mm]	**1.0**	**2.0**	**1.0**	**2.0**	**1.0**	**2.0**	**1.0**	**2.0**	**1.0**	**2.0**	**1.0**	**2.0**	**1.0**	**2.0**
Analog Lead	40	45	180	230	41	46	81.6	71.9	0.272	0.242	88.9	69.5	13324.7	10353
Discrete Lead	30	40	130	190	40	43	109.2	81.3	0.282	0.259	123.1	84.2	23826.0	13223
Analog PID	60	55	190	220	28	37	56.4	59.9	0.373	0.303	84.2	72.7	6369.5	7186.5
Discrete PID	37.5	50	100	160	22	29	92.8	67.6	0.431	0.370	160.0	100.0	17236.8	9145.7

Table 6.3: System output with variation in input step response amplitude

6.7. RESPONSE OF THE DAMPING AND STIFFNESS CONSTANTS OF THE SYSTEM

In this section the stiffness constant (k_{eq}) and damping constant (b_{eq}) of the discrete PID controller will be evaluated with a change in the proportional gain (K_p) and derivative gain (K_D).

Figure 6.16 provides a graph of the stiffness constant with a change in the proportional gain. From this graph it can be seen that when the proportional gain of the discrete PID controller increases, the stiffness constant also increases.

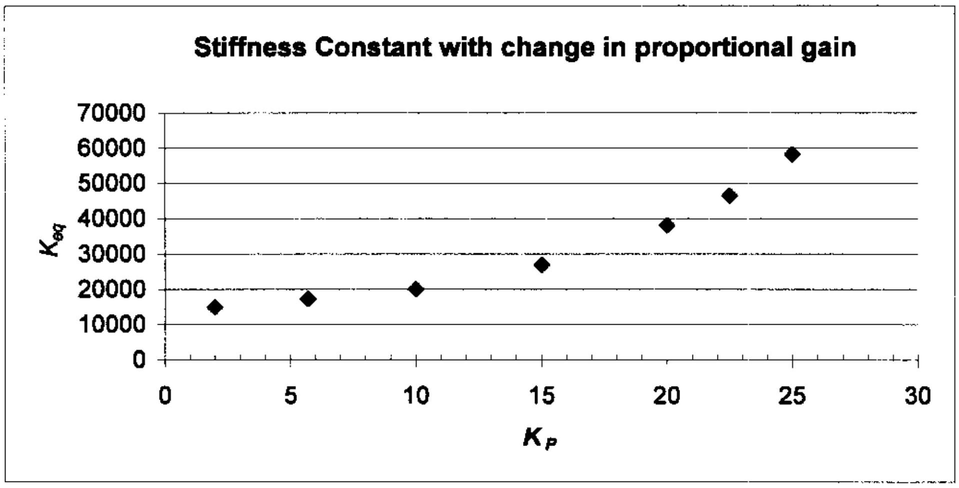

Figure 6.16: Stiffness constant with a change in the proportional gain

The experimental data of the damping constant with a change in the derivative gain can be seen in figure 6.17. From this figure it can be seen that an increase in the derivative gain of the discrete PID controller, leads to an increase in the damping constant. This figure has an almost linear response.

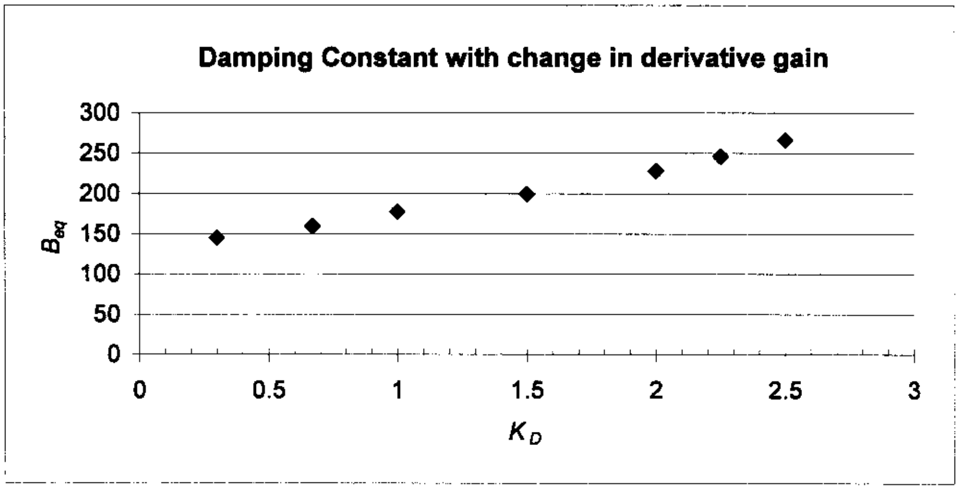

Figure 6.17: Damping constant with a change in the derivative gain

6.8. CONCLUSIONS

The dSpace® Controldesk interface provides useful signal information at different operating points. The signal coming from the sensor, input signals to the controllers and output signals going to the actuators can all be seen in Controldesk. A model can be designed and tested in Simulink®, before it is downloaded onto the real-time controller.

CHAPTER 7
CONCLUSIONS AND IMPROVEMENTS

7.1. CONCLUSIONS

The depth parameter in Quickfield® can only be measured in block format and has a fixed value of 100 cm. This caused a problem in terms of the accuracy of the data obtained. A better finite element package must be used in the future.

Quickfield® does not make provision for 3 dimensional simulations and therefore only two dimensional simulations can be done. For accurate results a 3 dimensional package must be used. Software packages like Ansys® and Algor® must be looked at.

The induction sensor is used to measure the distance of the air gap between the steel disc and the electromagnets. The distance between the air gap and the output voltage has a linear response. This makes it ideal to use the sensor over a wide air gap range.

The model was started by using PWM power amplifiers and an induction sensor for position feedback. This provided serious problems, since all the noise/switching generated by the PWM power amplifiers was carried onto the induction sensor. The model was then earthed, shielded cables were used and the power amplifiers were shielded in any way possible.

Although the PWM power amplifiers and induction sensor work perfectly when driven separately, they did not want to work together. This problem could not be fixed and it was decided to switch the optical sensors, but the same problem occurred with the optical sensors. Somehow the noise generated by the PWM power amplifiers gets into the system.

Finally it was decided to throw out the PWM power amplifiers and use power transistors instead. The induction sensor was brought back and the system was tested again. The amount of noise in the system is now al lot less that with the previous attempts.

The dSpace® Controldesk interface provides useful signal information at different operating points. The signal coming from the sensor, input signals to the controllers and output signals going to the actuators can all be seen in Controldesk.

dSpace® provides a real-time interface (RTI) between Simulink® and Controldesk, making it possible to design and test a Simulink® model before it is downloaded onto the real-time controller.

From the steady state error (e_{ss}) obtained during the load test (table 6.1), the conclusion can be made that the PID controllers are the better controllers, since it has smaller steady state errors. The lead controllers are also suspending the disc, but it has larger steady state errors.

From the data obtained for the disturbance test (table 6.2), the conclusion can be made that the PID controllers are also the better controllers (in terms of the e_{ss}). The lead controllers also recover from the disturbance, but have larger steady state errors.

7.2. IMPROVEMENTS

The project objective was to develop a working axial AMB system, on which measurements and tests can be conducted in a research environment. This objective was met and it is now possible to make improvements on the system.

Possible future projects can be done on the improvement of the sensors (designing a sensorless sensor), designing advanced control techniques for the axial AMB model by using the dSpace® DS1104 controller and designing an axial AMB model for high speed rotation.

Improvements on the sensors are possible by increasing the linear area of the inductive sensors, increasing the signal to noise ratio (SNR) and improving the bandwidth of the sensor. The linear area can be improved by using a full-wave active rectifier instead of a half-wave active rectifier and obtaining the optimum impedance for the desired air gap. This optimum impedance can be calculated by using the following equations: $L_1 = L_0 \dfrac{d}{d-x}$ and $L_2 = L_0 \dfrac{d}{d+x}$.

Increasing the SNR is possible by increasing the frequency and by designing a notch filter with a steeper cut-off (higher order filter), using integrated components with a high SNR and using components which are not sensitive to noise in the specific frequency band. Care must be taken with the value of C7, since it determines the amount of ripple in the output of the sensors.

The project can further be improved by designing advanced control techniques for the dSpace® controller. For this advanced control techniques fuzzy logic control, sliding mode control, advanced PID control, H^{∞} control, adaptive variable bias control, advanced adaptive autocentering control and Mu synthesis control can be looked at. These advanced control techniques can all be implemented in the dSpace® real-time interface (RTI).

The designing of an axial AMB model for high speed applications can be taken a step further. Principles like hall-back effects, flux-canceling effects and using electrodynamic suspension (EDS) with electromagnetic suspension (EMS) can be investigated.

The model can further be improved by using precision eddy current probes, intergated displacement and velocity probes and designing a sensorless sensor. Improvements on the actuating amplifiers can be done by using PWM power amplifiers or investigating linear power amplifiers.

CHAPTER 8

LIST OF REFERENCES

[1] Ahrens M., Kucera L. and Larsonneur R., "Performance of a Magnetically suspended flywheel energy storage device", *IEEE Transactions on Control System Technology*, Vol. 4, No. 5, September 1996

[2] Alaire P., Knospe C.P., et al., "Short course on magnetic bearings", Alexandria, Virginia, August 19-20, 1997

[3] Allaire P.E., "First magentic bearings", Mechanical and Aerospace Engineering Dept., University of Virginia, Charlottesville, VA 22901, 1997

[4] Allaire P.E., Maslen E.H., "Introduction to magnetic bearings", Mechanical and Aerospace Engineering Dept., University of Virginia, Charlottesville, 1997

[5] Allaire P.E., Maslen E.H. and Lewis D.W., "Magnetic thrust bearing operation and industrial pump application", Department of Mechanical, Aerospace and Nuclear Engineering, ROMAC Laboratory, Charlottesville, May 1997

[6] Hertzog R., Buhler P., et al. (September 1996). Unbalance compensation using generalized notch filters in the multivariable feedback of magnetic bearings. *IEEE Transactions on control system technology: Special issue on magnetic bearings control.* Vol. 4, no.5, pp580-585.

[7] Hultman A. and Eriksson M.L., The attraction of magnetic bearings. [Online]. Available:http://www.evolution.skf.com/gb/article.asp, [Date of access: March 2003]

[8] Hung Y., "Magnetic Bearing Control Using Fuzzy Logic", *IEEE* Department of Electrical Engineering, Auburn University, AL 36849-5201, 1997

[9] Kasarda M.E.F., "An Overview of Active Magnetic Bearing Technology and Applications", March 2000, The shock and vibration digest. Vol. 32, no 2, pp 91-99

[10] Knospe C., Collins E. G., "Introduction to the special issue on magnetic bearing control", University of Virginia, Charlottesville, 1997

[11] Liebert W., "Performance Evaluation of a Fast Digital Fuzzy Controller for an Active Magnetic Bearing", Laboratory of Electrical Engineering Design, Zürich, Switzerland, 1996

[12] McCloskey T., "Guidelines for the use of magnetic bearings in turbomachinery", Technology insights, San Diego, Calafornia, February 1996

[13] Miller H., Ahrens M., Totally enclosed inline electric motor driven gas compressor, Dresser-Rand Co., Available: http://www.dresser-rand.com [Date of access: April 2004]

[14] Newcastle University. Modern Flywheel Uninterruptible Power Supplies. [Online]. Available: http://murray.newcastle.edu.au/users/students/2001/c9605166/modern_ups.htm, [Date of access: April 2004]

[15] Pretorius J.H.C., "A three dimensional magnetic bearing for high speed rotors", Dissertation-M.S.C., Johannesburg: RAU, 1982

[16] Revolve magnetic Bearings Inc. Magnetic bearing. [Online]. Available: http://www.revolve.com/Technology/magbearings.html, [Date of access: March 2003]

[17] Rundell, A. E., Drakunov, S. V., and DeCarlo, R. A., "A Sliding Mode Observer and Controller for Stabilization of Rotational Motion of a Vertical Shaft Magnetic Bearing," *IEEE Transactions on Control Systems Technology*, Vol.4, 598-608, September 1996

[18] Scherpen J.M.A., "Nonlinear Control for Magnetic Bearings in Deployment Test Rigs: Simulation and Experimental Results", Faculty of Information Technology & Systems, Dept. of Electrical Engineering, USA, pp. 2613–2618, 1996

[19] Schweitzer G, "Active magnetic bearings - chances and limitations", *International Centre for Magnetic Bea rings, ETH Zurich,* vdf Hochschulverlag AG, 1998

[20] Sinha, P.K., "Electromagnetic Suspension Dynamics & Control", IEE control engineering series; v.30, England, 1987

[21] Takahashi N, "Optimization of Die Press Model", Department of Electrical and Electronic Engineering, Okayama University, Japan, 1998

[22] Tessier L.P., The development of an auxiliary bearing landing system for a flexible active magnetic bearing supported hydrogen process compressor rotor. From Proceedings: MAG' 97, Alexandria, USA, 1997. [Online]. Available: http://www.revolve.com/Technology/Pdf/dpmt_auxbrg_landing.pdf, [Accessed: March 2003]

[23] Thompson M.T., "Electrodynamic Magnetic Suspension—Models, Scaling Laws, and Experimental Results", *IEEE Transactions on Education*, VOL. 43, NO. 3, August, 2000

[24] University of Virginia, Jesse W. Beams 1898 – 1977, [Online]. Available: www.phys.virginia.edu/History/Beams/beams_and_johnson.jpg, [Date of access: May 2003]

[25] Waukeshu Bearings Corporation. The Benefits of Magnetic Bearings. [Online]. Available: http://www.magnetic.waukbearing.com/products/magnetic_benefits/magnetic_benefits.html, [Date of access: March 2003]

[26] Yang C. and Knospe C., "Optimal Control of a Magnetic Bearing without Bias Flux Using Finite Voltage", Department of Mechanical and Aerospace Engineering, University of Virginia.

[27] Zeisberger M. and Gawalek W. (1998), Losses in magnetic bearings. Materials Science and Engineering, no B53, pp193-197. Available: http://www.sciencedirect.com [Date of access: March 2003]

APPENDIX A

PHOTOS OF THE AMB MODEL

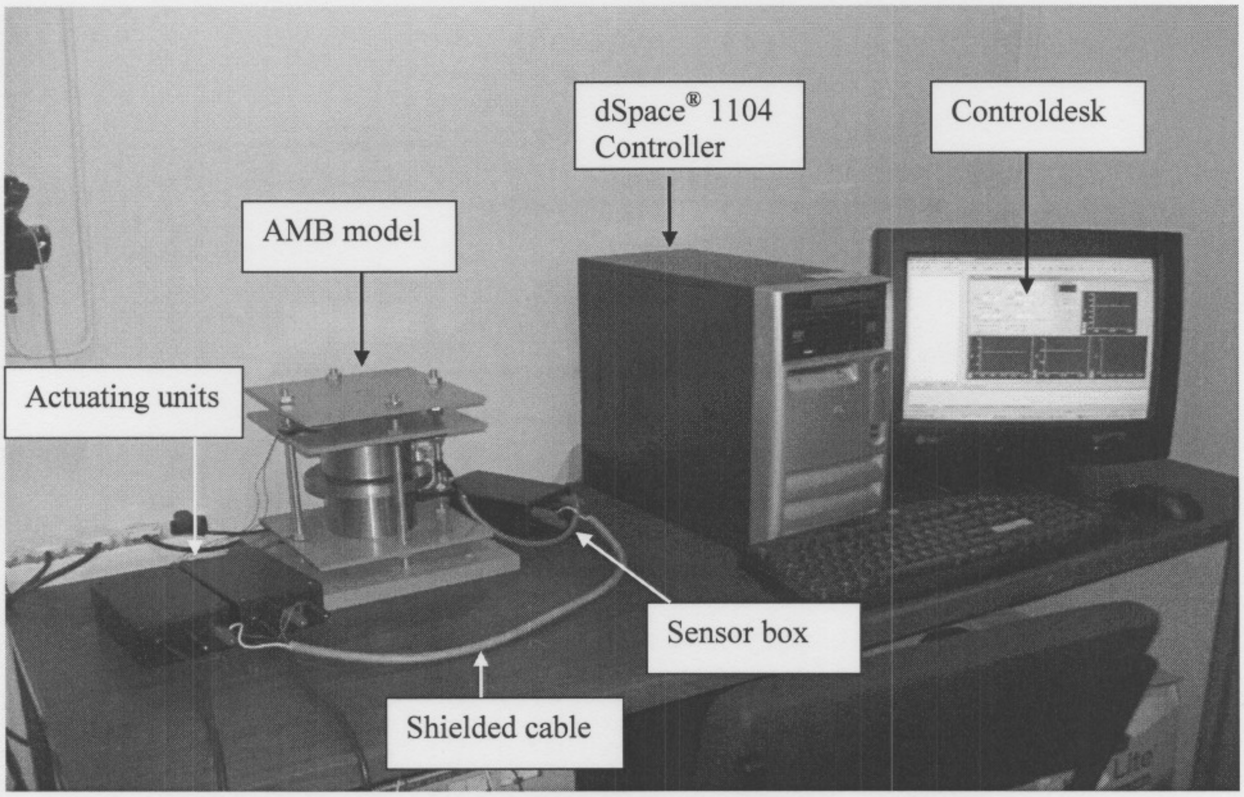

Figure A.1: Complete Axial AMB system

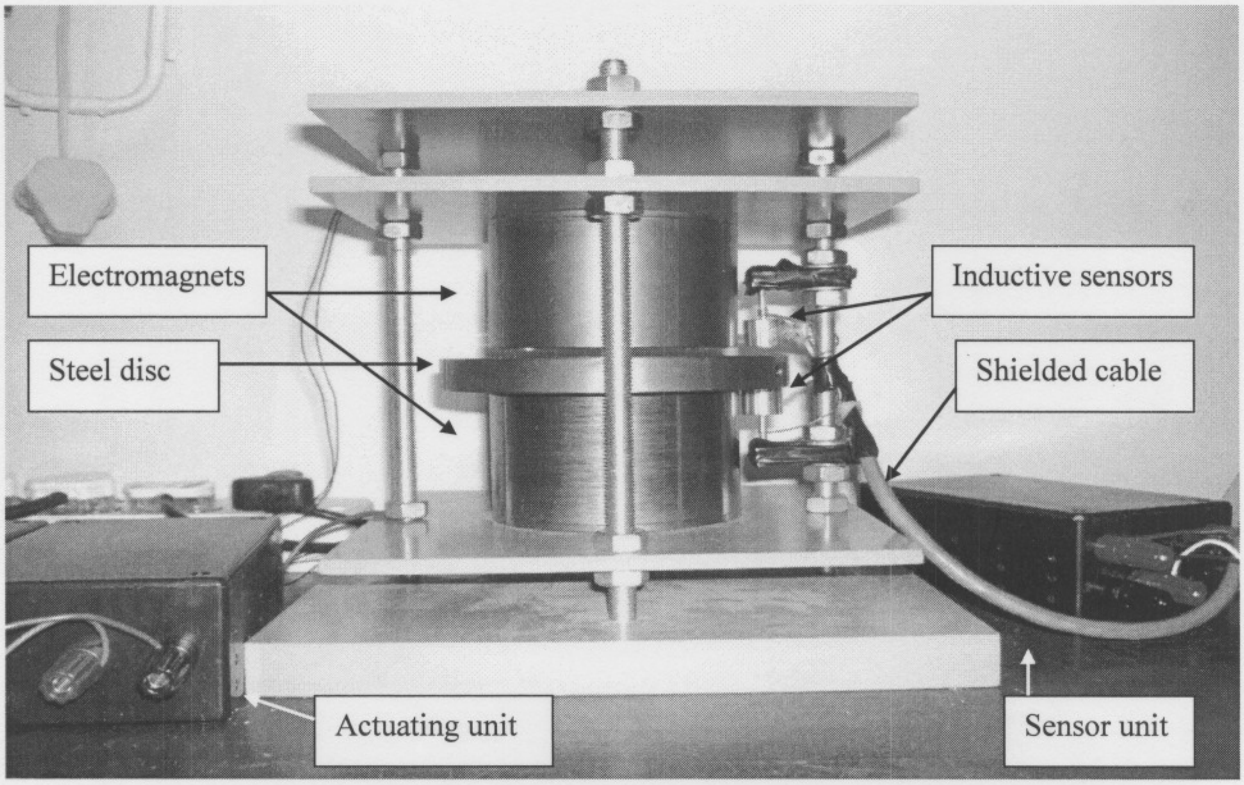

Figure A.2: Close-up of the Axial AMB model

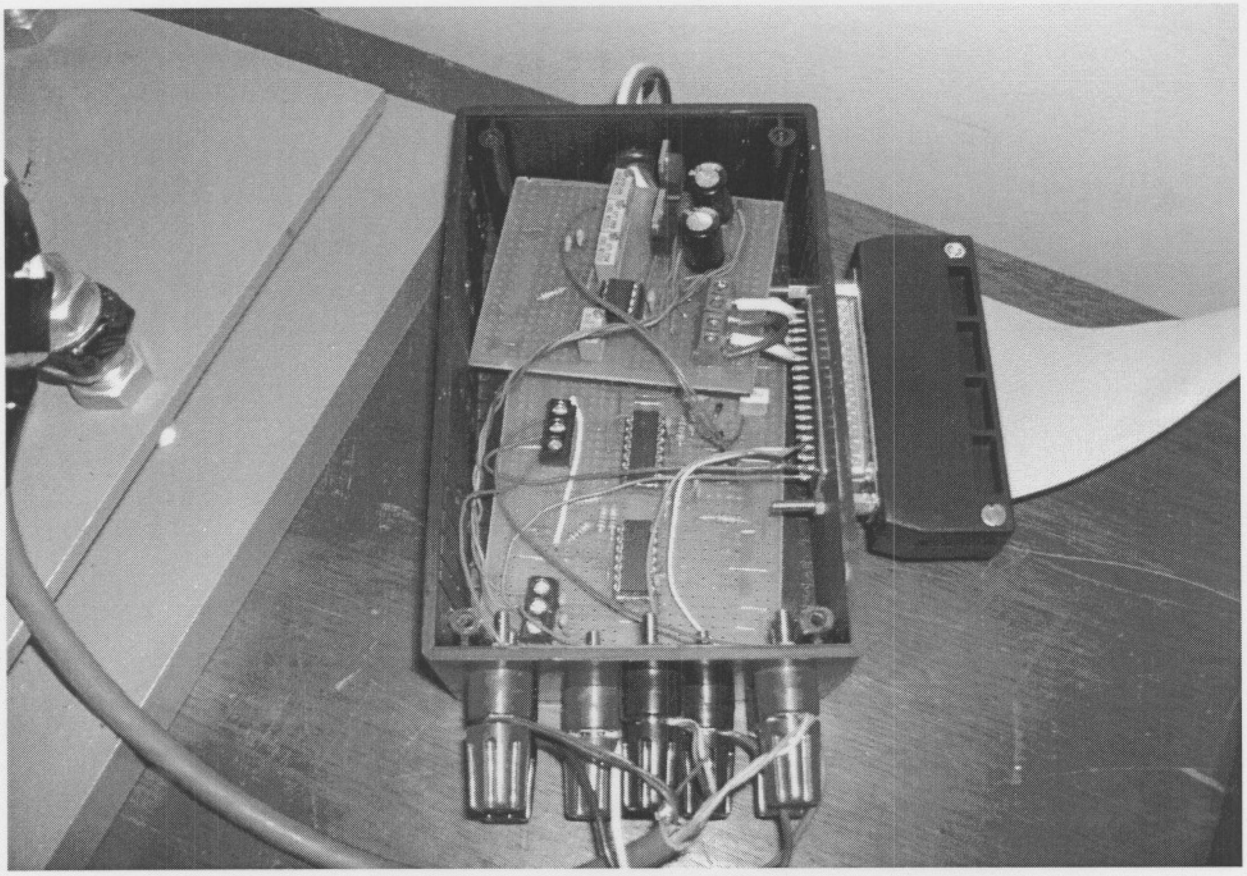

Figure A.3: Inside the sensor unit

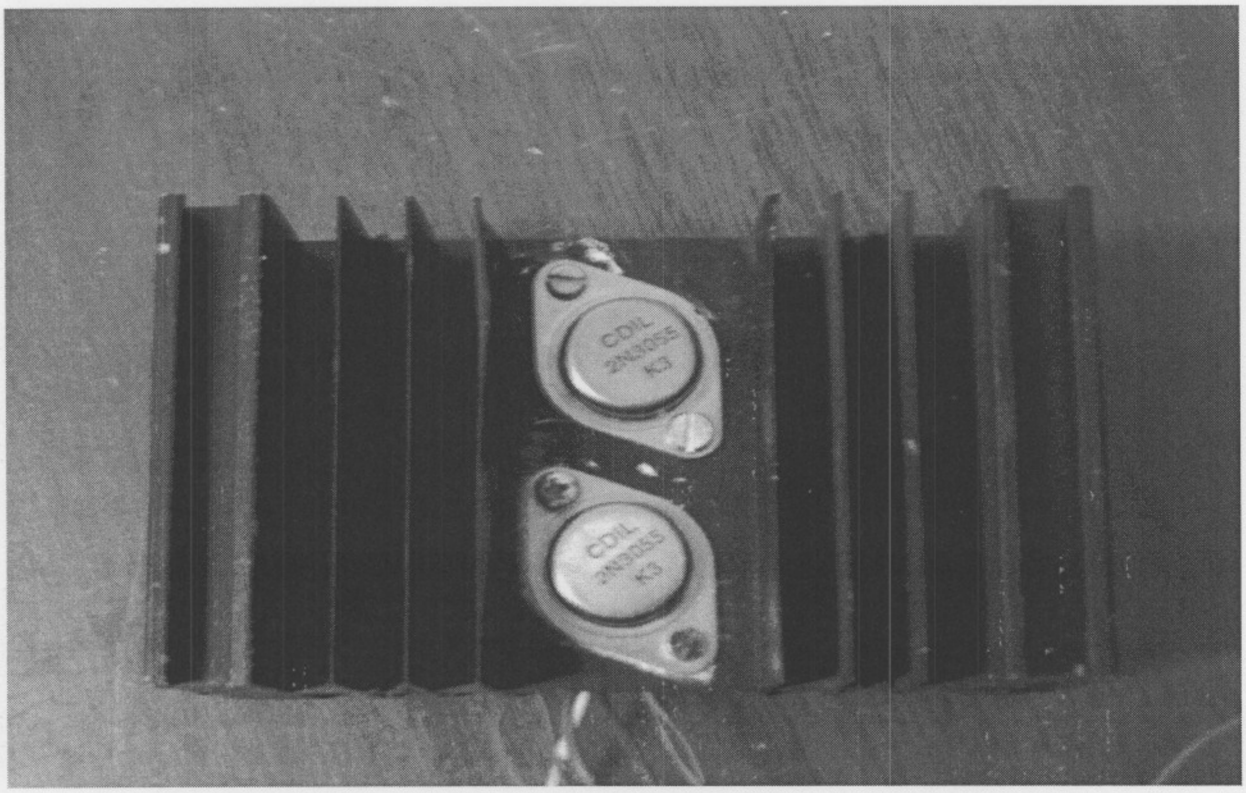

Figure A.4: Actuator unit

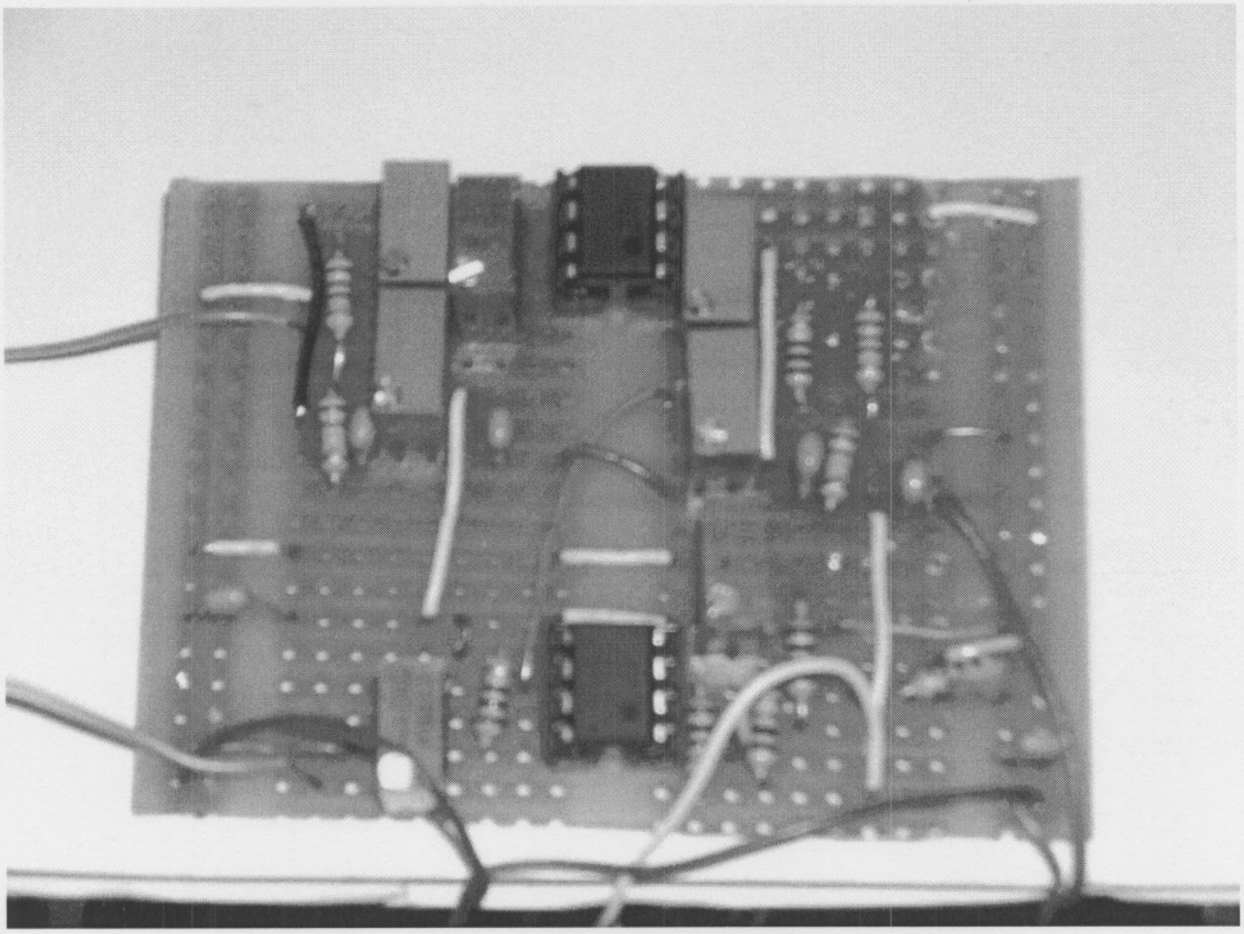

Figure A.5: Lead controllers

These photos are best viewed in full colour. All of the photos in this section are available on the CD, available on request.

APPENDIX B

CIRCUIT DIAGRAMS

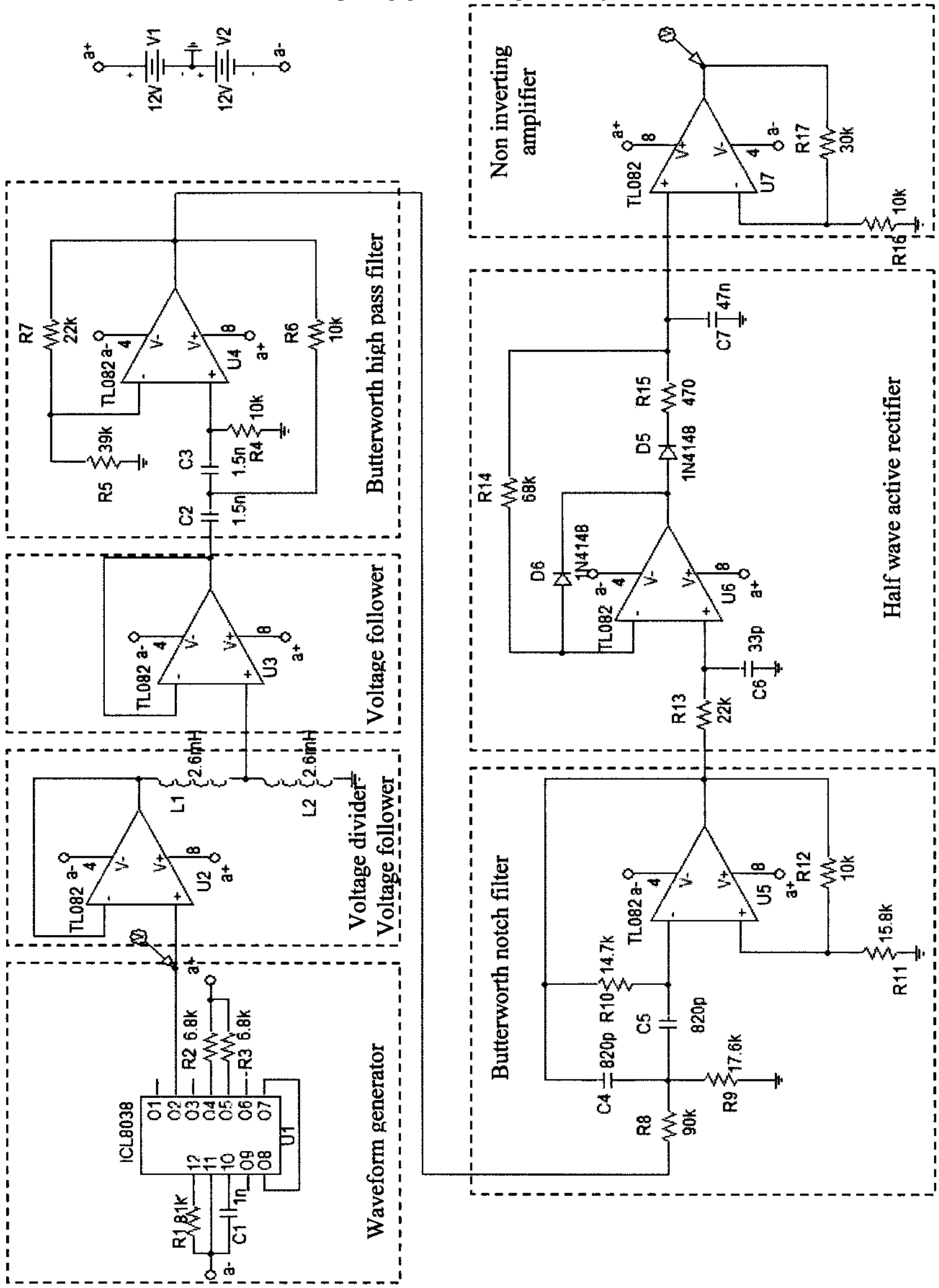

Figure B.1: Position sensor circuit diagram

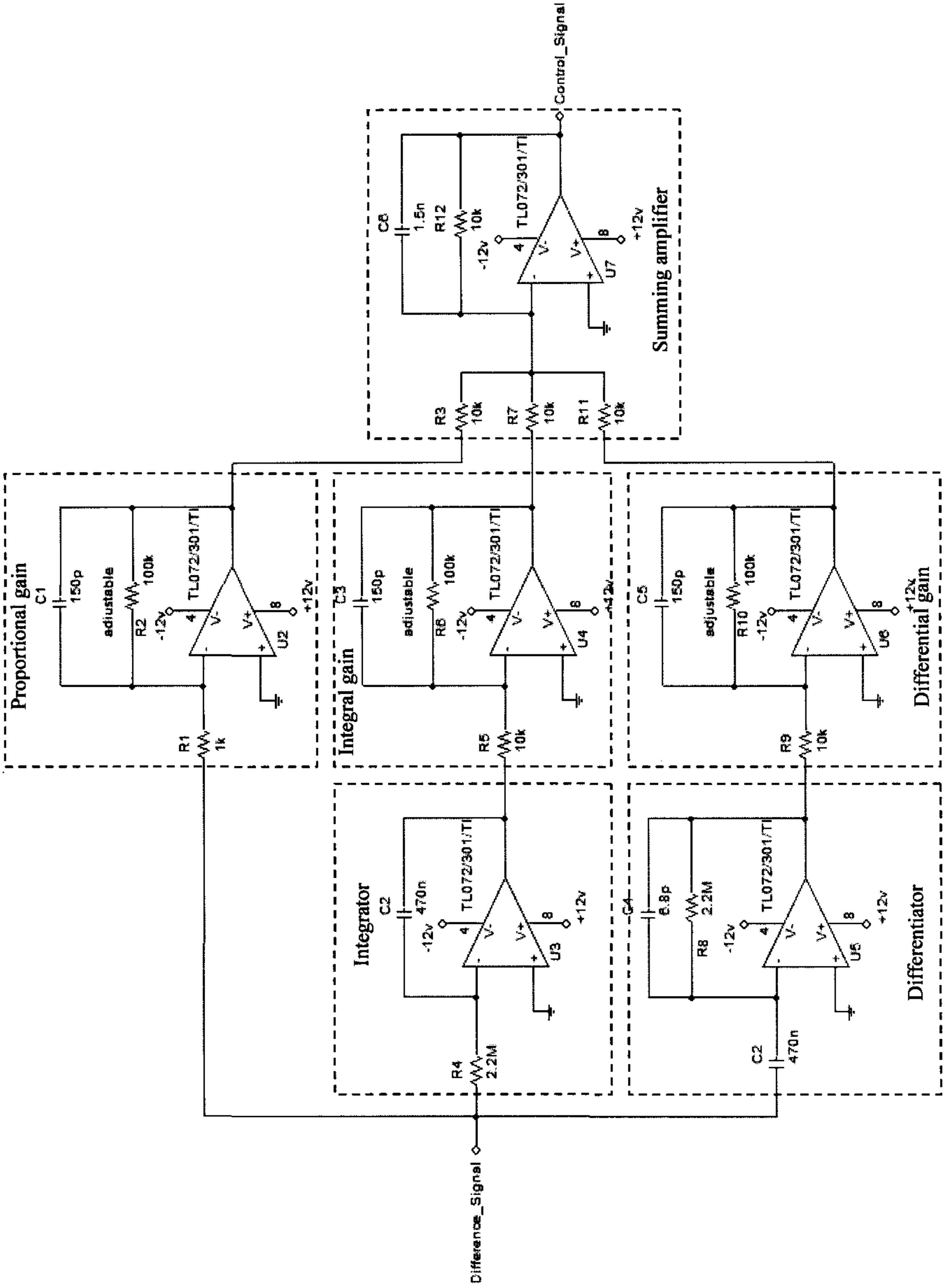

Figure B.2: PID controller with active differential gain

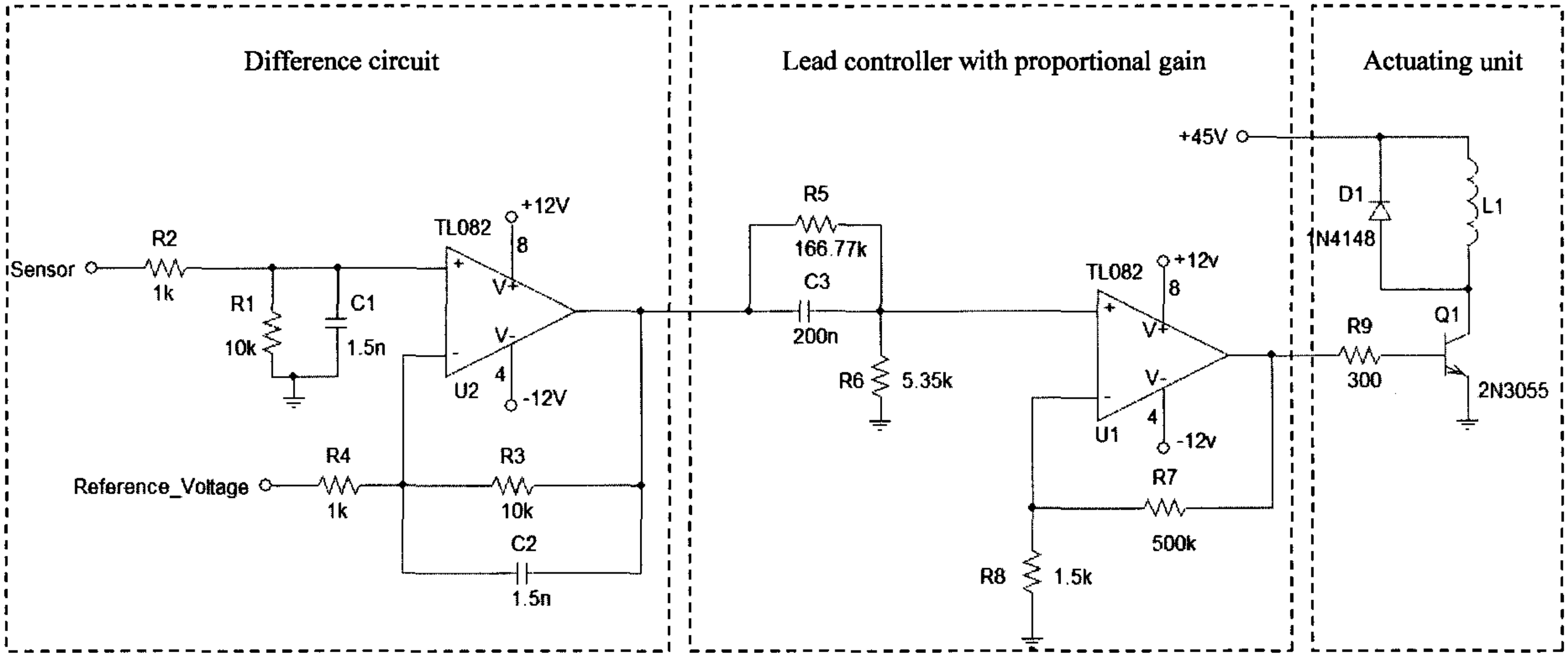

Figure B.3: Lead controller and actuator circuit diagram

APPENDIX C

MECHANICAL DESIGN OF THE AXIAL AMB MODEL

This section gives additional information about the mechanical design of the project. Figure C.4 gives the total construction of the model. From this figure it can be seen where the basis plate and steel rods (figure C.1), middle plate (figure C.2) and top plate (figure C.3) fit in.

Figure C.5 gives a 3-D view of the complete axial AMB model. From this figure the suspended disc (blue), top and bottom c-shaped electromagnets (green), magnet coil (red) and position sensor (brown) can be seen.

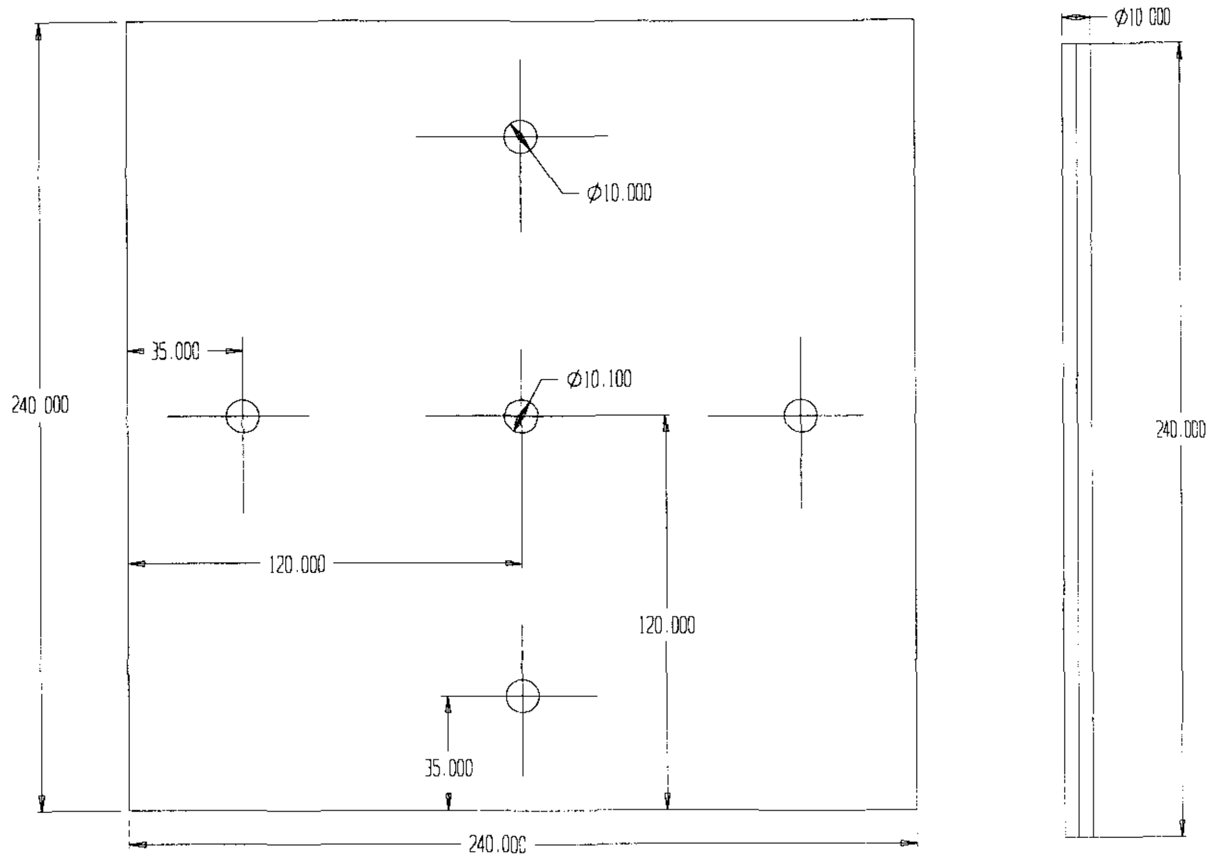

Figure C.1: Basis plate and steel rod

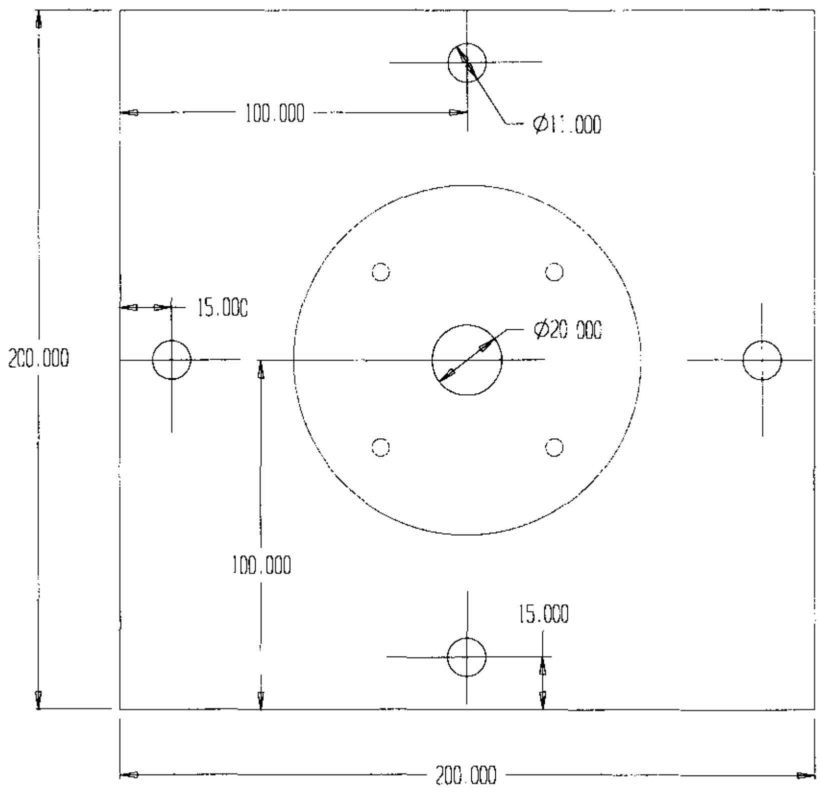

Figure C.2: Middle plate

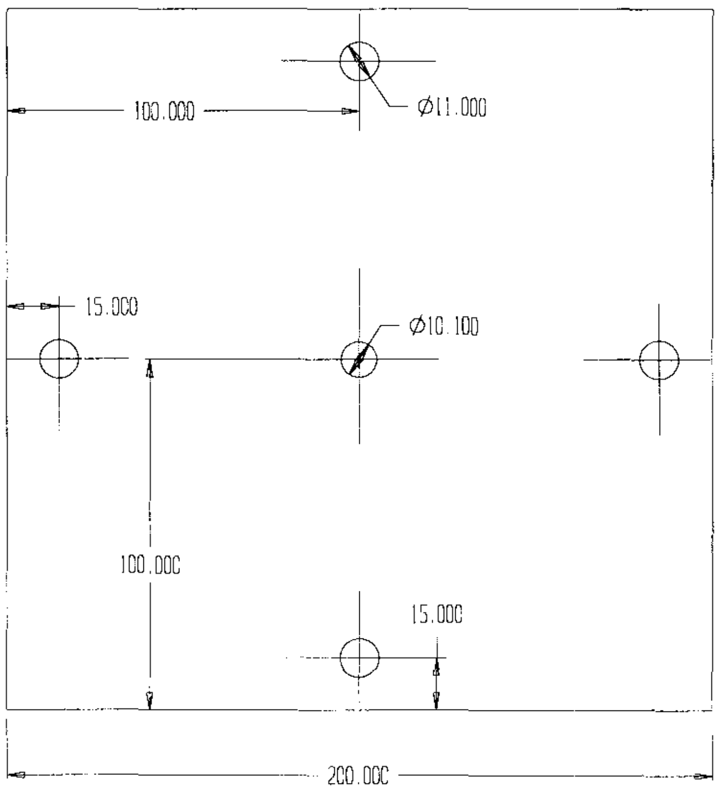

Figure C.3: Top plate

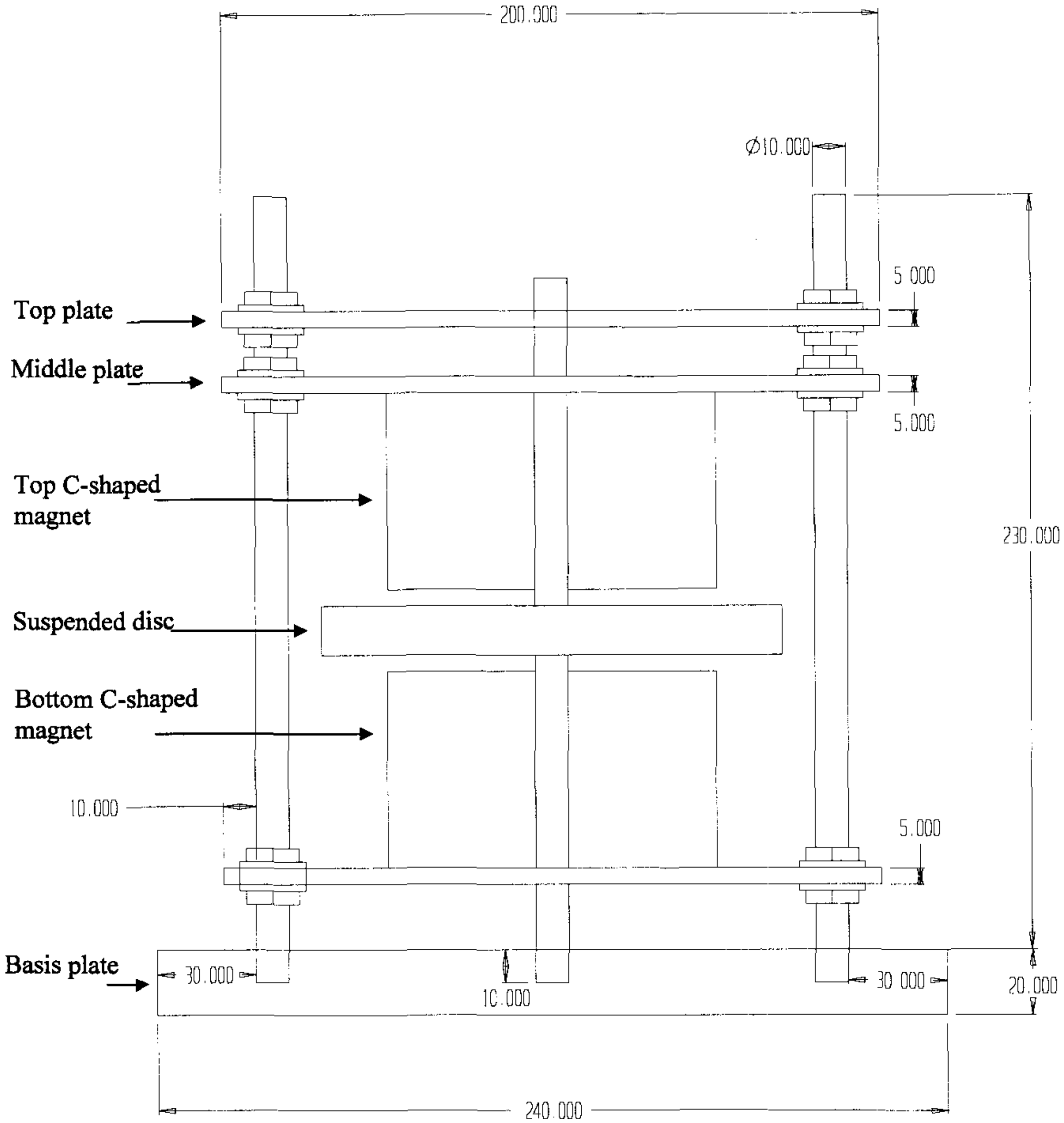

Figure C.4: Total construction of the model

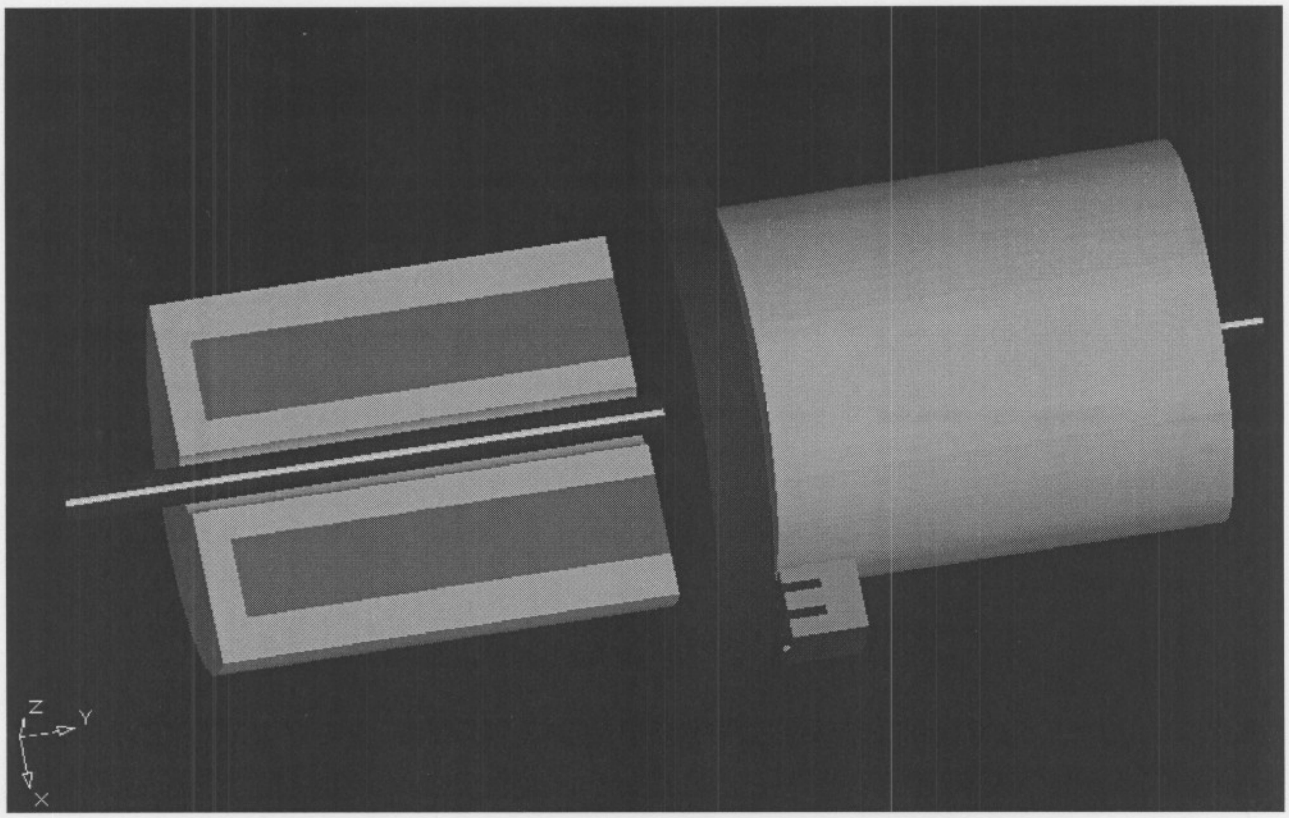

Figure C.5: 3-D view of the complete axial AMB model[2]

Figure C.5 provides a 3-D drawing of the complete axial active AMB model, showing both electromagnets. The left electromagnet is a cross-sectional view showing the coil (red), the core (green) and the steel rod (blue) running through the centre. The placement of the inductive sensor (brown) can be seen on the right side of the steel base.

[2] This picture is available in full colour on the CD, file: Model_complete2.gif, available on request.

APPENDIX D
QUICKFIELD® ANALYSIS OF THE MODEL

This section provides additional information on the Quickfield® analysis done in chapter 3. From these figures the mesh, potential, flux density, field strength, energy density and permeability of both the c-shaped magnets can be seen.

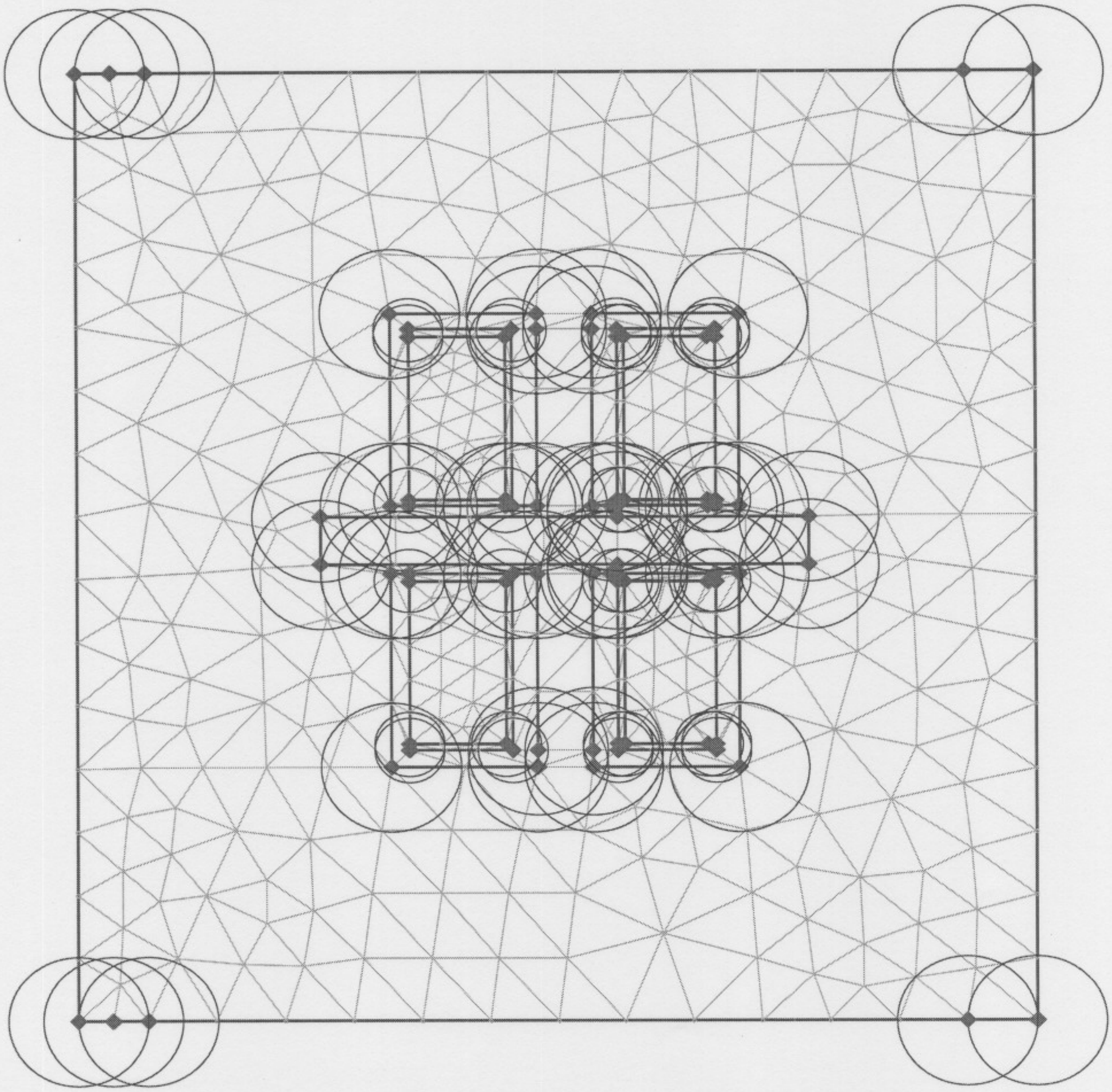

Figure D.1: Mesh of the complete system

Figure D.1 shows the electromagnets viewed in geometry mode. The total number of nodes was limited to 192. The mesh is the small green lines filling up the rectangles. The circles show the spacing needed to create the mesh. The air parameter was designed with 2 cm spacing and the coil and steel parameters was designed with 1 cm spacing.

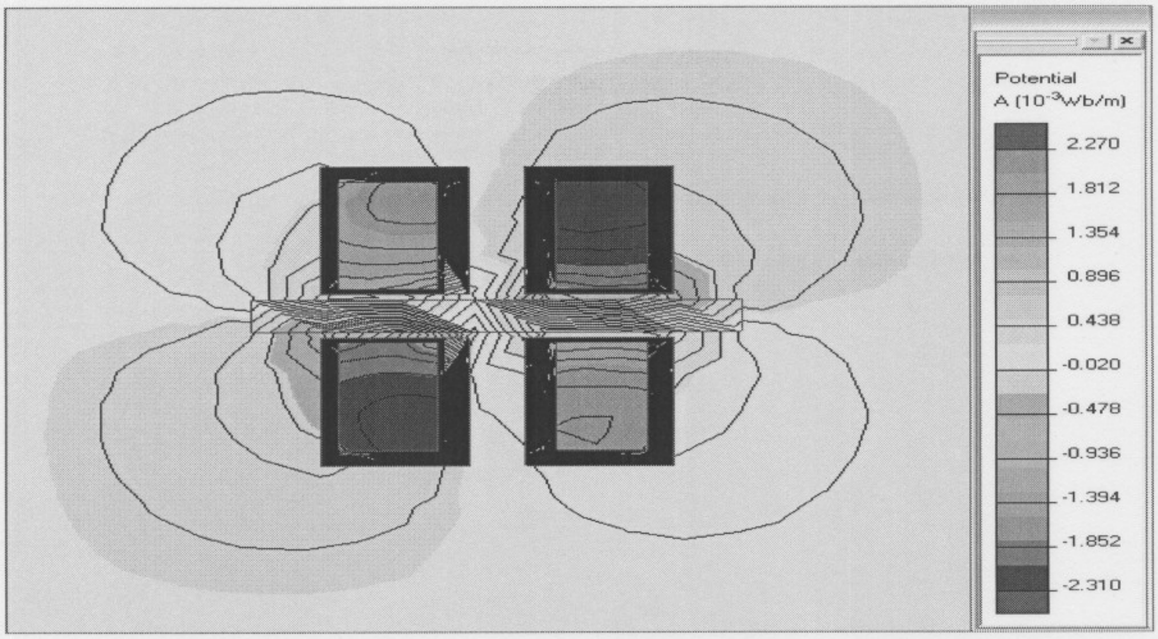

Figure D.2: Potential of both c-shaped magnets[3]

Figure D.2 is viewed in analysis mode. This figure was analysed with a potential color map, this is shown on the right side of the figure. From this figure it can be seen that the positive coil parameter has the most potential, whereas the negative coil parameter has the least potential.

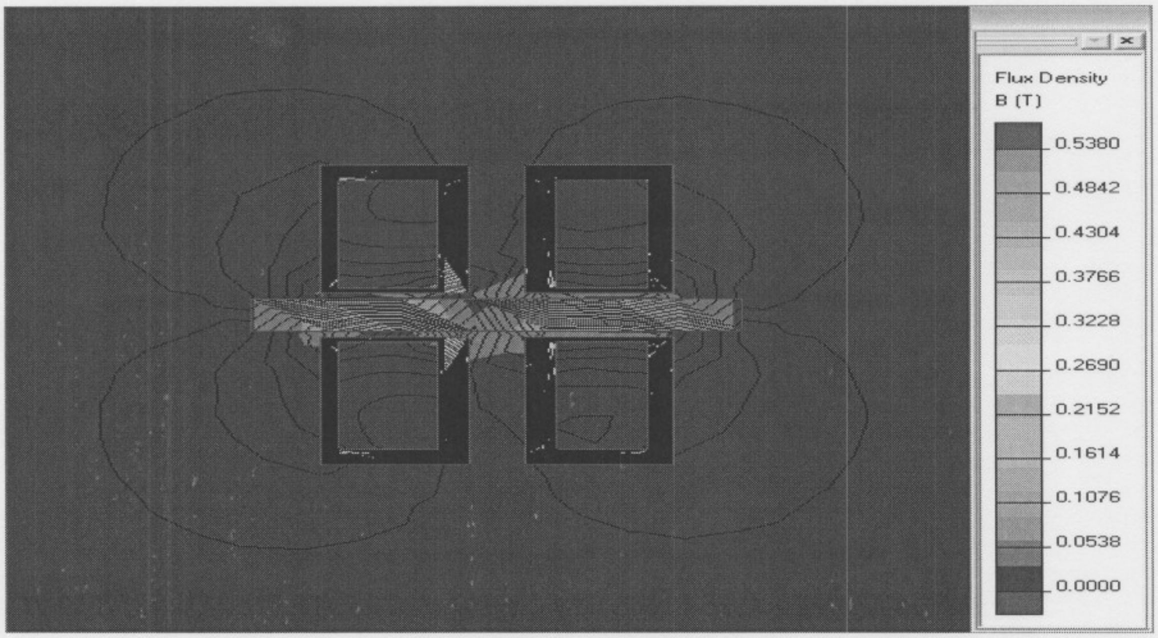

Figure D.3: Flux density of both c-shaped magnets[4]

Figure D.3 shows the flux density of both the c-shaped magnets. From this figure it can be seen that the highest flux density is between the electromagnets and the steel base.

[3,4] These pictures are available in full colour on the CD, available on request.

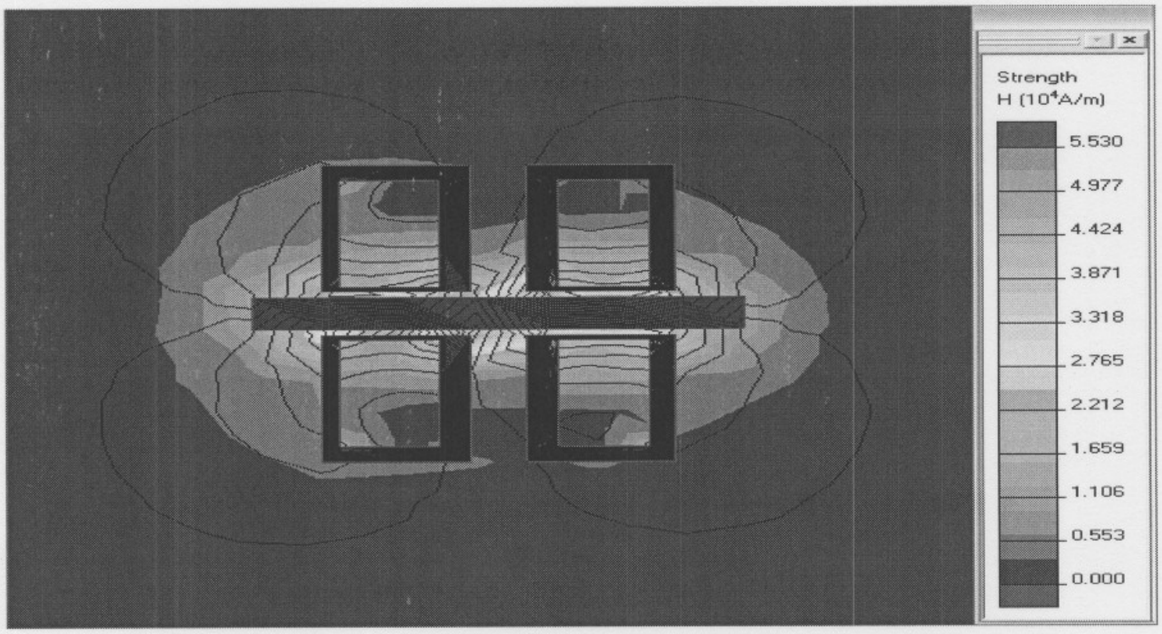

Figure D.4: Strength of both the c-shaped magnets[5]

From figure D.4 it can be seen that the strength H is the highest between the electromagnets and the steel disc. The strength H = 29686 A/m at this point.

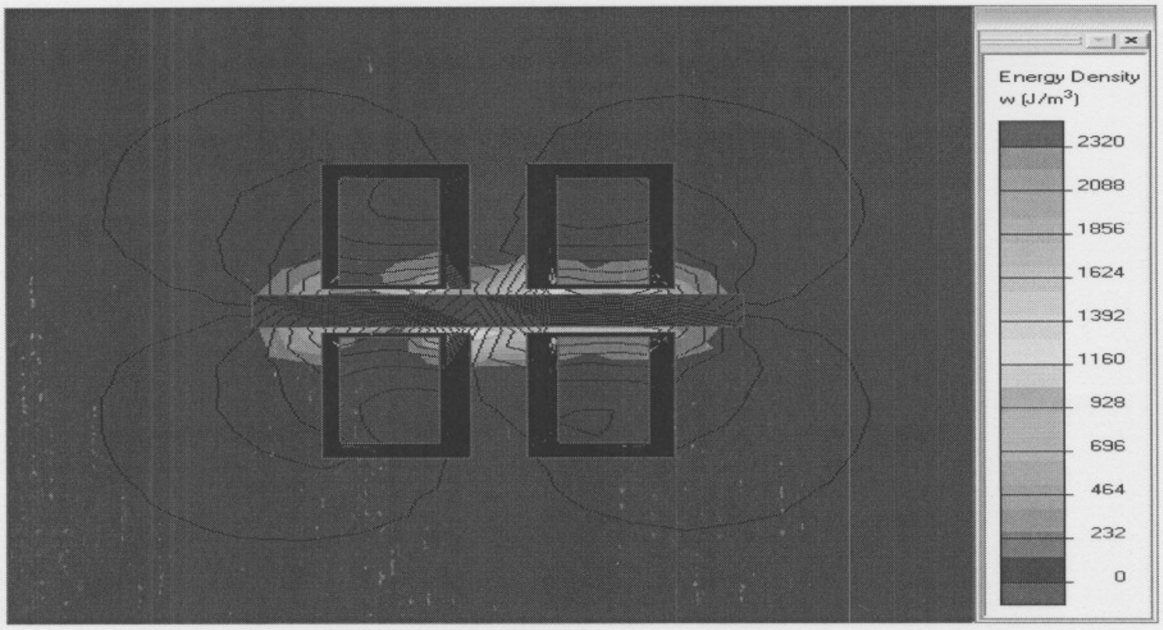

Figure D.5: Energy density of both the c-shaped magnets[6]

The energy density also reaches it maximum between the electromagnets and the steel base. This maximum energy density w = 564.76 J/m^3.

[5,6] These pictures are available in full colour on the CD, available on request.

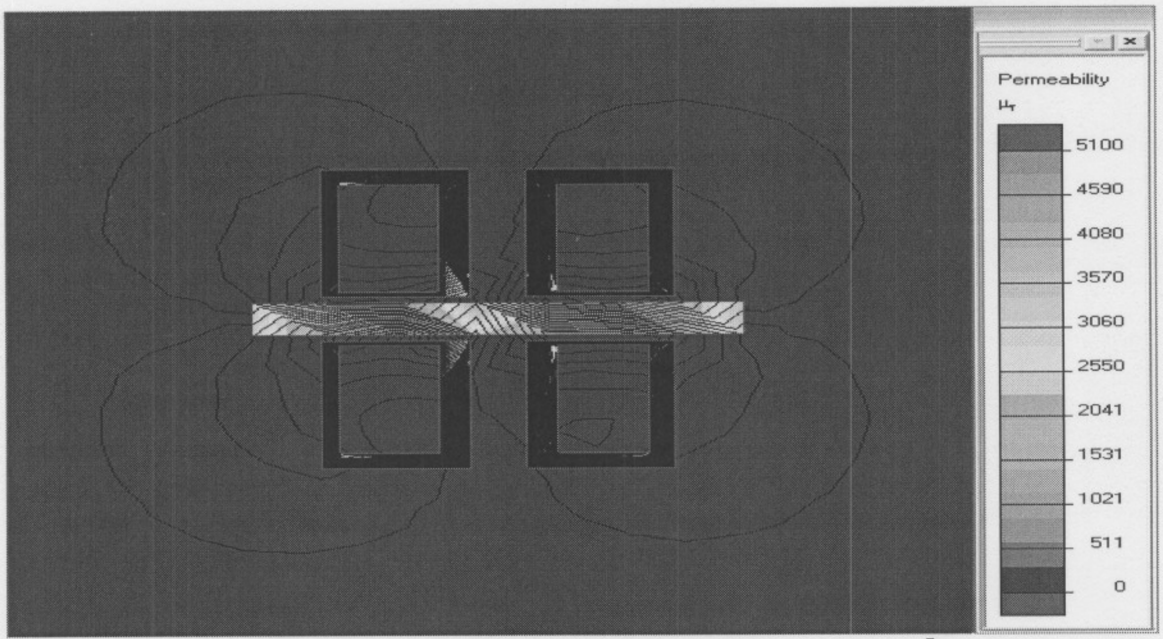

Figure D.6: Permeability of both the c-shaped magnets[7]

From figure D.6 it can be seen that the maximum permeability is inside the steel base. This maximum permeability is μ_r = 4260.3. Care must be taken with the values obtained with the Quickfield® simulations, since the depth parameter for these simulations are in block format.

The electromagnets have a cylindrical shape with diameter of 100 cm, therefore the results obtained with Quickfield® is not precisely correct and have to be fitted. The results give a good estimate and can be used for verification purposes.

Quickfield® does not make provision for 3 dimensional simulations and therefore only two dimensional simulations can be done. For accurate results in the 3rd dimension a software package like Ansys® would be better.

[7] This picture is available in full colour on the CD, available on request.

APPENDIX D
QUICKFIELD® ANALYSIS OF THE MODEL

This section provides additional information on the Quickfield® analysis done in chapter 3. From these figures the mesh, potential, flux density, field strength, energy density and permeability of both the c-shaped magnets can be seen.

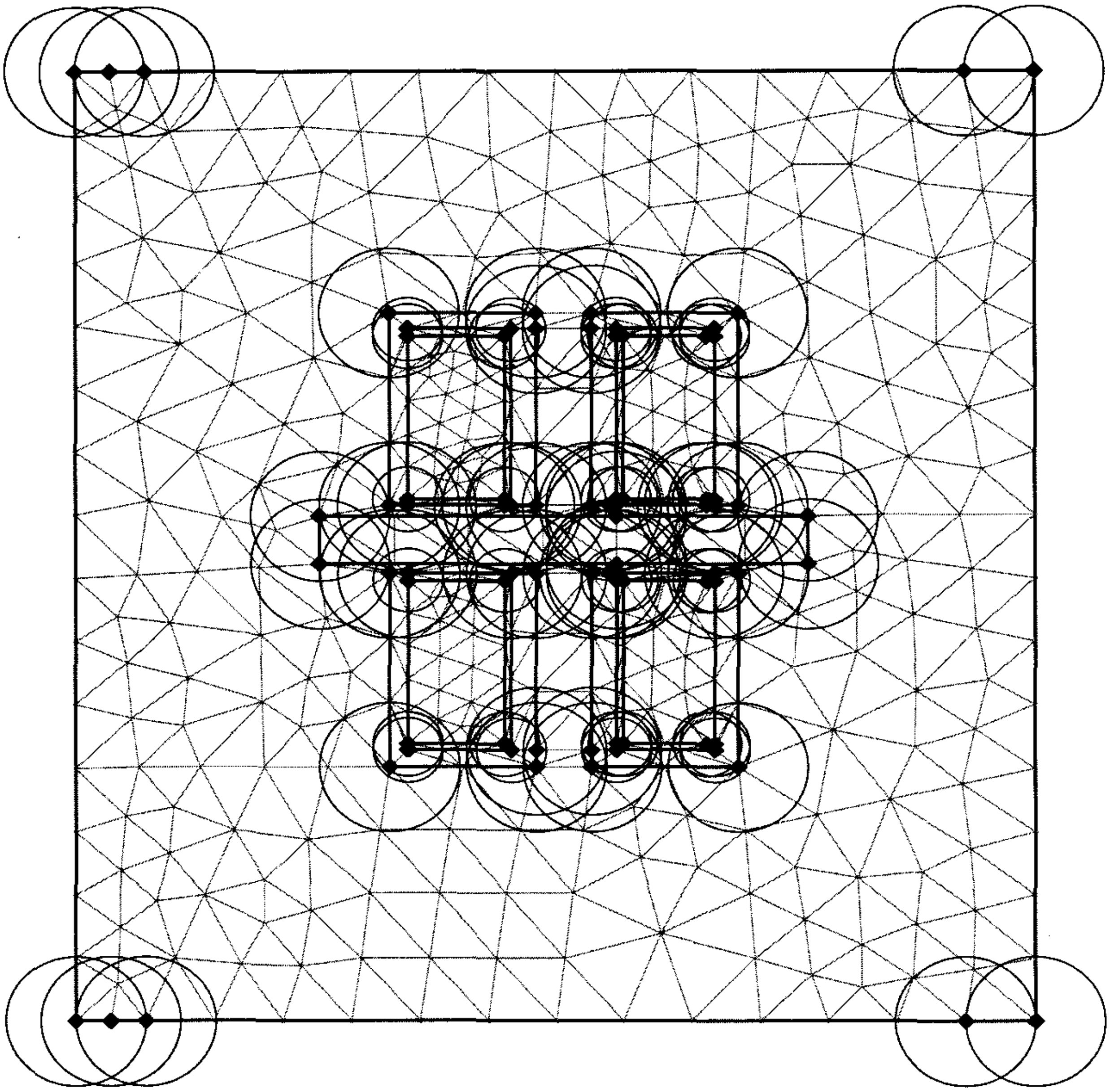

Figure D.1: Mesh of the complete system

Figure D.1 shows the electromagnets viewed in geometry mode. The total number of nodes was limited to 192. The mesh is the small green lines filling up the rectangles. The circles show the spacing needed to create the mesh. The air parameter was designed with 2 cm spacing and the coil and steel parameters was designed with 1 cm spacing.

APPENDIX E

CALCULATION OF THE SPRING-MASS-DAMPER CONSTANTS

This appendix focuses on the calculation of the spring-mass-damper constants. Calculation of the constants of the system with one electromagnet will be done first, followed by the calculations of the system with both electromagnets.

E.1 SYSTEM WITH ONE ELECTROMAGNET

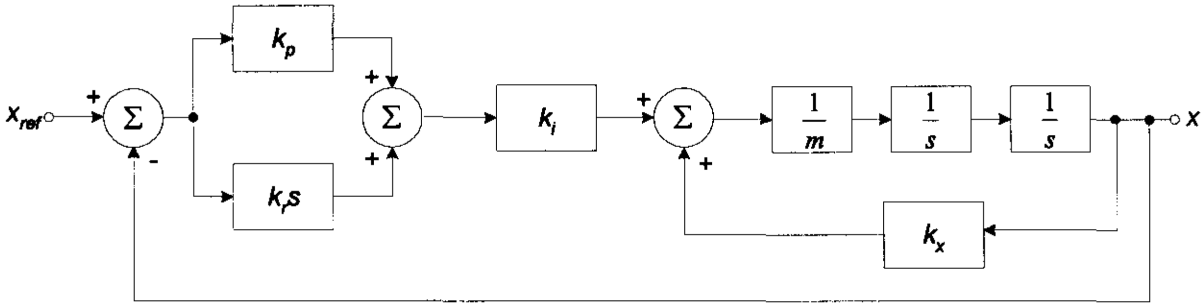

Figure E.1: Block diagram of the system with one electromagnet

Figure E.1 provides the block diagram and figure E.2 the signal flow diagram of the system with one electromagnet. These figures will be used for calculation of the constants.

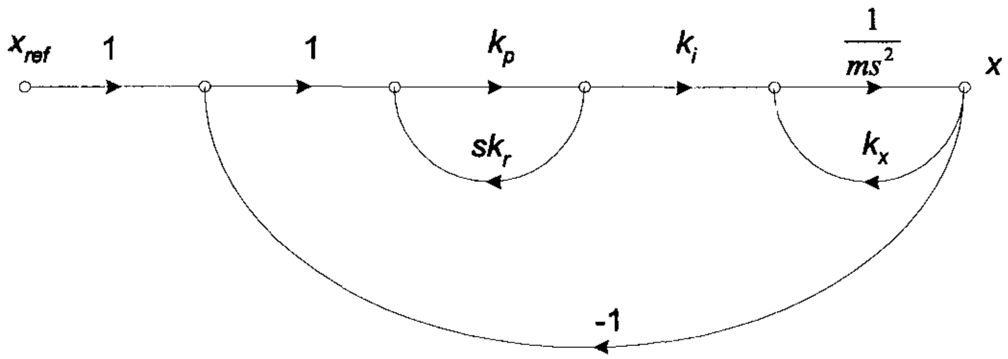

Figure E.2: Signal flow diagram of the system with one electromagnet

The paths and cofactors obtained from figure E.2 are calculated by (1) and (2).

$$P_1 = \frac{k_p k_i}{ms^2} \qquad \Delta_1 = 1 \tag{1}$$

$$P_2 = \frac{k_r k_i}{ms} \qquad \Delta_2 = 1 \tag{2}$$

where P_1 and P_2 are the paths and Δ_1 and Δ_2 are the cofactors of the paths.

The loops are calculated by (3), (4) and (5).

$$L_1 = \frac{k_x}{ms^2} \tag{3}$$

$$L_2 = -\frac{k_p k_i}{ms^2} \tag{4}$$

$$L_3 = -\frac{k_r k_i}{ms} \tag{5}$$

The determinant of the graph is given by (6).

$$\Delta = 1 - (L_1 + L_2 + L_3) \tag{6}$$

The gain formula is given by (7).

$$\begin{aligned} T(s) &= \frac{P_1\Delta_1 + P_2\Delta_2}{\Delta} \\ &= \frac{\frac{k_p k_i}{ms^2} + \frac{k_r k_i}{ms}}{1 - \frac{k_x}{ms^2} + \frac{k_p k_i}{ms^2} + \frac{k_r k_i}{ms}} \\ &= \frac{\frac{k_i}{m}\left(k_r s + k_p\right)}{s^2 + \left(\frac{k_r k_i}{m}\right)s + \left(\frac{k_p k_i}{m} - \frac{k_x}{m}\right)} \end{aligned} \tag{7}$$

Standard form of root equation is given by $s^2 + 2\zeta\omega_n s + \omega_n^2$, where ζ is the damping ratio and ω_n is the natural frequency of the system. Standard form of the spring-mass-damper equation is given by $s^2 + \left(\frac{b_{eq}}{m}\right)s + \left(\frac{k_{eq}}{m}\right)$, where b_{eq} is the damping constant, m is the mass and k_{eq} is the stiffness of the system.

Therefore: $\frac{b_{eq}}{m} = \frac{k_r k_i}{m}$ $\quad \therefore b_{eq} = k_r k_i$

and $\frac{k_{eq}}{m} = \frac{k_p k_i - k_x}{m}$ $\quad \therefore k_{eq} = k_p k_i - k_x$

Further $\omega_n = \sqrt{\frac{k_p k_i - k_x}{m}}$ and $2\zeta\omega_n = \frac{k_r k_i}{m}$ $\quad \therefore \zeta = \frac{k_r k_i}{2\omega_n} = \frac{k_r k_i \sqrt{m}}{2\sqrt{k_p k_i - k_x}}$

E.2 SYSTEM WITH BOTH ELECTROMAGNETS

Figure E.3 provides the block diagram and figure E.4 the signal flow diagram of the system with both electromagnets. These figures will provide the basis for the calculation of the spring-mass-damper constants. The parameter i_0 in figure E.4 represent the bias current.

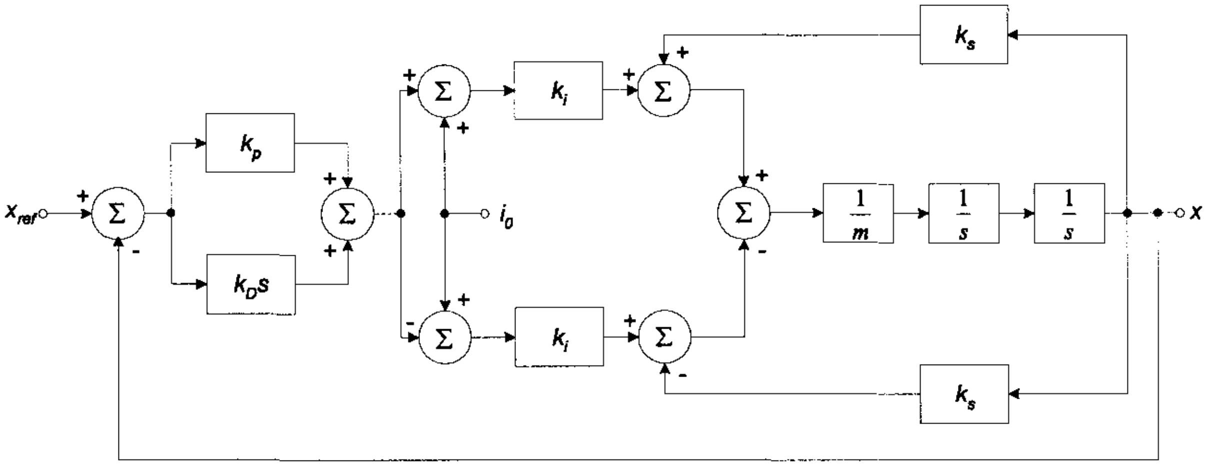

Figure E.3: Block diagram of the system with both electromagnets

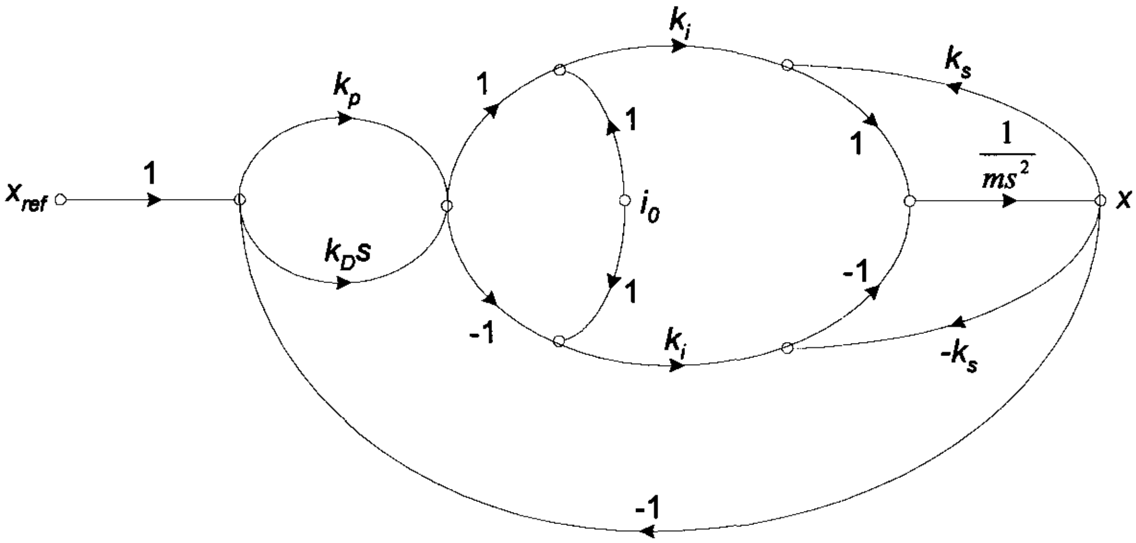

Figure E.4: Signal flow diagram of the system with both electromagnets

The paths and loops obtained from figure E.2 are given by (8) and (9).

$$P_1 = \frac{k_p k_i}{ms^2},\ P_2 = \frac{k_D s \cdot k_i}{ms^2} = \frac{k_D k_i}{ms},\ P_3 = \frac{k_p k_i}{ms^2},\ P_4 = \frac{k_D s \cdot k_i}{ms^2} = \frac{k_D k_i}{ms} \tag{8}$$

$$L_1 = \frac{k_s}{ms^2},\ L_2 = \frac{k_s}{ms^2},\ L_3 = -\frac{k_p k_i}{ms^2},\ L_4 = -\frac{k_D k_i}{ms},\ L_5 = L_3,\ L_6 = L_4 \tag{9}$$

The calculation of the gain formula, determinant of the graph and cofactors of the paths is given by (10).

$$T(s) = \frac{P_1\Delta_1 + P_2\Delta_2 + P_3\Delta_3 + P_4\Delta_4}{\Delta}$$
$$\Delta = 1 - (L_1 + L_2 + L_3 + L_4 + L_5 + L_6), \qquad \Delta_1 = \Delta_2 = \Delta_3 = \Delta_4 = 1 \tag{10}$$

The gain formula is given by (11).

$$\begin{aligned} T(s) &= \frac{\dfrac{2k_p k_i}{ms^2} + \dfrac{2k_D k_i}{ms}}{1 - \left(\dfrac{2k_s}{ms^2} - \dfrac{2k_p k_i}{ms^2} - \dfrac{2k_D k_i}{ms}\right)} \\ &= \frac{2k_p k_i + 2k_D k_i s}{ms^2 + 2k_D k_i s + (2k_p k_i - 2k_s)} \end{aligned} \tag{11}$$

Therefore from the root equation and the spring-mass-damper equation constants can be obtained.

$$\begin{aligned} q(s) &= s^2 + \frac{2k_D k_i}{m} s + \frac{2k_p k_i - 2k_s}{m} \\ &= s^2 + \frac{b_{eq}}{m} s + \frac{k_{eq}}{m} \end{aligned} \tag{12}$$

The damping constant b_{eq} and stiffness k_{eq} can be found in (13).

$$\begin{aligned} b_{eq} &= 2k_D k_i \\ k_{eq} &= 2k_p k_i - 2k_s \end{aligned} \tag{13}$$

APPENDIX F

PSPICE® ANALYSIS OF THE INDUCTIVE SENSOR

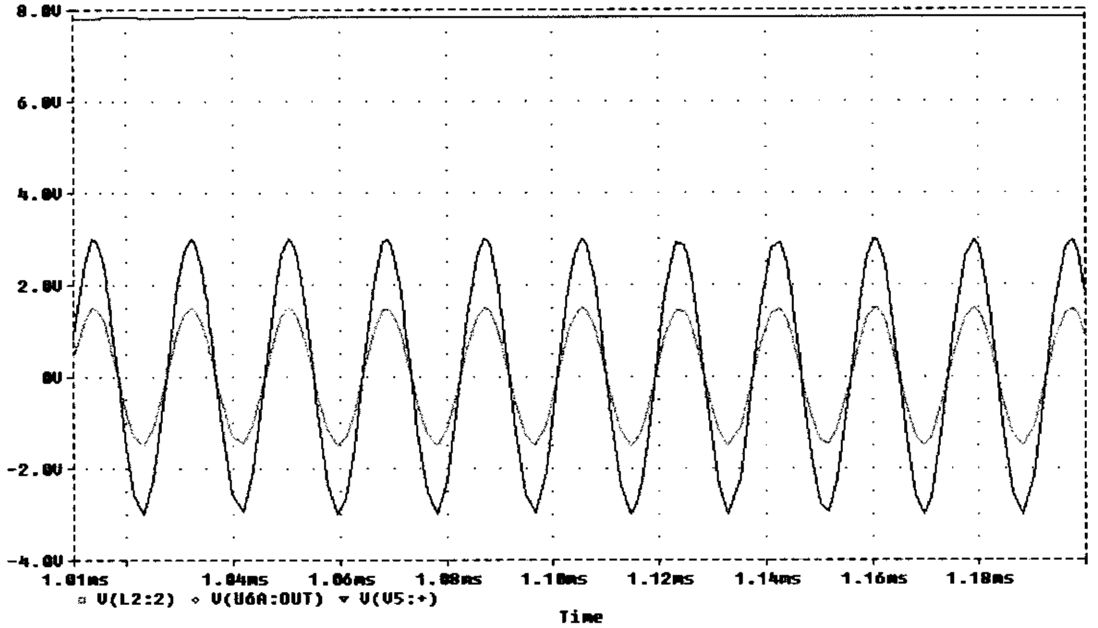

Figure F.1: Output of the sensors with $L_1 = L_2$

The d.c. line in the figure F.1 is the output of the sensor. The sine wave with amplitude of 1.5 V is the input signal of the sensor and the sine wave with amplitude of 3 is the output of coil L_1 in figure B.1. Figure F.2 provides the output obtained from the active rectifier. A sine wave with amplitude 1 V was given as input and the dc output was obtained.

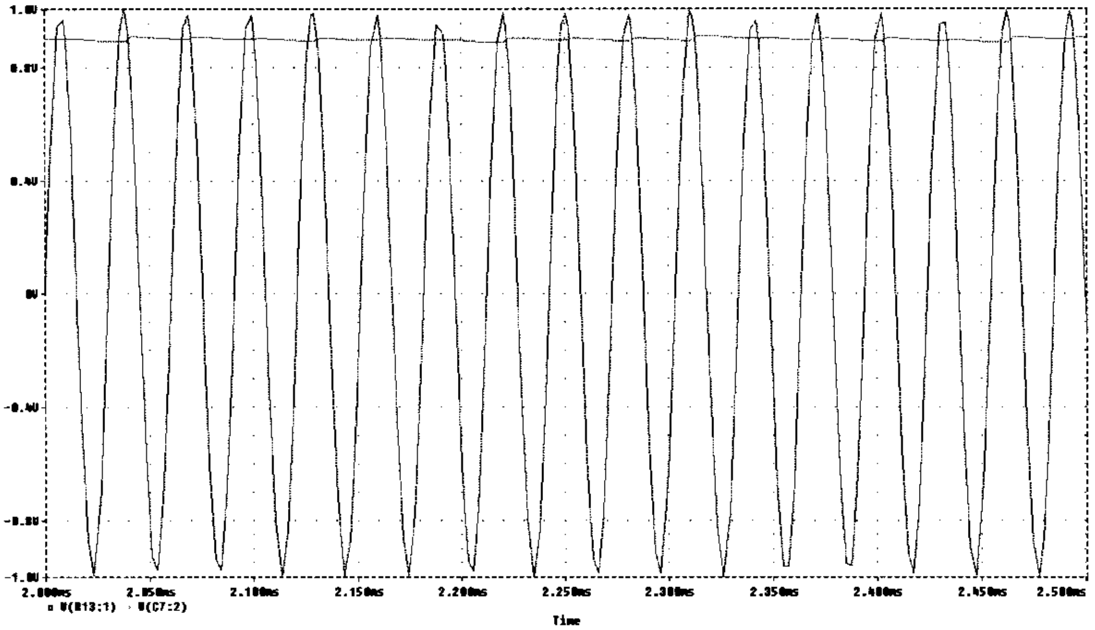

Figure F.2: Output obtained from the active rectifier

APPENDIX G

OSCILLOSCOPE PRINTOUTS OF THE SENSOR AND CONTROLLERS

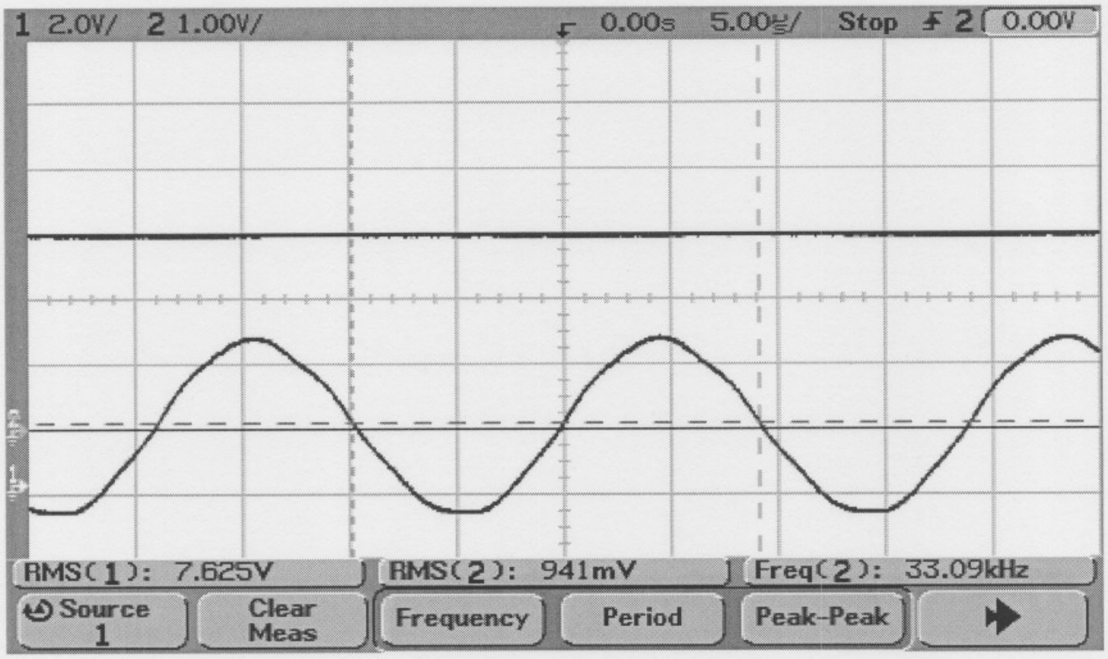

Figure G.1: Oscilloscope output of the sensors with $L_1 = L_2$

The signal with amplitude of 1.5 V and frequency of 33 kHz is the input signal to the sensor and can be seen in figure G.1 and figure G.2. The d.c. signal is the sensor output in figure G.1 and the signal with amplitude of ≈3 V is the output of coil L_1 as shown in figure B.1.

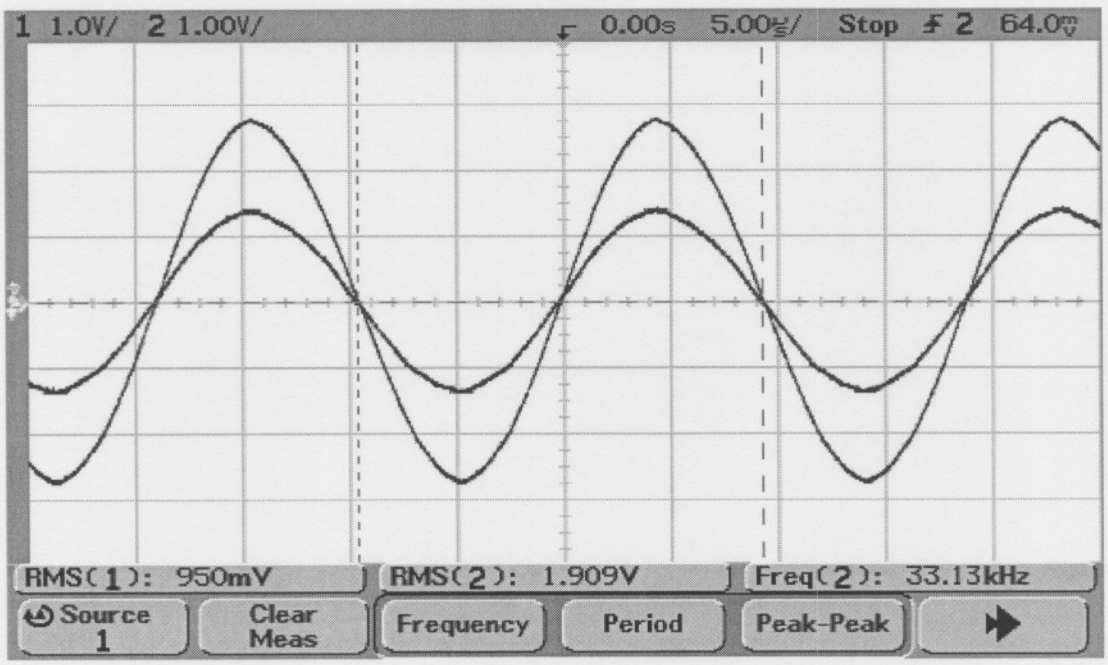

Figure G.2: Sensor input and inductor output with $L_1 = L_2$

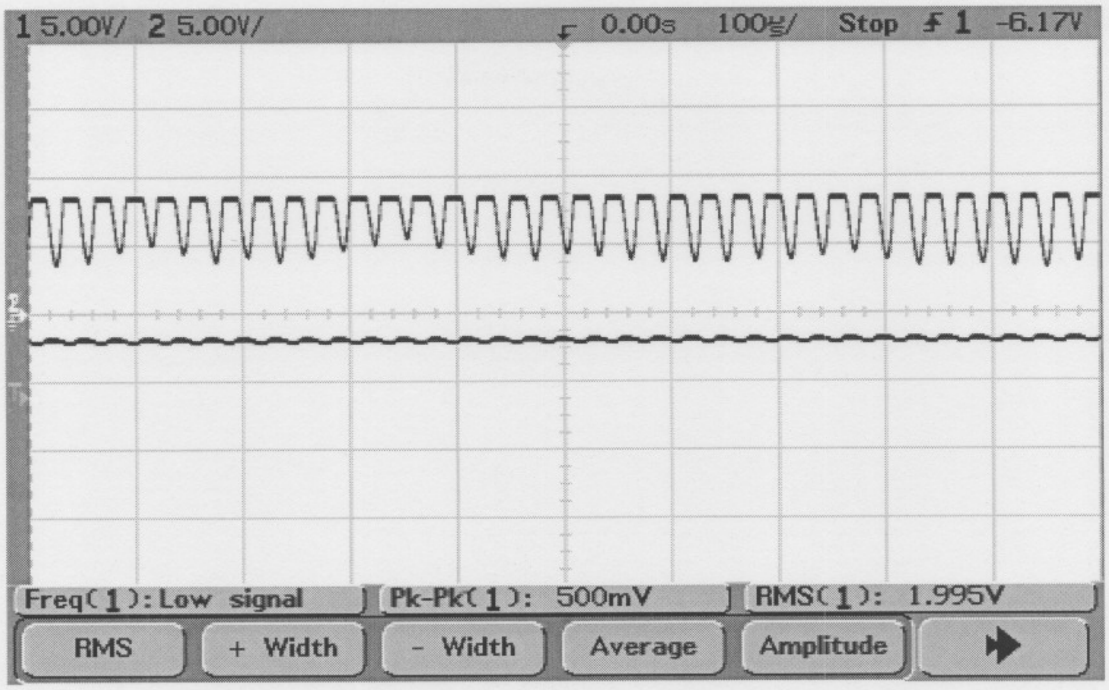

Figure G.3: Lead controller output with a positive air gap

The d.c. line in figure G.3 and figure G.4 is the output from the sensor. The other signal is the output of the lead controller. In figure G.3 the bottom electromagnet is attracting and the top one is releasing. In figure G.4 the top electromagnet is attracting and the bottom one is releasing.

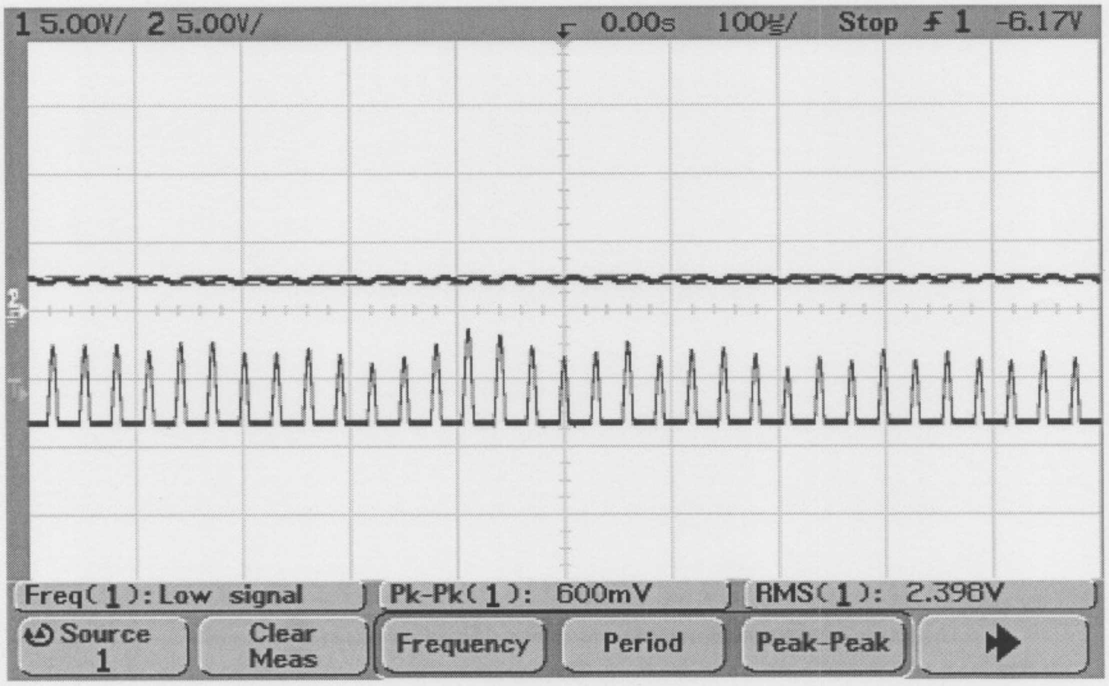

Figure G.4: Lead controller output with a negative air gap

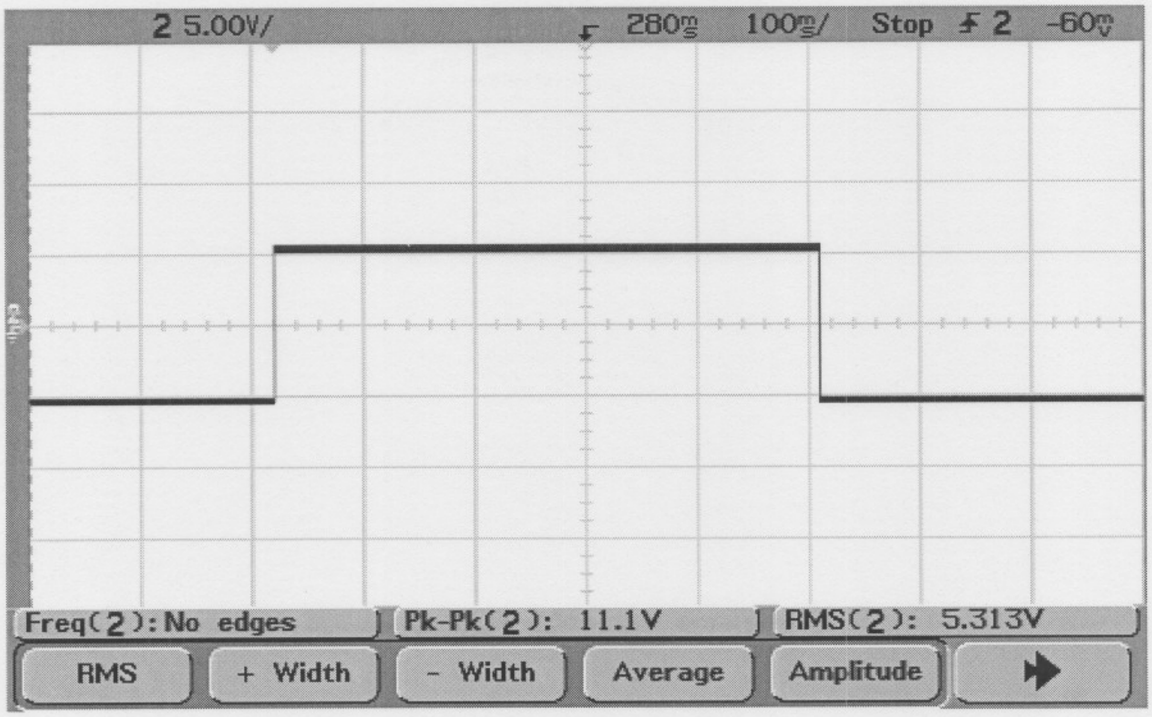

Figure G.5: Input step signal for the system with an analog PID controller

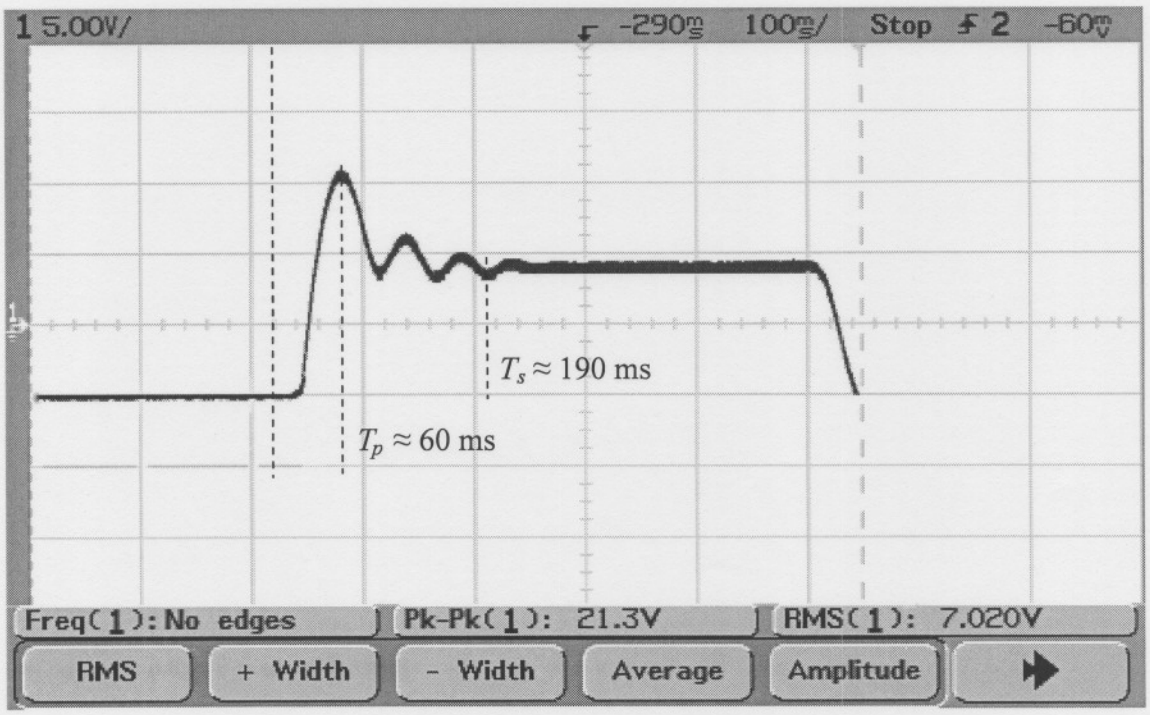

Figure G.6: System output signal for a step input (PID controller)

The analog PID controller has a time-to-peak $T_p \approx 60$ ms and settling time $T_s \approx 190$ ms.

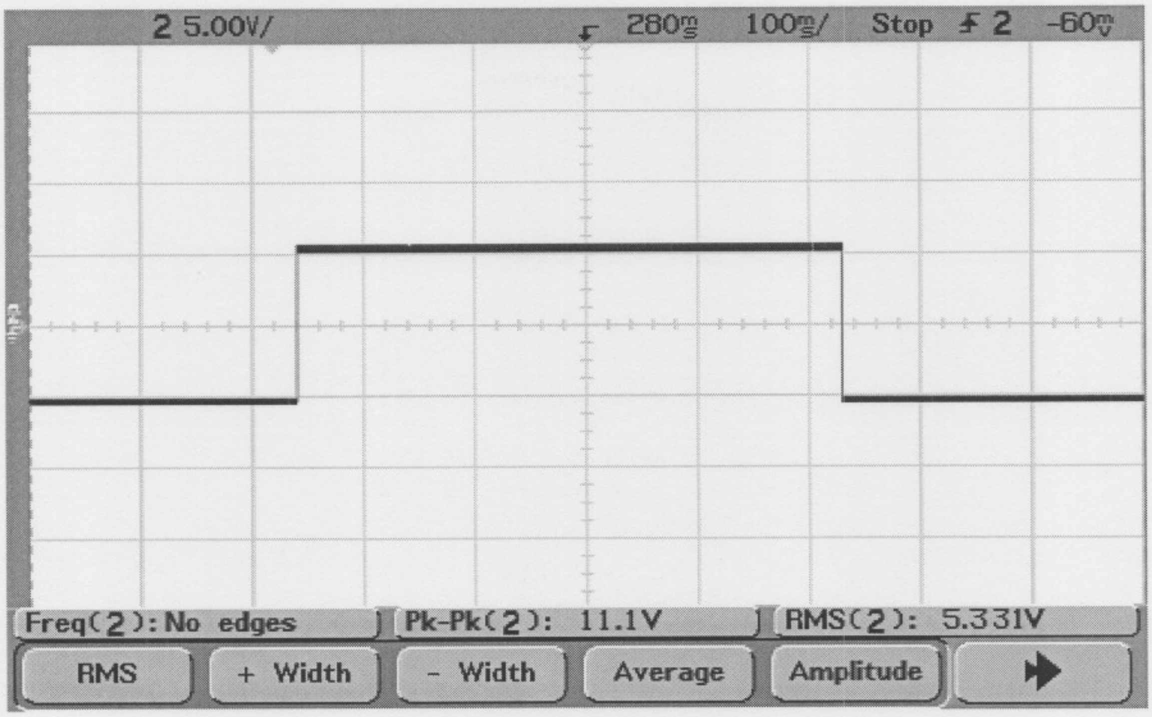

Figure G.7: Input step signal for the system with an analog lead controller

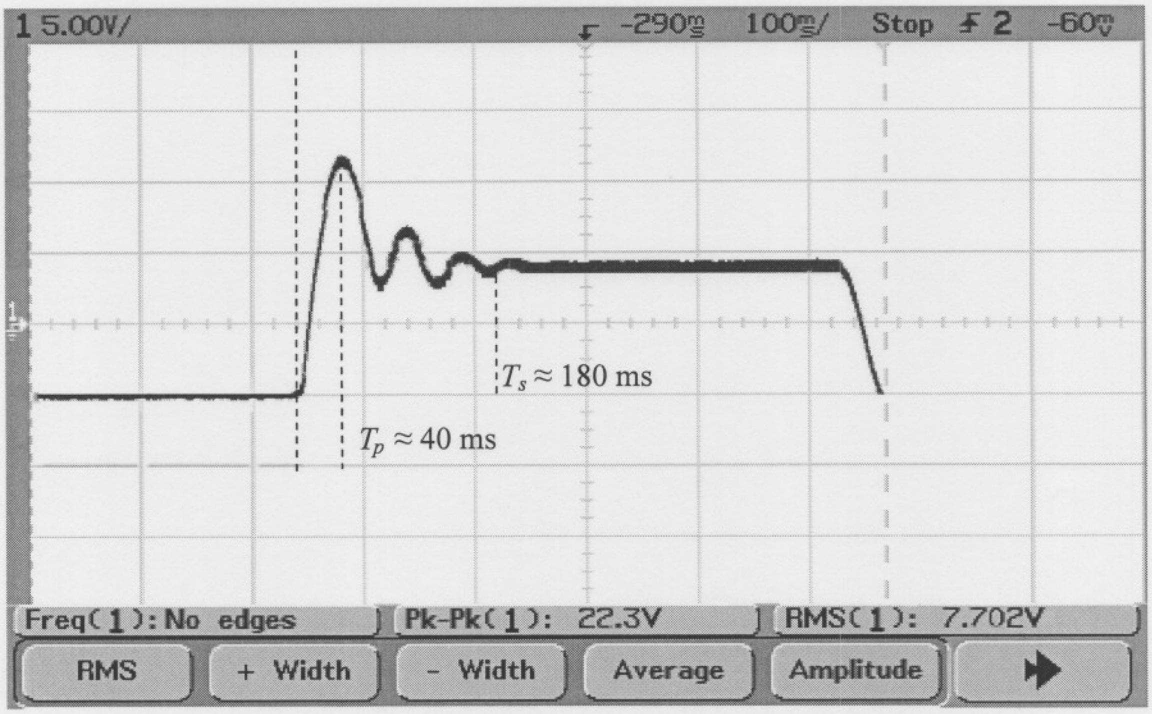

Figure G.8: System output signal for a step input (lead controller)

The analog lead controller has a time-to-peak $T_p \approx 40$ ms and settling time $T_s \approx 180$ ms.

APPENDIX H

MATLAB® SOURCE CODE FOR LEAD CONTROLLER DESIGN

```
%Selecting K gain
K = 10;

%Transfer function of the oncompensated system
numg = [-500]; deng = [1 0 -0.05];

%Calculation of the phase margin
[num,den] = series(K,1,numg,deng);
w = logspace(-1,4,200);
[mag,phase,w] = bode(num,den,w);
[Gm,Pm,Wcg,Wcp] = margin(mag,phase,w);

%Additional phase lead
Phi = -(110+Pm)*pi/180;

%Compute the value of alpha
alpha = (1+sin(Phi))/(1-sin(Phi))

%Plot -10log(alpha) line to aid in locating Wm
M = -10*log10(alpha)*ones(length(w),1);

%Final plot and labels
[mag,phase,w] = bode(num,den,w);
semilogx(w,20*log10(mag),w,M),grid
xlabel('frequency [rad/sec]'), ylabel('mag [dB]')
```

The above source code is for the design of the lead controller (section 5.5). The Bode diagrams can be seen in figure 5.19 and figure 5.22.

APPENDIX I

DATASHEETS, CATALOGS AND MOVIE CLIPS

I.1. dSPACE® ACE 1104 ADVANCED CONTROL KIT *(ACE01-e.pdf)*

I.2. DS1104 R&D CONTROLLER BOARD (*ds1104_flyer2002_en.pdf*)

I.3. MLIB/MTRACE® FUNCTIONS (*dspace-catalog2002_mlib-mtrace.pdf*)

I.4. CONTROLDESK® SOFTWARE CATALOG (*dspace-catalog2002_controldesk.pdf*)

I.5. 4N25 OPTOCOUPLER/PHOTOTRANSISTOR *(4N25.pdf)*

I.6. ICL8038 WAVEFORM GENERATOR/VOLTAGE CONTROLLED OSCILLATOR *(ICL8038.pdf)*

I.7. TL072, LOW NOISE DUAL J-FET OPERATIONAL AMPLIFIER *(TL072.pdf)*

I.8. TL082, GENERAL PURPOSE DUAL J-FET OPERATIONAL AMPLIFIER *(TL082.pdf)*

I.9. 2N3055, SILICON NPN HIGH-POWER TRANSISTOR *(2N3055.pdf)*

I.10. MOVIE CLIP 1: SUSPENDED DISK WITH NO ROTATION *(Suspending_no rotation.avi)*

I.11. MOVIE CLIP 2: SUSPENDED DISK WITH ROTATION *(Suspending1_rotating.avi)*

I.12. MOVIE CLIP 3: SUSPENDED DISK WITH ROTATION *(Suspending2_rotating.wmv)*

I.13. MOVIE CLIP 4: SUSPENDED DISK WITH SQUARE WAVE INPUT *(Suspending square wave.avi)*

All the above datasheets and catalogs contain technical detail of the project. These PDF, AVI and WMV files are included in the CD, available on request.